A Study of Neutrino Oscillation Models with Super-Kamiokande Atmospheric Neutrino Data

Michael R. Dziomba

A dissertation
submitted in partial fulfillment of the
requirements for the degree of

Doctor of Philosophy

University of Washington

2012

Reading Committee:

R. Jeffrey Wilkes, Chair

Ann E. Nelson

Thompson Burnett

Program Authorized to Offer Degree:
Physics

University of Washington

Abstract

A Study of Neutrino Oscillation Models with Super-Kamiokande Atmospheric Neutrino Data

Michael R. Dziomba

Chair of the Supervisory Committee:
Professor R. Jeffrey Wilkes
Physics

The rapidly evolving field of neutrino oscillations continues to offer exciting experimental results as it enters the era of precision measurements. The mixing angles and mass-squared splittings governing neutrino oscillations have all been measured experimentally and only one parameter, the CP-violating phase δ, remains unmeasured. Both atmospheric and long-baseline accelerator experiments are sensitive to the parameters θ_{23} and Δm^2_{23}. In particular the wide range of neutrino pathlengths and energies accessible to the Super-Kamiokande (SK) detector with atmospheric neutrinos offer a unique opportunity to measure these parameters with high-statistics data. SK is also suitable for constraining exotic oscillation models which include sterile neutrinos and non-standard matter interactions, due to the large variations in density through which atmospheric neutrinos can traverse. In this thesis we use an expanded atmospheric neutrino dataset combined with improved Monte Carlo simulations to update the SK 2-flavor muon neutrino disappearance zenith angle analysis. We measure values of $\Delta m^2_{23} = 2.30^{+0.17}_{-0.22} \times 10^{-3}$ eV^2 and $\sin^2 2\theta_{23} > 0.95$ (90% C.L.), in excellent agreement with recent worldwide results. We also fit the SK data to a recent exotic model which incorporates both sterile-active mixing and a new non-standard interaction in matter. We find that SK rules out most of the model's parameter space and restricts it to the region where standard 2-flavor mixing is recovered.

TABLE OF CONTENTS

LIST OF FIGURES

GLOSSARY

SK: Super-Kamiokande

ID: Inner detector

OD: Outer detector

FV: Fiducial volume

MC: Monte Carlo

CC: Charged current

NC: Neutral current

ACKNOWLEDGMENTS

The work in this thesis would not have been possible without the help of many people. First and foremost I would like to thank Professor Jeff Wilkes for advising me throughout my graduate school career. His mentoring style suited me perfectly and allowed me to enjoy my experience as a graduate student. The introductions to the Super-Kamiokande Collaboration and Japan that he gave me will leave a lasting mark on me.

I am indebted to Roger Wendell for personally guiding me through the analyses in this work. His endless efforts for both Super-Kamiokande as a whole and my personal progress have been invaluable and his friendship has made Japan a memorable experience. I am also very grateful for the wonderful and patient instruction I received from Jen Raaf, who was always willing to take the time to help me.

I would also like to extend thanks to Ed Kearns, Shiozawa-san, Chris Walter and Kate Scholberg for their excellent guidance within the AtmPD group, as well as to all Japanese colleagues whose tireless efforts have allowed Super-Kamiokande to be so successful.

I have thoroughly enjoyed my time as a graduate student at the University of Washington because of the friends I have been lucky to surround myself with. Kevin Connolly has been a great friend throughout and I hope our discussions about physics, language and life continue for a long time. The rest of my graduate school comrades, including Laura Bodine, Eric Wallace, Jason Dexter and many others have made Seattle a wonderful experience.

I have also shared many wonderful experiences with my fellow students in Japan, including but not limited to Kota, Piotr, Maggie, Joshua, T, Tanaka-san and Ikeda-san. I am also very thankful for my many friends in Buffalo, especially Zack Long and Dave Stockburger, who have not forgotten me as my dreams have taken me far away from home.

The love, support and encouragement of my family, especially Mom, Dad, and Grandma Jane, has been invaluable and for that I cannot thank them enough.

DEDICATION

For my family.

Chapter 1

INTRODUCTION

The study of neutrinos began in 1930 when Wolfgang Pauli postulated the existence of a neutral particle with a very small mass in order to explain the continuous electron energy spectrum found in β decays[99]. Since then, the field has been driven by vast theoretical literature and exciting experimental results. The neutrino has been the target of experimental studies for approximately 60 years and as of this writing new results are still being released and future experiments are in their early design phases. The current and future experiments have taken neutrino physics beyond the discovery stage and into the era of precision measurements. The present work builds upon the vast experimental framework set up by previous results and also hints at the shift to precision measurements in the field of atmospheric neutrino oscillations.

1.1 Neutrinos

Neutrinos are electrically-neutral spin-1/2 leptons which only undergo weak interactions. In the standard model (SM) of particle physics, neutrinos are massless and come in three flavors, electron (ν_e), muon (ν_μ) and tau (ν_τ), analogous to the charged leptons. They are also experimentally known to exist only as left-handed neutrinos or right-handed anti-neutrinos[80].

Though existing copiously throughout the universe, they are experimentally very difficult to detect as they can pass through tremendous amounts of matter without interacting. Soon after their initial theoretical proposal by Pauli in 1930, Fermi generated a point-like theory for neutrino interactions[74]. The currently verified unified electroweak theory which describes neutrino interactions would not be fully developed until the 1960s and the weak interaction mediating bosons, the $W^{\pm}$ and Z^0 were eventually discovered in 1983. The large masses of these vector bosons (M_W = 80.6 GeV/c^2, M_Z = 91.2 GeV/c^2) result in a weak

interaction range of only about 10^{-18} m. The neutrino itself was first definitively detected in 1956 by Cowan and Reines using the inverse β decay reaction $\bar{\nu} + p \rightarrow e^+ + n$ taking place in a liquid scintillator surrounded by photomultiplier tubes (sensitive photon detectors which will be described in more detail later)[90]. The source of the electron antineutrinos in this experiment was a nearby nuclear reactor facility.

Neutrinos have since been detected from natural sources such as the Sun[16], Earth's atmosphere[67], the core of the Earth[10], man-made accelerator beamlines[52] and a Supernova event in 1987[41]. In addition to electron flavor neutrinos, muon[29] and tau flavor neutrinos[77] have also been detected, and experiments studying weak boson decays (in particular, the Z^0 boson which mediates NC weak interactions) currently limit the number of light species which participate in weak interactions to these three[9].

1.2 Atmospheric Neutrinos

This work focuses on the behavior of atmospheric neutrinos. Cosmic rays which are predominantly high-energy protons arrive from space and interact with nitrogen and oxygen molecules in the Earth's atmosphere. Mesons (quark-antiquark pairs) such as pions (π) and kaons (K) are produced in large numbers in these reactions. These mesons are not stable and their decays produce neutrinos. A typical decay chain beginning with a pion has the form

$$\pi^+ \rightarrow \mu^+ + \bar{\nu}_\mu \tag{1.1}$$

which produces a muon antineutrino. The muon then decays by the process

$$\mu^+ \rightarrow e^+ + \nu_e + \bar{\nu}_\mu \tag{1.2}$$

producing an additional muon antineutrino and a single electron neutrino. This process was assumed to begin with a π^+ particle, but the charge conjugate of this process which produces two muon neutrinos and one electron antineutrino is also possible. With these decay chains producing the atmospheric neutrino flux (the fraction of neutrinos produced by kaon decays becomes significant at really high energies), we expect the flux ratio $(\nu_\mu + \bar{\nu_\mu}/\nu_e + \bar{\nu_e})$ to be roughly two. In reality this ratio is energy-dependent, but this assumption for the ratio is generally valid for neutrino energies up to around 1 GeV. More energetic muons may reach

the surface of the Earth before decaying and so a ratio smaller than two would be expected for a terrestrial experiment at higher neutrino energies. Though the uncertainties on the absolute neutrino and antineutrino fluxes are relatively large (they can be on the order of 10-25% depending on energy), this flavor ratio is estimated with an uncertainty of only 2% [48]. Significant deviations of this ratio from 2 offered the first evidence that neutrinos exhibited behavior beyond their description in the standard model.

1.3 Neutrino Oscillations

Contrary to their masslessness in the SM, evidence for massive neutrinos has been found via flavor transformations, or "oscillations", in neutrinos produced from the sun[61], hadronic decays in the atmosphere[65], accelerator beamlines[52, 36] and nuclear reactors[59, 27, 43]. Neutrino oscillations are sensitive to the differences in the squared masses of the states, defined by $\Delta m^2_{ij} \equiv m^2_j - m^2_i$. Thus, measurements of this parameter by neutrino oscillation experiments places a lower bound on at least as many neutrino mass states as the number of separate mass-squared splittings.

Independent of the oscillation experiments, upper constraints have been placed on the absolute neutrino masses. Tritium beta-decay end-point measurements have restricted the effective electron-neutrino mass to be $m_{\nu e} < 2.0$ eV [63, 25, 34]. Relatively high limits for the effective muon and tau neutrino masses of $m^{eff}_{\nu_\mu} < 0.19$ MeV and $m^{eff}_{\nu_\tau} < 18.2$ MeV also exist [34]. These limits are taken from pion decay ($\pi^+ \rightarrow \mu^+ + \nu_\mu$) and tauon decay spectrum shape analyses and are limited by the short lifetimes of the decaying particles involved. Cosmology also places very rough bounds on the upper limit of the sum of neutrino masses. Current limits are in the range $\sum_\nu \leq (0.75 - 5.5)$ eV[34][86][2].

Neutrino oscillations occur when the neutrino flavor states as defined by charged-current weak interactions and the mass eigenstates are not identical, and neutrinos also have non-zero masses. These were first proposed theoretically in the 1960s by Maki, Nakagawa and Sakata[93] and Pontecorvo[100]. The basic assumption is that the flavor states (indexed by letter) can be written as a linear superposition of three mass states (traditionally indexed by number):

$$|\nu_\alpha\rangle = \sum_{i=1}^{3} U^*_{\alpha i}|\nu_i\rangle \tag{1.3}$$

The transformation can be fully written out in terms of a unitary matrix transforming between the two sets of basis states. It has the general form

$$\begin{pmatrix} \nu_e \\ \nu_\mu \\ \nu_\tau \end{pmatrix} = \begin{pmatrix} U_{e1} & U_{e2} & U_{e3} \\ U_{\mu 1} & U_{\mu 2} & U_{\mu 3} \\ U_{\tau 1} & U_{\tau 2} & U_{\tau 3} \end{pmatrix} \begin{pmatrix} \nu_1 \\ \nu_2 \\ \nu_3 \end{pmatrix}. \tag{1.4}$$

It then takes the form

$$\begin{pmatrix} \nu_e \\ \nu_\mu \\ \nu_\tau \end{pmatrix} = \begin{pmatrix} 1 & 0 & 0 \\ 0 & \cos\theta_{23} & \sin\theta_{23} \\ 0 & -\sin\theta_{23} & \cos\theta_{23} \end{pmatrix} \begin{pmatrix} \cos\theta_{13} & 0 & \sin\theta_{13}e^{-i\delta} \\ 0 & 1 & 0 \\ -\sin\theta_{13}e^{i\delta} & 0 & \cos\theta_{13} \end{pmatrix} \begin{pmatrix} \cos\theta_{12} & \sin\theta_{12} & 0 \\ -\sin\theta_{12} & \cos\theta_{12} & 0 \\ 0 & 0 & 1 \end{pmatrix} \begin{pmatrix} \nu_1 \\ \nu_2 \\ \nu_3 \end{pmatrix} \tag{1.5}$$

where the so-called mixing angles θ_{12}, θ_{13}, θ_{23} and the CP-violating phase δ are the four parameters of the matrix which can be experimentally constrained. The separation of the sub-matrices roughly represent different areas of experimental research in neutrino oscillations. In particular, atmospheric and long baseline accelerator experiments such as SK have measured θ_{23}, reactor and accelerator experiments have recently measured θ_{13}, and solar experiments (including SK) have measured θ_{12}. There has been no measurement of δ as of yet. The current best-fit values for the mixing angles from a 2011 global analysis are shown in Table 1.1.

The experiments involve transformations of one neutrino flavor ν_α into another, ν_β, after propagation of a baseline L. It is useful to express this mathematically via the oscillation probability $\mathrm{P}(\nu_\alpha \rightarrow \nu_\beta)$. In the case where $\alpha = \beta$ the oscillation probability becomes a survival probability. In the following calculations the letters a,b and c represent flavor eigenstates, and the letters i,j, and k represent mass eigenstates. We can calculate the

Parameter	Best-Fit ($\pm 1\sigma$)
Δm^2_{23}	$2.35^{+12}_{-.09} \times 10^{-3}\text{eV}^2$
$\sin^2\theta_{23}$	$0.42^{+.08}_{-.03}$
δm^2_{12}	$7.58^{+0.22}_{-0.26} \times 10^{-5}\text{eV}^2$
$\sin^2\theta_{12}$	$0.306^{+.018}_{-.015}$
$\sin^2\theta_{13}$	$0.025^{+.007}_{-.007}$

Table 1.1: Global analysis constraints on the three mixing angles and two mass-squared splittings governing neutrino oscillations[76].

probability by assuming the initial state at t = 0 to be $|\nu_a = U^*_{aj}|\nu_j\rangle$. Applying time evolution, the state at time t is then

$$|\nu(t)\rangle = U^*_{aj} e^{-iE_j t}|\nu_j\rangle \tag{1.6}$$

We can then calculate the probability amplitude of detecting the neutrino in flavor state $|\nu_b\rangle$ at time t:

$$A(\nu_a \to \nu_b; t) = \langle\nu_b|\nu(t)\rangle = U^*_{aj} e^{-iE_j t}\langle\nu_b|\nu_j\rangle = U_{bi}U^*_{aj} e^{-iE_j t}\langle\nu_i|\nu_j\rangle = U_{bj} e^{-iE_j t}U^*_{aj}. \tag{1.7}$$

Here summation over repeated indices is implied. To convert this amplitude into a probability, we take the product of this with its complex conjugate:

$$P(\nu_a \to \nu_b; t) = |A(\nu_a \to \nu_b; t)|^2 = |U_{bj} e^{-iE_j t}U^*_{aj}|^2. \tag{1.8}$$

These oscillation probabilities are in general complicated to calculate due to the entries in the matrix U, especially when mixing of all three flavors is considered. A simplified case relevant for the analysis in this thesis will be shown in detail in the following subsection.

1.3.1 Two Flavor Oscillations

A good demonstration of a tractable closed-form oscillation probability is the two flavor oscillation case. We will assume oscillations only of the form $\nu_\mu \leftrightarrow \nu_\tau$, which will be used in

both analyses in this thesis. The 2x2 mixing matrix then takes the form of the lower right 2x2 section of the first sub-matrix in Eq. 1.5, as follows:

$$\begin{pmatrix} \nu_\mu \\ \nu_\tau \end{pmatrix} = \begin{pmatrix} \cos\theta_{23} & \sin\theta_{23} \\ -\sin\theta_{23} & \cos\theta_{23} \end{pmatrix} \begin{pmatrix} \nu_2 \\ \nu_3 \end{pmatrix} \tag{1.9}$$

We insert into Eq. 1.8 the matrix elements from this 2x2 matrix and the energies E_i, which can be given by

$$E_i = \sqrt{p^2 + m_i^2} \approx p + \frac{m_i^2}{2p} \approx p + \frac{m_i^2}{2E}. \tag{1.10}$$

The approximations made here are valid for relativistic neutrinos for which $p \gg m_i$, which is true for atmospheric neutrino energies because of the upper limits placed on the absolute masses. Inserting this into 1.8, we get

$$P(\nu_\mu \to \nu_\tau; t) = \sin^2 2\theta \, \sin^2 \left(\frac{\Delta m^2}{4E} t \right) \tag{1.11}$$

where Δ m^2 is equal to m$_3^2$ - m$_2^2$. For relativistic neutrinos we can replace t with L, and if we rewrite the probability in units useful for atmospheric oscillations with L in km and E in GeV, we arrive at

$$P(\nu_\mu \to \nu_\tau; L) = \sin^2 2\theta \, \sin^2 \left(1.27 \Delta m^2 \frac{L}{E} \right). \tag{1.12}$$

The first sine term in this probability is often referred to as the amplitude of the oscillations and is solely dependent on the mixing angle θ_{23}. The second sine term contains an L/E dependence which in combination with the mass-squared splitting Δm$_{23}^2$ leads to a signature zenith-angle dependent deficit of muon neutrinos in atmospheric neutrino data characteristic of oscillations. The wide range of pathlengths and energies spanned by atmospheric neutrinos provide are suitable for probing large regions of oscillation parameter space.

The two flavor oscillation case is only a simplification of full three-flavor mixing, but is a valid approximation when two conditions are met. The first is that oscillations driven by the other mass-splitting do not contribute significantly, which occur when

$$\frac{\Delta m_{12}^2 L}{E} \ll 1. \tag{1.13}$$

This condition allows the simplification $\Delta m^2_{12} \to 0$ to be made. The second simplification is the matrix element $|U_{e3}| = 0$. This element was recently confirmed to be non-zero, but the condition $|U_{e3}| \ll 1$ is still a respectable approximation given the global best-fit value shown in 1.1. It is these two assumptions which allow the full three-flavor oscillation case to be reduced to the simple two-flavor form of Eq. 1.12.

1.4 Sterile Neutrinos

In addition to the three mass eigenstates driving the standard oscillations, there is also the possibility of additional neutrino mass eigenstates. With the addition of new mass eigenstates, a new linear combination of the states can be constructed as in

$$|\nu_S\rangle = \sum_{i=1}^{N} U^*_{\alpha i} |\nu_i\rangle, \tag{1.14}$$

where N is now equal to the total number of mass eigenstates. Neutrino flavor states described by this linear combination are called sterile neutrinos because they do not participate in Weak interactions. With sterile neutrinos, the unitary transformation matrix expands to NxN, where N is the total number of active plus sterile species. In general the oscillation probabilities will change, usually becoming more complicated, and effects such as extra active disappearance and short baseline appearance can be generated. There has been no experimental confirmation of sterile neutrinos yet but their existence would explain some controversial experimental results.

In 1995 the LSND experiment searched for oscillations of the form $\bar{\nu}_\mu \to \bar{\nu}_e$ with neutrinos from μ^+ decay at rest over very short baselines approximately 30 m with neutrino energies of a few tens of MeV[69]. The experiment saw an excess of $\bar{\nu}_e$ above the expected background with 3.8σ significance. If interpreted as oscillations, the necessary oscillation frequency to drive oscillations with this ratio of L/E would be on the order of 1 eV^2. This is not compatible with the two measured Δm^2 values shown in Tab.1.1. The addition of a fourth mass eigenstate and by extension a sterile neutrino could explain the short-baseline oscillations. However, experiments which sought to confirm the LSND result, such as KARMEN[13, 68] and MiniBooNE[70], did not see evidence for the same type of oscillations and therefore ruled out most of LSND's allowed regions, as shown in Fig. 1.1.

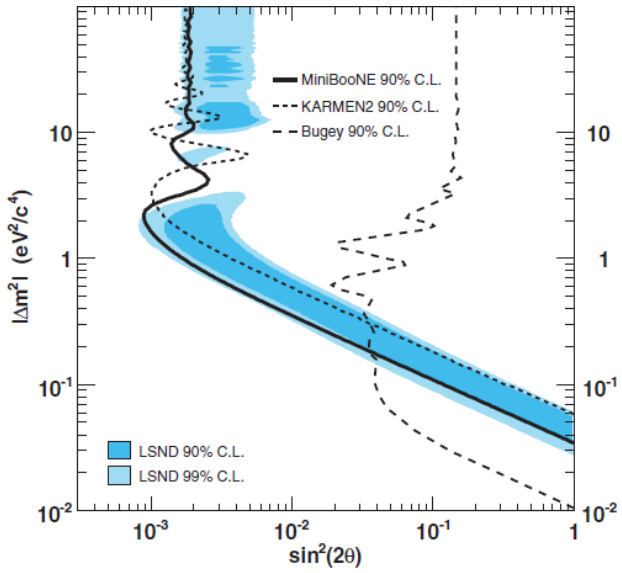

Figure 1.1: The LSND allowed region[69] overlayed with the exclusion regions from KARMEN[68] and MiniBooNE[70] for short baseline oscillations with large Δm^2. Image taken from [70].

However, a recent combined analysis done by the MiniBooNE collaboration claims to have seen an excess consistent with LSND[71]. For atmospheric oscillations, Super-Kamiokande conducted an analysis of their atmospheric neutrino dataset and concluded that for ν_μ disappearance the ν_τ mode was favored over any sterile neutrino mode[60].

Theorists have constructed many exotic models based on sterile neutrinos to explain this oscillation anomaly while maintaining compatibility with other experimental constraints (see [96, 79] for two such models). These models in general employ 1 or 2 sterile neutrinos in 3+1,3+1+1 or 3+2 frameworks, among others. In addition to terrestrial oscillation experiments, cosmologists have also recently used radiation studies related to the cosmic microwave background to suggest the existence of one or two sterile neutrinos[81]. Studies of sterile neutrinos remain an open and interesting topic for experimental searches.

1.5 Oscillations in Matter

Neutrino oscillations in matter are in general not equivalent to those in vacuum. In particular the presence of electrons in ordinary matter further complicates mixing. In addition to scattering and absorption interactions, neutrinos in matter experience effective potential from coherent forward scattering in CC and NC Weak interactions. All flavors experience an identical potential from NC scattering interactions given by

$$V_{NC} = \pm\frac{G_F}{\sqrt{2}}N_n, \tag{1.15}$$

where the sign is positive for neutrinos and negative for antineutrinos. Here N_n represents the number density of neutrons and G_F is the Fermi constant. Ordinary matter is assumed to be electrically neutral so the number of electrons and protons cancel and do not contribute to this potential. Additionally, electron neutrinos can undergo charged-current scattering by exchange of a W boson due to the presence of electrons. This term can be written as

$$V_{\mathrm{CC}} = \pm\sqrt{2}G_F N_e, \tag{1.16}$$

where N_e is now the electron number density and the same sign definitions as above hold. The fact that these potentials are different for electron neutrinos than they are for muon and tau neutrinos can create interesting effects in oscillations. As an example, in the two flavor case where ν_e only mixes with ν_μ, closed-form oscillation probabilities can be calculated. The oscillation probability has the same form as in the vacuum two flavor case:

$$P(\nu_e \to \nu_\mu; L) = \sin^2 2\theta \sin^2\left(\pi\frac{L}{l_m}\right). \tag{1.17}$$

In matter the "oscillation length" l_m is equal to

$$l_m = \frac{2\pi}{\sqrt{\left(\frac{\Delta \mathrm{m}^2}{2E}\cos 2\theta_0 - \sqrt{2}G_F N_e\right)^2 + \left(\frac{\Delta \mathrm{m}^2}{2E}\right)^2 \sin^2 2\theta_0}}. \tag{1.18}$$

Likewise, the expression for the mixing angle in matter also has a similar resonance form:

$$\sin^2 2\theta = \frac{\left(\frac{\Delta \mathrm{m}^2}{2E}\right)^2 \sin^2 2\theta_0}{\left(\frac{\Delta \mathrm{m}^2}{2E}\cos 2\theta_0 - \sqrt{2}G_F N_e\right)^2 + \left(\frac{\Delta \mathrm{m}^2}{2E}\right)^2 \sin^2 2\theta_0}. \tag{1.19}$$

The maximum value of the mixing angle in matter occurs when the condition

$$\sqrt{2}G_F N_e = \frac{\Delta \mathrm{m}^2}{2E}\cos 2\theta_0 \tag{1.20}$$

is true. Thus, large or even maximal mixing can occur in matter even when the vacuum mixing angle is small. This particular condition is called the MSW resonance condition and is used to explain the oscillation of ν_e states produced in the sun. The oscillations assumed here are for $\nu_e \leftrightarrow \nu_\mu$. In the two-flavor approximation, there is no effect from matter in $\nu_\mu \leftrightarrow \nu_\tau$ oscillations because both neutrinos experience only V_{NC} (i.e. there are no CC interactions because μ and τ are not present in ordinary matter). However, if full three-flavor mixing is considered, matter effects apply because the two flavors can mix with the electron neutrino. Additionally, mixing ν_μ and ν_τ with a sterile neutrino will also introduce matter effects, because the sterile neutrino does not even undergo NC interactions (i.e. $V_{NC} = 0$) and so a relative potential difference exists between the active and sterile species, just as in the case when mixing with ν_e was assumed.

1.6 Summary Of This Work

This dissertation uses the entire Super-Kamiokande atmospheric neutrino dataset to place constraints on two neutrino oscillation models. The first model is the standard two-flavor ν_μ disappearance analysis. This model has becoming very well constrained by both atmospheric and long-baseline accelerator experiments. This analysis differs from previous Super-Kamiokande 2-flavor zenith-angle analyses by using new SK data (1,097 days live-time), an updated detector simulation, updated neutrino interaction simulations and a new analysis binning technique (increasing the overall number of bins). These updates are shared with the 2-flavor L/E analysis and full 3-flavor analysis which are also being studied in other SK dissertations this year[92, 94]. The second model which is studied in this work is an exotic model which includes both sterile neutrino and matter oscillation effects. It was first published in 2011 and has not been constrained beyond the authors' initial constraints. The model is analyzed with the same dataset and simulations as the 2-flavor model.

Chapter 2

THE SUPER-KAMIOKANDE DETECTOR

2.1 Introduction

Super-Kamiokande (SK) is a water Cerenkov detector at the Kamioka Observatory of the Institute for Cosmic Ray Research, University of Tokyo. It is located in the town of Kamioka in Gifu prefecture, Japan, west-northwest of Tokyo (see Fig.2.1). The detector sits inside the Mozumi Mine, which is operated by the Kamioka Mining and Smelting Company. It is accessible via a 1.8 km-long mine tunnel which is nearly horizontal.

The geographic coordinates of the detector are $36°25'32.6''$N, $137°18'37.1''$E[12]. The detector cavity lies within Mt. Ikenoyama as shown in Fig. 2.2, covered by 1,000 meters of rock overburden, or 2,7000 meters-water-equivalent(m.w.e). This overburden reduces the rate of downward-going cosmic ray muons reaching the detector to $\sim$ 3 Hz.

It currently operates both as a standalone detector and also as the far detector for the T2K Experiment[39]. Construction of the detector began in 1991 and data-taking began on April 1, 1996. The detector has taken data in four distinct phases, labeled SK-I(1996-2001), SK-II(2002-2005), SK-III(2006-2008), and SK-IV(2008-present). In addition to neutrino oscillation physics, the detector also conducts research on neutrino astrophysics[44], nucleon decay searches[32], dark matter searches[62], and various other particle physics topics.

2.2 Cerenkov Radiation

SK relies on the phenomenon of Cerenkov radiation to detect neutrino interactions. Coherent electromagnetic radiation is generated when a charged particle moves through a medium faster than the local speed of light, analogous to the 'sonic boom' shock wave generated by an object moving faster than the speed of sound in air. The radiation is conical and allows us to determine the incoming direction of neutrinos that have interacted in the detector.

The local speed of light in a given medium is given by

Figure 2.1: Location of the Super-Kamiokande experiment in Japan. Taken from Ref. [12]

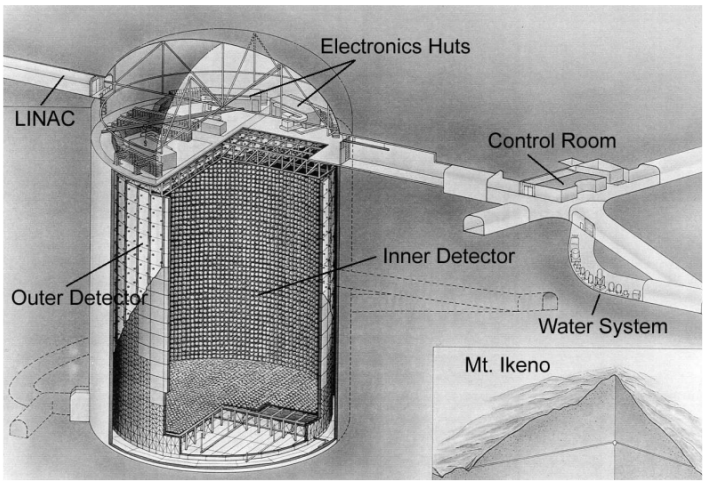

Figure 2.2: An overview of the SK detector and its location within Mt. Ikenoyama. Taken from Ref. [12]

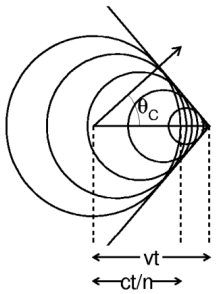

Figure 2.3: A schematic of the Cerenkov radiation emission angle relative to the charged particle's track. Taken from Ref. [111]

$$v = \frac{c}{n} \tag{2.1}$$

where n is the index of refraction of the medium. Charged particles traveling at speeds equal to greater than this will emit Cerenkov radiation. This speed corresponds to Cerenkov emission energy thresholds for electrons of about 0.77 MeV and for muons of about 160 MeV.

The angle of the Cerenkov radiation cone relative to the charged particle's track also depends on n and is equal to [89]

$$cos(\theta_c) = \frac{1}{n\beta} \tag{2.2}$$

.

A schematic showing the Cerenkov radiation emission angle for a particle moving with speed v/c is shown in Fig. 2.3.

In the ultra-relativistic limit where $\beta \to 1$, the angle only depends on the index of refraction. In this case, pure water ($n \sim 1.33$) yields an angle of 42°.

The amount of energy lost per unit track length via this radiation is given by the expression [89]

$$\frac{dE}{dx} = \frac{(ze)^2}{c^2} \int_{n(\omega)>(1/\beta)} \left(1 - \frac{1}{\beta^2 n^2(\omega)}\right) \omega \, \mathrm{d}\omega, \tag{2.3}$$

which equals approximately 500 eV/cm for the radiation wavelengths relevant to SK (300-600 nm). Note that this loss is small compared to the overall energy loss of charged particles in water due to scattering and ionization, which for minimum ionizing muons is around 2 MeV/cm. The number of photons emitted per unit track length is given by

$$\frac{d^2N}{dxd\omega} = \left(\frac{ze}{c}\right)^2 \frac{1}{\hbar}\left(1 - \frac{1}{\beta^2 n^2}\right). \tag{2.4}$$

For particles such as electrons and muons with $z = 1$, $e = 1$ and $\beta \sim 1$, there are approximately 200 photons per cm emitted along the particle's track in pure water. As will be described in following sections, accurate detection of the timing and quantity of photons will allow reconstruction of Cerenkov rings and thus the direction and energy information of charged particles in SK.

2.3 The SK Detector

The detector consists of a steel cylindrical tank 39.3 meters in diameter and 41.4 meters tall, with a nominal water capacity of 50 ktons. On top of the tank there is a dome area where five huts containing the electronics for the experiment are located. There is a also a control room connected to the dome area by a tunnel that is used for monitoring shifts, as shown in Fig. 2.2. The daytime shift is done form inside the control room, while evening shifts are conducted remotely.

Within the tank is a steel scaffolding structure approximately 2 meters from the outer wall which houses photomultiplier tubes (PMTs) and divides the detector volume into two optically separated concentric cylinders, an inner detector (ID) and outer detector (OD). The structure and PMTs are shown in Fig. 2.4. The OD acts as a veto and is defined by the area extending 2.05 meters inward from the tank walls and 2.2 meters from the tank top and bottom, containing approximately 18 ktons of water. The ID is defined as the inside of the scaffolding and contains 32 kilotons of water. The scaffolding structure itself is 0.55 meters in thickness, which is dead space through which light is not able to pass.

The ID side of the scaffolding is covered in a black low-density polyethylene sheet which absorbs light. This prevents light from leaking from the ID into the OD (and vice versa),

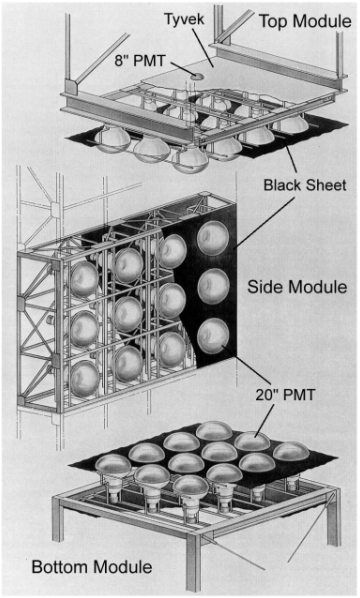

Figure 2.4: The scaffolding structure which divides the ID and OD, along with the mounted PMTs. Taken from Ref. [12]

and also prevents reflected or scattered light from bouncing around the ID. The OD side of the scaffolding and the inside of the outer detector wall are covered with white reflective Tyvek®(manufactured by DuPont) sheets. This increases the light collection efficiency of the OD PMTs. Tyvek has a reflectivity of $\sim 90\%$ for a wavelength of 400 nm.

2.4 PMTs

The photomultiplier tubes housed on the scaffolding act as light-collection detector elements viewing the ID and OD water volumes. PMTs operate by detecting photoelectrons emitted via the photoelectric effect when a photon strikes their photocathode surface. This initial photoelectron is multiplied into a large cascade of electrons by a series of interactions with dynodes at increasingly higher potentials. The gain factor for the PMTs used in SK is about 10^7, which means that 1 photoelectron becomes an output signal of roughly 10^7 photoelectrons after the final dynode (so that 1 input p.e. would produce a charge output of ~ 2 pC).

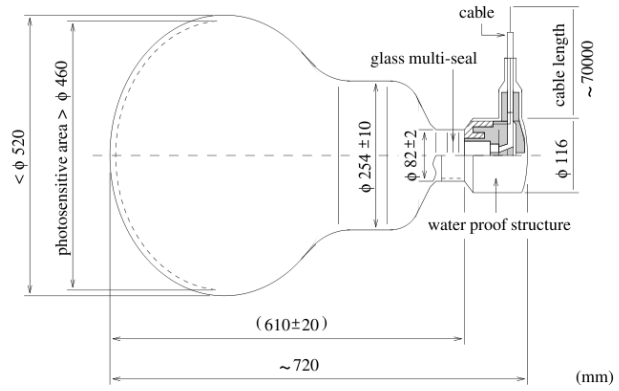

Figure 2.5: Schematic view of an ID 50 cm PMT. Taken from Ref. [12]

The ID contains 11,129 inward-facing Hamamatsu Type R3600-006 PMTs 50 cm in diameter. A schematic of an ID PMT is shown in Fig. 2.5.

The PMTs have a bi-alkali photocathode, with total photocathode coverage of the ID surface of effectively 40%. The number of PMTs and their effective photocathode coverage in the detector was significantly reduced in SK-II due to a major accident in 2001[11]. Reconstruction work between the SK-II and SK-III phases brought the detector back to its original PMT configuration. Additionally, the ID PMTs were placed inside fiberglass enclosures with acrylic hemispheres covering the photocathode surface, to prevent similar accidents in the future.

The ID PMTs have a peak quantum efficiency of about 20% within the range of wavelengths 360-400nm, as shown in Fig. 2.6, and are operated at voltages between 1,700 and 2,000 V. Each PMT has a dynamic range from 1 pe to $\sim$ 1200 pe (to be discussed in more detail in the section about the DAQ, which sets these limits), allowing SK to detect events with energies between 4.5 MeV and over 1 TeV, a wide range of energies spanning from low-energy solar neutrinos to high-energy atmospheric neutrinos. The timing resolution of the ID PMTs is 2-3 ns.

The OD contains 1,885 outward-facing PMTs each 20 cm in diameter. They are a combination of old PMTs recycled from the IMB experiment [56], and new Hamamatsu

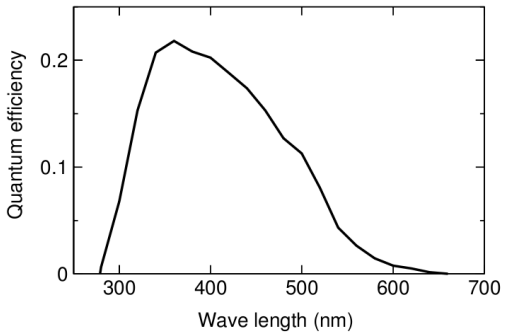

Figure 2.6: Quantum efficiency of the ID PMTs. The peak efficiency coincides with UV radiation wavelengths. Taken from Ref. [12]

R1408 PMTs. The IMB PMTs are concentrated near the top and upper part of the barrel while the majority of the barrel and the bottom of the tank have the new PMTs. Square acrylic wavelength shifting (WS) panels (60 cm per side) are attached to each PMT to enhance the light collection efficiency, achieving an enhancement ratio of 1.5 relative to a bare PMT. The plates absorb UV light and emit blue-green light closer to the sensitivity peak of the PMTs. The timing resolution of the OD PMTs is approximately 15 ns, in part due to the presence of the WS panels. While this is much poorer than the ID PMTs, the extra light collection efficiency it creates is valuable for use as a calorimeter and veto counter.

A magnetic field of 450mG exists naturally in the detector cavity volume. The timing and photoelectric trajectories of the PMTs are sensitive to such a magnetic field. To reduce the field strength, 26 sets of horizontal and vertical Helmholtz coils are placed inside the tank. Their operation reduces the average field inside the detector cavity to about 50mG.

A $\sim$ 70 m coaxial cable is connected to each PMT for the high voltage supply and data transfer. The PMT signals are sent up through these to one of four electronics huts located in the dome area on top of the tank.

2.5 Data Acquisition System

During the first three phases (SK-I, SK-II, and SK-III; 1996-2008) of the Super-Kamiokande experiment, the data acquisition (DAQ) system did not undergo any major upgrades. In 2008, in anticipation of the SK-IV running period and the T2K Experiment[39], the DAQ front-end electronics underwent a complete upgrade. The data analyzed in this work spans all four phases of the experiment. We present a brief overview of the original DAQ system, and a more detailed overview of the new SK-IV system. The reader can refer to Ref. [12] for a more detailed description of the original DAQ system, and Ref. [33] for further details on the specifics of the new SK-IV electronics.

2.5.1 Original DAQ

The original DAQ featured independent PMT readout electronics for the ID and OD PMTs. The ID PMT signals were read out by Analog Timing Modules (ATMs), each of which managed 12 PMTs, located in the electronics huts. Each ATM featured two channels per PMT and switched between the channels to reduce readout dead time. Square wave pulses were created by the ATM upon receiving a PMT signal, and then sent to a global hardware analog-sum "hitsum" trigger. This trigger activated at a threshold of 29 PMT hits. In the event of a global trigger the digitized charge and timing information for each ID PMT was saved for a time window from 400 ns prior to 900 ns after the trigger. The event information was finally sent to offline computers by custom built "TKO" crate interfaces via an optical network. The ATMs were saturated at charge inputs of around 600 pC (a feature which was improved with the new SK-IV system).

The OD PMT signals were readout by "paddle cards", which each handled signals from 12 PMTs. Charge-to-time conversion (QTC) modules produced a square wave with the timing information defined by the leading edge and the overall charge defined by the width. For global OD triggers, information was saved between 10 μs prior to and 6 μs after the trigger.

In both cases, individual PMT signal thresholds were set to 0.25 p.e. This DAQ electronic system was used until the end of the SK-III period in 2008.

2.5.2 New DAQ

The new DAQ system provides a stable setup for the next 10 to 20 years and many direct benefits to SK physics analyses. To lower the energy threshold for solar neutrino studies, a high-speed DAQ is necessary to combat the increase in background rates. Also, a supernova burst in the galactic center could produce tens of thousands of events in SK in a 10s time window. The original DAQ was capable of recording approximately 60,000 events in this time span, but the new DAQ increases that capacity by a factor of 100. The new dead-time free system also allows all PMT hits to be recorded. In the original system only PMT hit information within the defined global trigger windows was recorded. This feature also has benefits for supernova relic neutrinos studies. These events are distinguished from atmospheric neutrino background events by a 2.2 MeV gamma ray emitted with a 200 μs delay from neutron capture following the initial neutrino interaction. It becomes possible to apply software triggers to select these special events because all PMT hit information is recorded in the new system. A much larger dynamic charge range also raises the saturation level, which benefits higher-energy neutrino studies.

The ATM boards in the ID are replaced by QBEE modules, which stands for "QTC (charge-to-time converter) Based Electronics with Ethernet". Each QBEE board collects analog input signals from 24 PMTs. The QTC outputs a digital pulse with the leading edge defining the timing information and the pulse width defining the total charge. The pulse information is read out to the on-line computers by Ethernet cables using the TCP/IP protocol. This greatly improves the transfer time for data and eliminates bottlenecks which were sometimes caused by the (custom-built) TKO readouts in the original DAQ. The same QBEE electronics were used for the OD PMTs as well. Although the OD boards were new, the QTC readout principle was carried over from the previous OD setup.

The analog sum hardware trigger has been replaced by a software trigger that records all PMT hits. Event windows are defined by a 60MHz master clock which continuously applies a periodic 17μs trigger to the QBEEs. The data readout rate which is necessary to save all hits is 1.5MB/s/QBEE, which is easily achieved by this system. A schematic diagram of the new system with the QBEEs and master clock is shown in Fig. 2.7. A schematic

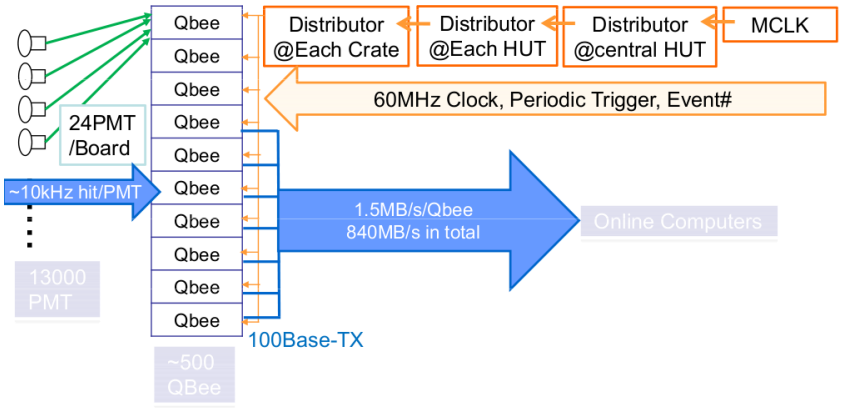

Figure 2.7: A schematic of the new DAQ system. Taken from Ref. [33]

showing the new periodic software trigger system is shown in Fig. 2.8.

The timing resolution of the QBEEs at the 1 p.e. signal level is 0.3 ns. This timing resolution is much better than the 2.8ns timing resolution for the 50cm (20 inch) ID PMTs at the same charge level. A plot of the timing resolution for the QBEE and the PMT as a function of input charge is shown in Fig. 2.9. The QBEEs also feature a much improved dynamic charge range. There are three input channels per chip, each with three gain ratios of $1 : \frac{1}{7} : \frac{1}{49}$, combining to give a dynamic range from 0.2 pC to 2500 pC. A timing chart for the process of converting a raw PMT current signal to a digital output signal by the QTC is shown in Fig. 2.10. As shown the built-in discriminator is used to produce a QTC out signal with the hit timing (leading edge) and charge (pulse width) information encoded. The process time is about 1 μs/hit.

The QBEEs also feature the high-speed processing necessary for recording all the data in a supernova burst event. A high-rate test was performed by feeding the same signal into the QBEE and no data loss was seen up to frequencies of 130 kHz, as shown in Fig. 2.11. This represents a factor of 100 improvement over the original DAQ readout.

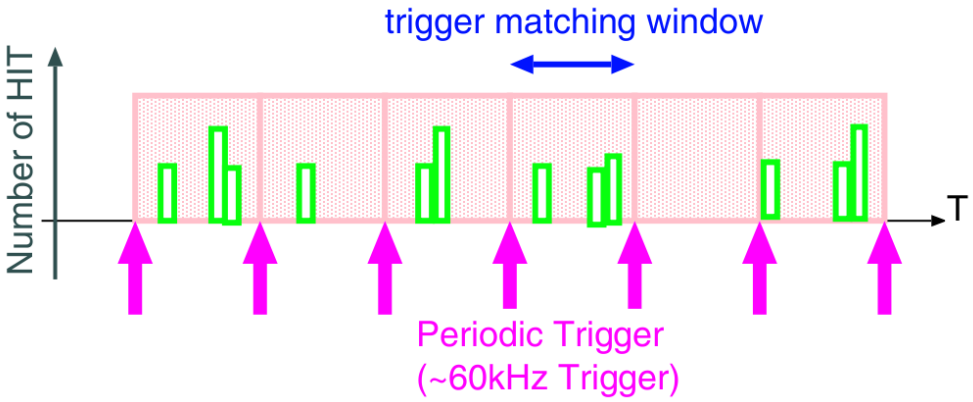

Figure 2.8: A schematic of the new periodic software trigger. Taken from Ref. [33]

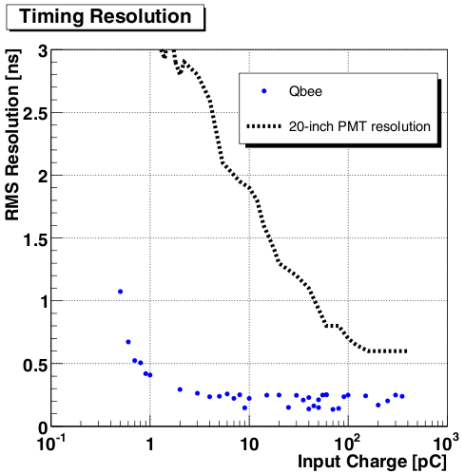

Figure 2.9: A schematic of the timing resolution as a function of input charge for a QBEE and ID PMT. Taken from Ref. [33]

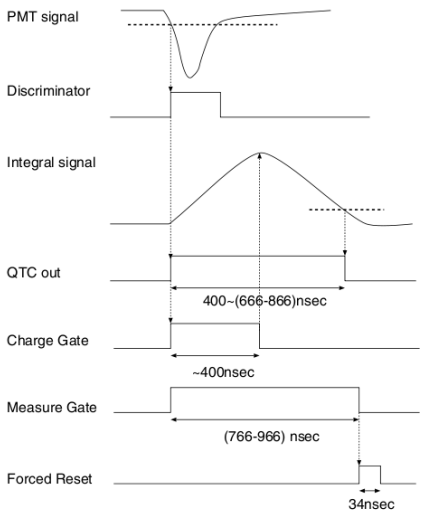

Figure 2.10: Timing chart for QTC processing of raw PMT signal. Taken from Ref. [33]

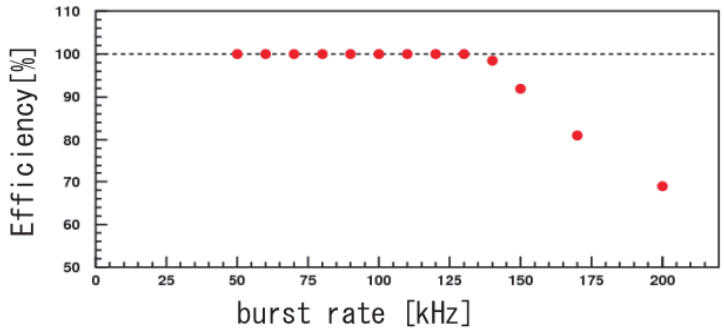

Figure 2.11: The high-speed processing rate of the QBEEs. Frequency of the input signal is on the horizontal axis. Taken from Ref. [33]

Trigger	SK-I	SK-II	SK-III	SK-IV	SK-IV Average Rates
SLE	-260 mV	-110 mV	-186 mV	-196 mV	3260 Hz
LE	-320 mV	-152 mV	-302 mV	-324 mV	36 Hz
HE	-340 mV	-180 mV	-320 mV	-300 mV	11 Hz
OD	19 hits	19 hits	19 hits	19 hits	3 Hz

Table 2.1: A summary of each analysis trigger threshold for each detector period, along with the average trigger rates for SK-IV.

2.5.3 Trigger

The SK-I,-II, and -III detector configurations used a hardware hitsum for the analyses triggers. With the new SK-IV electronics, a new software trigger is used that selects trigger events after saving all hit information. In both setups, four analyses triggers were defined: three ID triggers (super-low energy [SLE], low energy [LE], and high energy [HE]) and an OD trigger. The SLE and LE triggers are used mainly for solar neutrino events and SN relic events, while the HE trigger is mainly used for atmospheric neutrino and high-energy cosmic ray muon events. The OD trigger threshold is defined within a 200 ns coincidence window. The SLE threshold is limited from below by backgrounds such as rock wall and PMT glass radioactivity which increase as the threshold decreases. All trigger thresholds were decreased during SK-II to reflect the reduced photocathode coverage. A summary of the thresholds and approximate trigger rates for each analysis trigger in each run period are shown in Table 2.5.3.

2.6 Air Purification

Radon in the mine air (from the U/Th decay chain) can decay and the products can become a low-energy background for the experiment. It can also be a health hazard to people working in the mine, at more extreme levels. Natural levels of radon vary throughout the year, ranging from about 200 Bq/m^3 to 3,000 Bq/m^3 depending on the season. Multiple actions

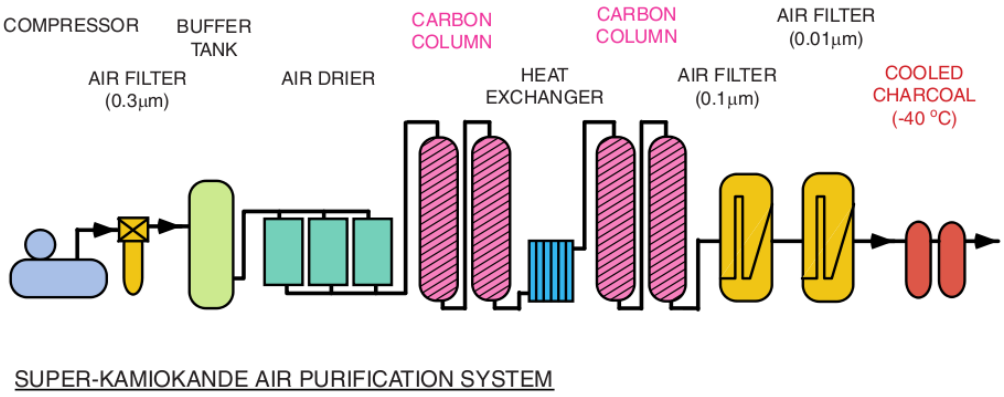

Figure 2.12: Schematic view the radon-free air system. Taken from Ref. [5]

are taken to minimize this. The mine cavity surface is coated with MineGuard®(made by Urylon), a radon-tight paint. Additionally, a radon-free air system is housed just outside the entrance to the mine. An air blower takes radon-free air from outside the mine and pumps it into the mine at a slight over-pressure at a rate of about 10 m^3/min. This system maintains a Radon level of about 40 Bq/m^3 in the dome and control room areas. A schematic of the air purification system is shown in Fig. 2.12.

2.7 Water Purification

Maintaining very pure water inside the tank is crucial to the successful operation of a water Cerenkov detector. A water purification system is used which continuously recycles the water in the tank. It is a closed cycle system which processes water at a rate of approximately 60 metric tons per hour. Water is passed through the same purification system when refilling the detector as well, but with raw mine water used as the source. Water is supplied to the bottom of the ID, and removed at the top and bottom of the OD, as well as the top of the ID. This flow is chosen to minimize the stagnation of water in the tank. A schematic of the water system is shown in Fig. 2.13.

Water from the SK tank is initially passed through 1 μm mesh filters to remove particulate matter. This prevents reduction of transparency for Cerenkov photons. The water

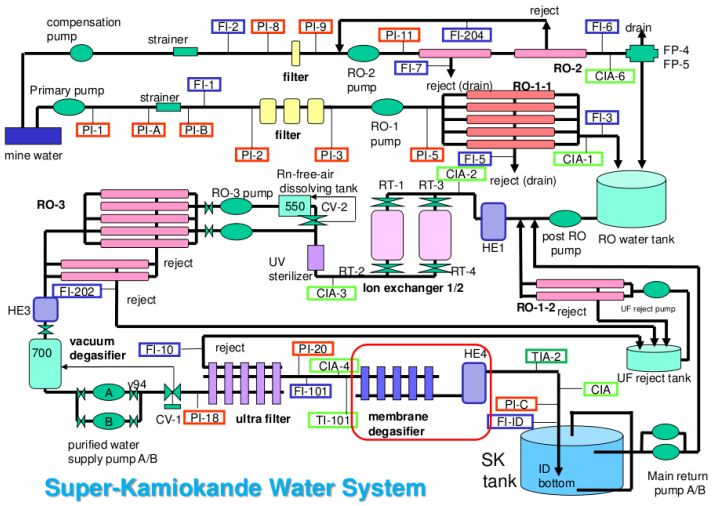

Figure 2.13: Schematic view the water purification system.

also passes through two heat exchanges, which cool the water to about 13 °C. This reduces the dark noise rate of the PMTs and also suppresses growth of bacteria which can further reduce water transparency. A UV sterilizer is used to kill any remaining bacteria.

Rn-reduced air is dissolved into the water, and a vacuum degasifier is used to remove dissolved radon and oxygen gas. Radon gas is removed with $\sim 96\%$ efficiency at this stage. An ultra filter removes particles down to about 10 nm in diameter. Finally a membrane degasifier removes remaining radon gas dissolved in the water with more than 80% efficiency. The water system underwent an upgrade in 2012 (the upgraded system is shown in the figure) to supply colder water to the SK tank. The water temperature exhibits an anti-correlation with the transparency length, so colder water is better for reducing absorption of Cerenkov light. A new He-4 heat exchanger and membrane degasifier were installed in the system, shown in the red box in the schematic. The temperature of the water in the tank is slightly above 13 °C.

Chapter 3

CALIBRATION

3.1 Introduction

It is essential for the detector response to be well known so that the data can be accurately analyzed. Many types of calibration are performed in the detector to measure its response. In these calibrations a known source of light is used to simulate events in the detector and the output is compared to expectations. The following are some of the main calibration tests.

3.2 Water Calibration

3.2.1 Laser absorption and scattering

The ability of SK to operate as a water Cerenkov detector relies on having pure water with well-understood transparency, absorption and scattering properties. First, the water's index of refraction was modeled by a complicated function which calculated the effective index as a function of wavelength as shown in Fig. 3.1. As seen in the figure the index of refraction varies between 1.33 and 1.36 for the Cerenkov radiation wavelengths of interest.

Additionally, a propagation model for light in the tank water including the effects of absorption and scattering was developed. These effects reduce the intensity of light as it travels in the water. Intensity as a function of distance traveled is given by

$$I = I_0 e^{-\frac{L}{WT}}. \tag{3.1}$$

In this expression L is the distance traveled by the light, WT is the water transparency parameter (the inverse of the attenuation length) including scattering and absorption effects, I_0 is the original light intensity, and I is the intensity after traveling a distance L. The goal of the calibration described here is to estimate the water transparency parameter WT. This

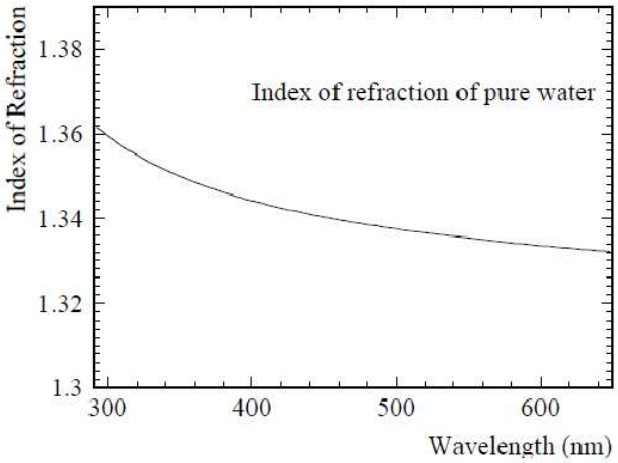

Figure 3.1: The index of refraction of the SK tank water modeled as a function of light wavelength.

parameter is defined as

$$WT(\lambda) = \frac{1}{\alpha_{sctt}(\lambda) + \alpha_{abs}(\lambda)}. \tag{3.2}$$

The parameters α_{sctt} and α_{abs} in this expression have units of 1/m. Light scattering is modeled to include both Rayleigh and Mie scattering. Rayleigh scattering applies to wavelengths of light that are much larger than the size of the scattering object (a water molecule, for example), whereas Mie scattering applies when the two length scales are comparable to each other (for example, light scattering from a large impurity in the water). The scattering parameter can then be divided into these two components, as given by

$$L_{atten} = WT(\lambda) = \frac{1}{\alpha_{Ray}(\lambda) + \alpha_{Mie}(\lambda) + \alpha_{abs}(\lambda)}. \tag{3.3}$$

However, for actual calibration measurements the scattering parameters are most easily separated by their angular distributions. Fig. 3.2 shows the scattered light angular distribution from symmetric (left) and asymmetric (right) scattering, respectively. Light from Rayleigh scattering obeys the left distribution, and that from Mie scattering is approximately described by the sum of both distributions. Thus, the water transparency

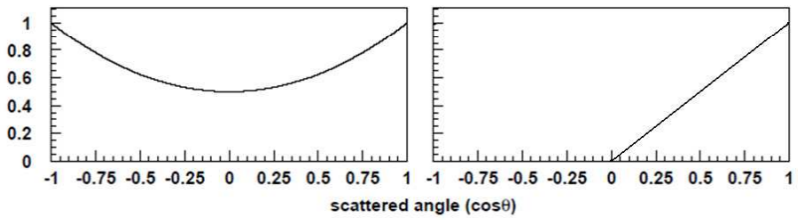

Figure 3.2: Angular distribution of scattered light from symmetric (left) and asymmetric (right) scattering.

parameter can be rewritten as

$$WT(\lambda) = \frac{1}{\alpha_{sym}(\lambda) + \alpha_{asy}(\lambda) + \alpha_{abs}(\lambda)}. \tag{3.4}$$

Each of these α coefficients are found to have λ^{-4} dependence to leading order, and the absorption parameter has an additional term which dominates at longer wavelengths (it has a complicated functional form that is plotted in 3.5).

For this calibration measurement, a set of eight laser light injectors which send laser light of tunable wavelengths into the SK tank via an optical fiber were used. A schematic showing the positions of these injectors in the detector is shown in Fig. 3.3.

Wavelengths of 337, 365, 400 and 420 nm produced by a nitrogen laser (337 nm wavelength) combined with wavelength-shifting laser dyes for were used in this system for SK-I, -II and -III. For SK-IV, the system was updated, replacing the nitrogen/dye laser system with a laser diode (LD) system. The new wavelengths in the SK-IV LD system were 337, 375, 405 and 440 nm. An event display for a sample laser injection event is shown in Fig. 3.4 As shown in the figure the laser light is not passed through a diffuser, so the majority of the light causes PMT hits at the bottom of the detector. The other PMT hits in the event are caused by either backgrounds (PMT dark noise, for example) or scattered light.

The hit and timing distributions of the laser light data were used to tune the water parameters until sufficient agreement was seen with MC simulation events. The results of the measurements of the scattering and absorption parameters are shown in Fig. 3.5. The inverse of the overall water transparency parameter is shown by the black line in both plots.

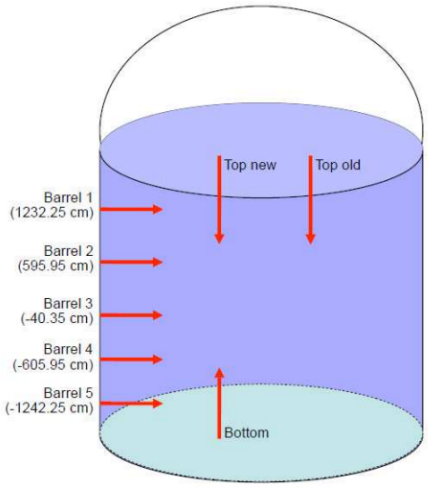

Figure 3.3: The positions of the eight laser light injectors in Super-Kamiokande. "Old" refers to the sole original injection point used in SK-I.

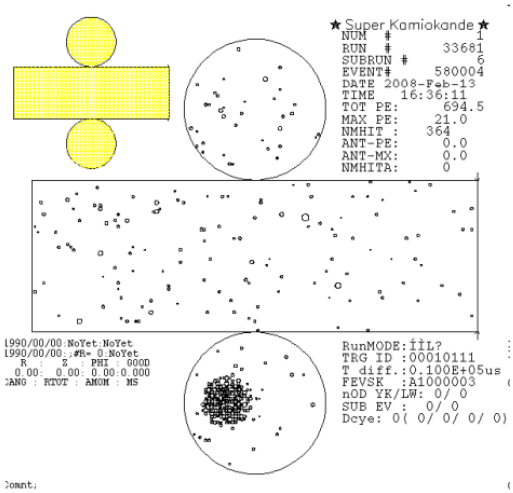

Figure 3.4: A typical laser light injection event (injected from the top of the tank).

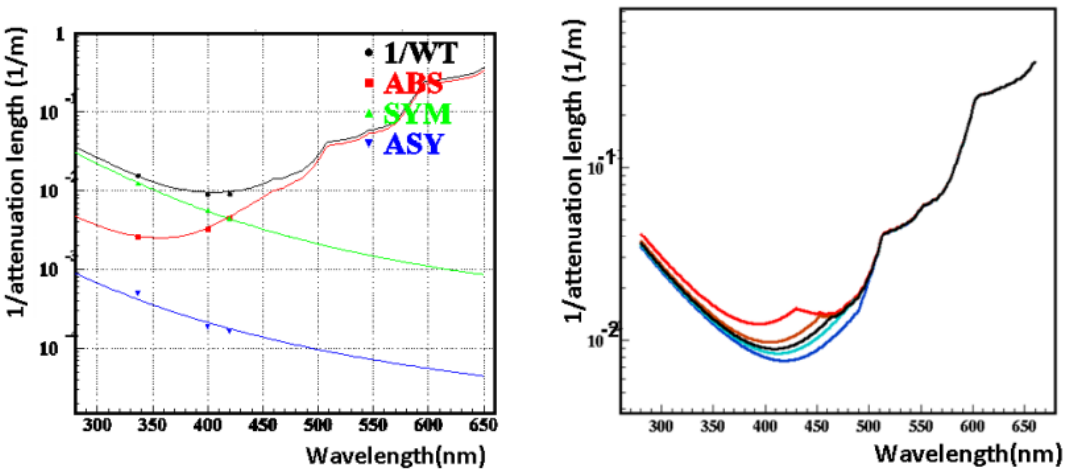

Figure 3.5: Measurement of the water parameters for scattering and absorption.

An attenuation length of approximately 100m was achieved for SK-IV.

3.2.2 Cosmic ray muons

Downward-going cosmic ray muons also serve as a calibration tool for measuring water transparency. These particles are the majority of HE triggers in the SK data and occur at a rate of a few Hz. They are typically minimum ionizing particles which deposit energy (mostly through ionization) steadily at a rate of about 2 MeV/cm, independent of their energy. One advantage of using cosmic ray muons over laser events is that the measurement with cosmic ray muons is naturally averaged over the spectrum of Cerenkov radiation, instead of a monochromatic distribution. The detected number of photo-electrons is given by

$$Q = Q_0 \frac{f(\theta)}{l} e^{-\frac{l}{L_{atten}}}. \tag{3.5}$$

where Q_0 is a constant, $f(\theta)$ is the PMT acceptance (geometric photosensitive area), l is the photon path length, and L_{atten} is the attenuation length. A schematic showing the path length of the photons and their arrival angle θ at the PMT is shown in Fig. 3.6.

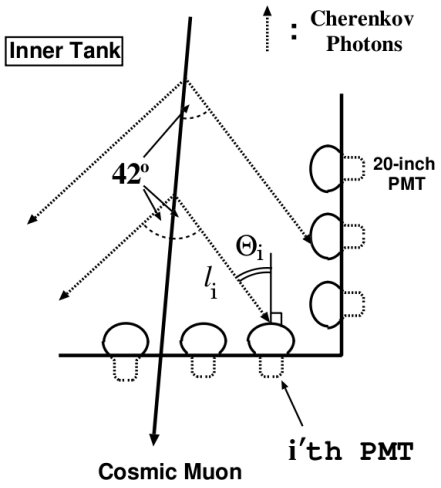

Figure 3.6: Cosmic ray muon water transparency measurement schematic.

The detected charge is measured over the angle θ and plotted as a function of the path length that the light took to reach the PMT. This plot is then fit for the normalization factor Q_0 and attenuation length L_{atten}. The attenuation length measured from these studies is found to vary between 80 and 90m for SK-IV. The plot for SK-IV is shown in Fig. 3.7. This is comparable to the measured values found for SK-I,-II, and -III (see Ref. [109] for more details).

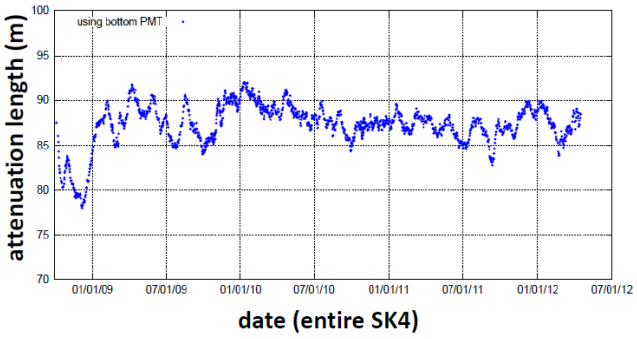

Figure 3.7: Thru-mu measurement of attenuation length for SK-IV.

3.2.3 Water quality position and time dependence

The SK water quality has a position and time dependence because of the flow from the water circulation system. For the position dependence, a top-bottom asymmetry in the water is measured by a monthly calibration with a Ni-Cf source positioned at three heights (Z = +12m, 0m and -12m) in the detector. The PMT hit rates are found to be a few percent lower near the top of the tank than near the bottom [38]. A xenon lamp connected to a scintillator ball is also used as a complementary measurement of the position dependence. These light sources are regularly used to monitor the time dependence of the water quality as well. More details can be found in Ref. [12].

3.3 Charge calibration

In addition to the water properties, a thorough understanding of the response of the PMTs to the Cerenkov radiation photons is necessary for precise event energy reconstruction and MC simulation. As described in the previous chapter, PMTs amplify photo-electron signals (the amplification factor is the "gain" of the PMT) and send the amplified signal to the readout electronics. The following sections describe calibration studies done to understand the charge and timing properties of the PMT signals.

3.3.1 HV determination

The charge response of the PMT for a given amount of light must we well understood for sufficiently accurate energy reconstruction. The response can be quantified by the gain and quantum efficiency (QE) values. The gain of each PMT is controlled by the amount of HV supplied to the dynodes. Generally, the relationship between supplied HV and gain for a PMT is given by

$$\text{Gain} \propto \alpha \text{HV}^{\beta} \tag{3.6}$$

where α and β are unique to each PMT. The gain calibration includes measurements of average and individual PMT gains, respectively. PMT gains can in general be determined from the single photo-electron response to the Nickel γ-ray calibration source. The general

principle is to first adjust PMT HV values so that the output charge, Q_{obs}, from each PMT (after corrections for the number of p.e.s detected) is uniform across all PMTs. The output charge can be calculated by the expression

$$Q_{obs} \propto N_{photon}(i) \times QE(i) \times Gain \tag{3.7}$$

where N_{photon} represents the number of photons striking the photo-cathode, QE represents the quantum efficiency, and i represents the ith PMT. After adjusting the HV to achieve sufficient uniformity, additional independent measurements were made of the PMT gains and quantum efficiencies. These serve as necessary inputs for the MC simulation of the detector.

A group of "standard PMTs" were calibrated so that their output charges matched each other to within 1.3% before installation in the ID. This so-called "pre-calibration" was done in 2005 before the start of SK-III data-taking. In total 420 PMTs were calibrated by placing them in a dark box with a Xe lamp source passed through a UV filter (passing only light with $\lambda < 400$nm) and then a scintillator ball. The HV of each of these PMTs was adjusted so that the charge output matched that of a reference avalanche photodiode (APD).

The locations of the standard PMTs in the ID are shown in Fig. 3.8. All ID PMTs were grouped together (25 groups in total, such that 9-12 standard PMTs were included in each group) and the charge responses to the calibration light sources were matched to the average charge response of the standard PMTs within that same group. This reduced uncertainties due to water quality and photon propagation for PMTs located in different areas in the ID. Light flashed from the Xe lamp was passed through the UV filter and scintillator ball. The scintillator ball was positioned in the center of the talk and rotated around its vertical axis to account for any spherical asymmetry. Each PMT received roughly 50 p.e.s per flash of light. A schematic of the setup showing the scintillator ball and a sample group of PMTs is shown in Fig. 3.9.

The corrected charge, Q_{corr}, observed at each PMT was then calculated from the observed charge, Q_{obs} with the expression

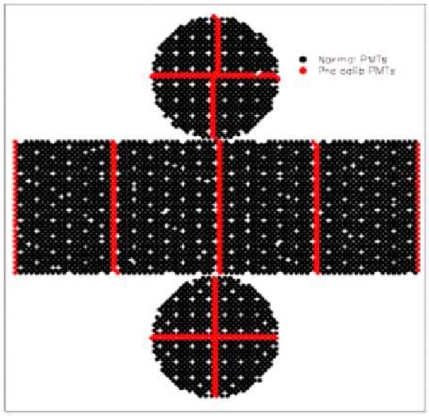

Figure 3.8: The installed locations of the standard PMTs (shown in red) within the ID.

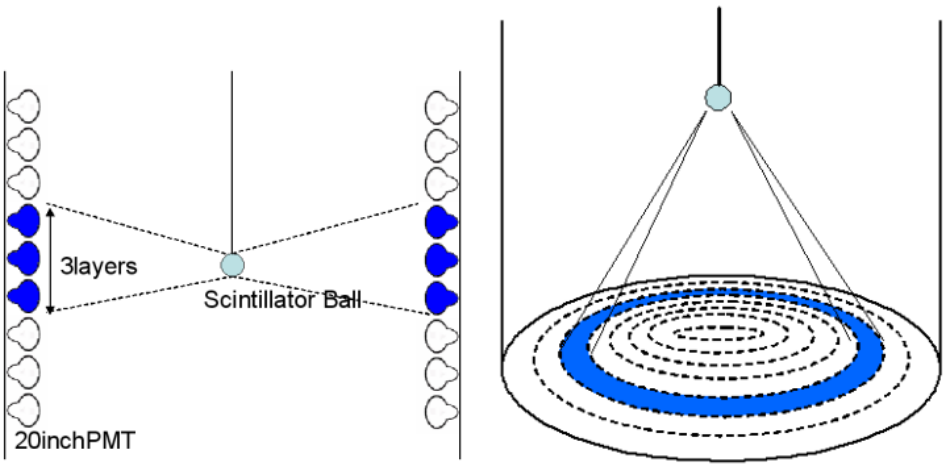

Figure 3.9: The scintillator ball setup for the PMT HV determination. A sample grouping of PMTs calibrated together is shown in blue.

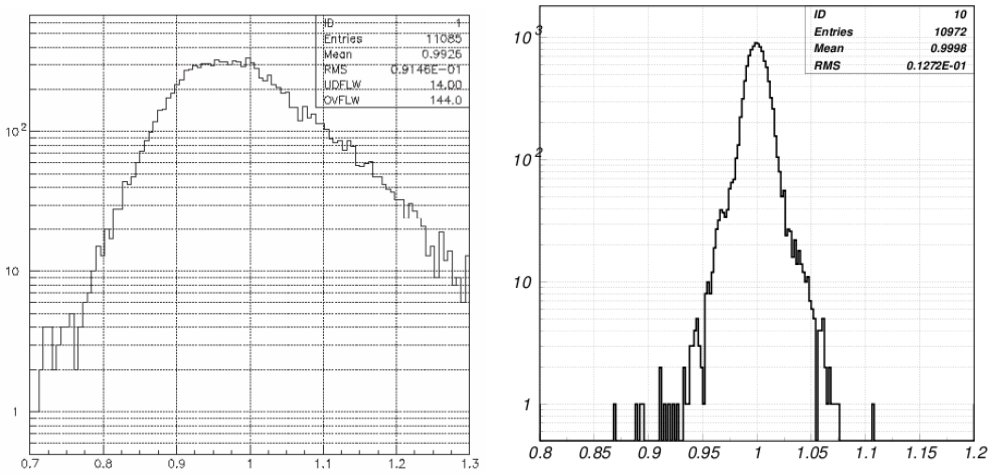

Figure 3.10: The ratio of each PMTs corrected charge to the target charge (mean corrected charge of standard PMTs) before (left) and after (right) HV adjustments.

$$Q_{corr} = \frac{Q_{obs} \times r^2}{f_{accept}(\theta)} \tag{3.8}$$

where r is the distance from the scintillator ball to the PMT and θ the angle from the PMT to the scintillator ball. The HV for each PMT was adjusted so that the corrected charge equaled that of the average of the standard PMTs within the same group. The results of this calibration can be seen in the contrast of the left and right plots in Fig. 3.10. The figure demonstrates that after the tuning the variation of observed charge relative to the standard charge decreased significantly. The observed charges for all PMTs were equal to each other within 1.3% after this calibration procedure, compared to almost 10% beforehand.

3.3.2 Absolute gain calibration

An overall "absolute gain" calibration was also updated for SK-IV and compared to previous detector configurations. A photon source called the "nickel" source was used for this measurement. It was made up of a source of Californium (^{252}Cf) surrounded by a spherical mixture of NiO (6.5 kg) and polyethylene (3.5 kg). The spontaneous fission of the ^{252}Cf source produces neutrons which are then thermalized (brought to thermal equilibrium) by

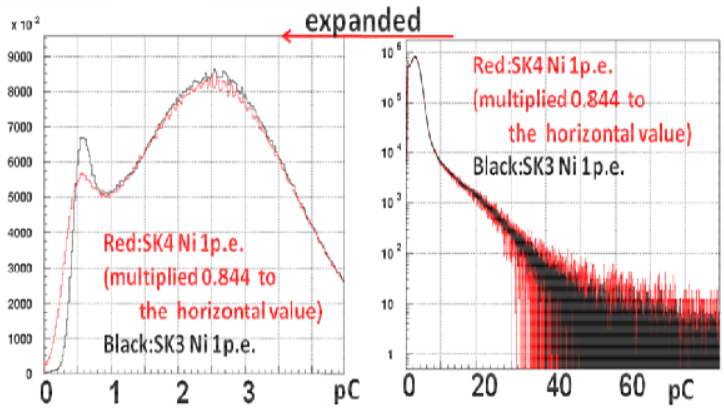

Figure 3.11: The single p.e. distributions for SK-III (black) and SK-IV (red, adjusted by scaling factor) shown for two different horizontal scales (left and right).

the polyethylene. After thermalization the neutrons can be captured by the nickel, producing gamma rays of about 9 MeV through the process Ni(n,γ)Ni (where the initial and final Ni elements are different isotopes). Each of these gamma rays subsequently produces about 100 photons detected by the PMTs. The energy of these events were low enough that the probability of PMTs receiving detecting only a single p.e. was very high. The nickel source was positioned near the center of the SK tank for the measurement.

The resulting 1 p.e. distribution for SK-IV was similar to that of SK-III, with some differences in the low charge tail region. The QTC chips on the new SK-IV QBEE boards had a poorer resolution in the low charge per p.e. region than that of SK-I through SK-III, so the SK-IV single p.e. distribution was adjusted to overcome this. The SK-IV single p.e. data were multiplied by a factor of 0.844, which gave agreement between the SK-III and SK-IV peaks. The SK-III and corrected SK-IV distributions are shown in Fig. 3.11.

From this measurement the conversion factor between p.e. input and final PMT charge output can be determined. This is the "gain" factor that was the goal of the measurement. This scaling factor is given the name "pC2pe". It represents the amount of charge in units of pC generated as the output signal from 1 input p.e., or in other words the gain (note that this value is consistent with the rough estimate of the gain of the PMTs of $\sim 10^7$

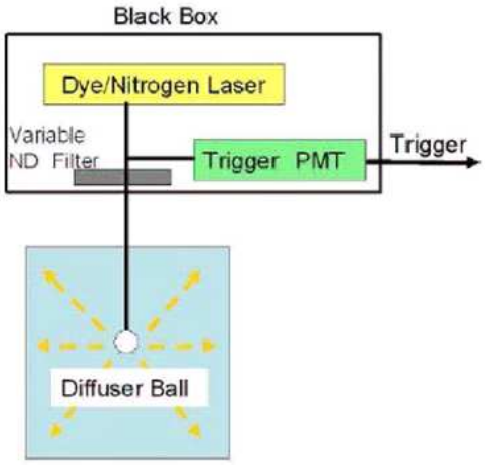

Figure 3.12: A schematic of the setup used to measure the relative PMT gains.

quoted in the previous chapter). For SK-IV the global pC2pe value was found to be 2.658. This differed from the corresponding SK-III value, 2.243, by the scaling factor which was mentioned above.

3.3.3 Relative gain calibration

The relative gain calibration describes the individual PMT response relative to the average response described in the previous section. The setup for this measurement is shown in Fig. 3.12. A dye/nitrogen laser connected to a diffuser ball was used as the light source. As with all other calibration measurements the light source was partially redirected to a dedicated trigger PMT which indicated exactly when the source was flashed.

The relative gain for each PMT can be determined from the ratio

$$\text{Gain}(i) \propto \frac{Q_{obs}(i)}{N_{hit}(i)} \tag{3.9}$$

where i is the i-th PMT, Q_{obs} is that PMTs observed charge, and N_{hit} is the number of photons reaching the PMT cathode. Thus, the calibration measurement should give both values in the RHS of this equation. This value was then normalized by the mean value over all PMTs, giving the relative gain. The measurement was taken twice, with the

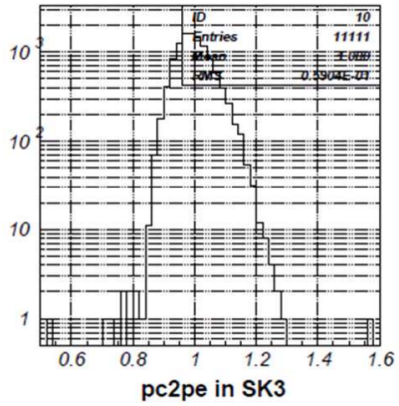

Figure 3.13: The distribution of relative gains for all ID PMTs after normalizing to mean 1.

light set to low and high intensities, respectively. This was done to get around the fact that individual PMT hits in a low-intensity setup could be from background and therefore cannot be guaranteed to be coming from the light source (this was not a problem in the absolute gain measurement described previously because the data were not studied separately for individual PMTs.) The low intensity produced 0.3 [hit/event/PMT] and the high intensity produced 50 [pe/event/PMT], on average. The charge observed by each PMT for the high intensity run was the numerator for 3.9, while the number of hits in the low intensity run was the denominator. The distribution of this quantity divided by the mean of the value from all PMTs is shown in Fig. 3.13. This information served as input to the detector MC simulation.

3.3.4 QE measurement

The quantum efficiency, or QE, was defined as the fraction of photons incident on the PMT cathode which produced a p.e. detected by the dynodes and subsequently read out by the electronics. The nickel gamma-ray source introduced previously was used to measure the hit rate of each PMT for this measurement. As mentioned above, each gamma-ray emission resulted in about 100 detectable photons, so the probability of PMTs measuring multiple

hits was very low. In this case the QE is proportional to the measured hit rate. The PMT hit rate was adjusted by MC predictions of the number of photons expected to reach the PMT, to account for the remaining uncertainty in the number of photons reaching each PMT.

Several selection cuts applied to the data from these events reduced unwanted backgrounds. Only events with reconstructed vertices near the nickel source (¡ 400cm away, because the gamma ray is expected to produce photons near its emission point), time differences $> 5\mu$s after the previous event (to remove noise), and passing other various selection cuts were selected. The resulting distribution of PMT hit rates from this calibration is shown in Fig. 3.14. In this figure the blue dots represent the calibration data and the red dots the detector MC simulation. The top plot shows the hit rate distribution of barrel PMTs with the vertical position (z) along the horizontal axis. The bottom left and right plots show the distribution for top and bottom PMTs, respectively, as a function of square of the distance from the center (cm^2). As seen in these plots the hit rate differs from 1 for some PMTs near the edges of the tank. This is from photon reflections off of neighboring PMTs and water scattering. However, the figure also shows that the MC simulation correctly reproduces these tank edge PMT effects.

3.3.5 PMT calibration consistency check

So far calibration of the PMT HV values and independent measurements of the gain and QE for individual PMTs have been described. A further measurement was made to test the consistency of these PMT calibration steps. The "diffuser ball" source was placed at the center of the tank and used as the light source. The charge observed by each PMT from this source was corrected for the distance and acceptance angle relative to the source. This corrected charge was then divided by the QE and relative gain factors as measured in previous sections. The resulting distribution of normalized, corrected charge is shown in Fig. 3.15 for the PMTs divided by their locations. The plot was mostly flat around 1.0, confirming the consistency of the calibration, while indicating a very slight top-bottom asymmetry of less than 1%.

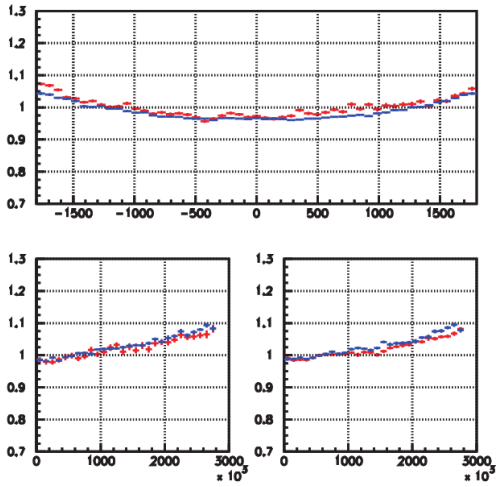

Figure 3.14: The distribution of PMT hit rates for the barrel (top plot), top (bottom left) and bottom (bottom right) PMTs. The blue is the calibration data and the red the MC simulation data.

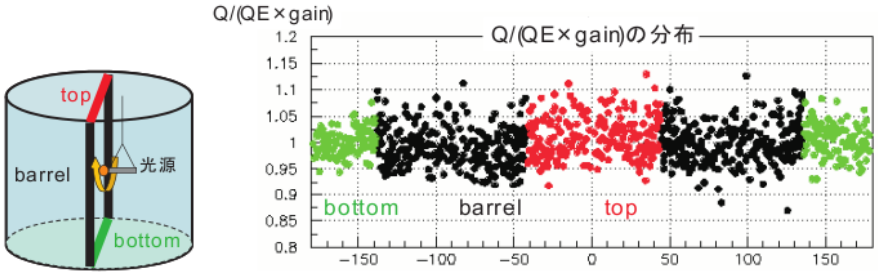

Figure 3.15: The corrected charge divided by the QE and gain for PMTs divided geometrically.

3.3.6 QBEE Charge non-linearity

The linearity of the charge response of the PMTs with the new SK-IV QBEE electronics was also measured. The linearity was defined as the ratio of the observed charge to the expected charge across as a function of increasing charge. The new QBEE electronics had a wide dynamic range, capable of processing an input range of 1-1000 p.e.s. The response linearity in this entire range was investigated. In the SK-I,-II and -III detector configuration, the original electronic readout boards (ATMs) exhibited a $\sim 6\%$ systematic upward shift in the output charge introduced in the analog-to-digital conversion process. This was corrected for by applying a scaling function to the output charge. The measurement described here examined the existence of a similar effect in SK-IV. The nitrogen laser connected to the diffuser ball was used as a light source.

First special monitor PMTs, whose outputs were connected directly to ADCs with well-known response characteristics, were chosen as references. The monitor PMTs were illuminated by the diffuser ball at various gain settings and various distances from the light source (to get data at a range of charge outputs), and their linearity as a function of charge was confirmed. After confirming their linearity, their response to the light was used in each calibration event to determine the expected charge for all other PMTs.

Next, normalizing runs where the diffuser ball light inside the tank was adjusted so that the output of each PMT was around the 10 p.e. level were completed. This established a base output charge ratio between each PMT and the monitoring PMT for that run, to account for geometric acceptance and location variation. To check each ID PMT/QBEE's linearity, the laser source was flashed many times, and the mean output charge per event Q_{mean} was recorded for each PMT. The ratio of this mean output charge to the expected charge should be a constant value of 1.0 independent of the charge level for a perfectly linear PMT/QBEE response. The expected charge Q_{exp} was determined by the monitor PMT Q_{mon} and the normalizing run data and was given by the expression

$$Q_{exp}^{(i,m)} = Q_{mon}^{m} \times \frac{Q_{mean}^{(i,n)}}{Q_{mon}^{(n)}} \tag{3.10}$$

where m is the calibration run index, i the PMT index, and n the normalizing run

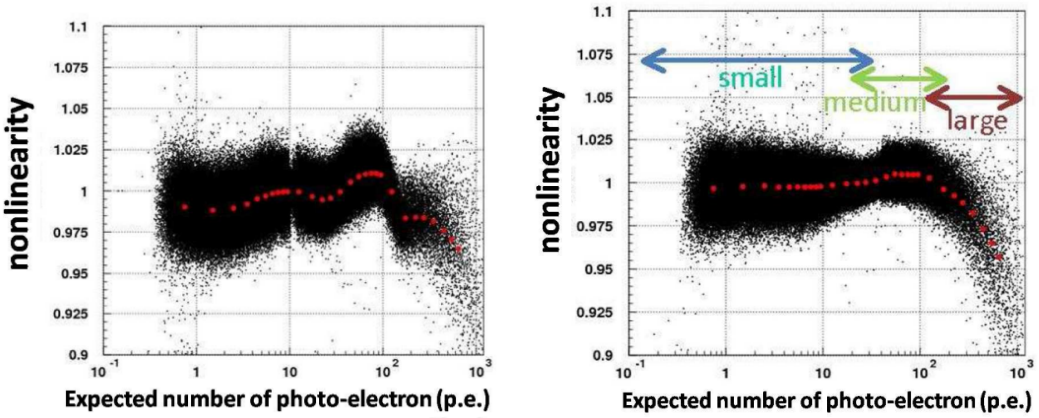

Figure 3.16: The nonlinearity as a function of expected charge for ID PMTs before (left) and after (right) multi-hit correction. The red points show the average of the black points at the corresponding horizontal charge bin.

index. The result of the ratio as a function of expected charge for all PMTs is shown in the left-hand plot of Fig. 3.16. The linearity value varies from 1.0, especially at higher expected p.e. levels.

This variation is caused by two separate effects. The first comes from the QBEE and occurs when the input signal is read in by more than one channel (of the three possible channels) on the QBEE board. The second comes from the PMT itself, for which nonlinearity of about 2% of greater appears at high expected charge levels. The latter effect cannot be easily corrected, but for the QBEE multi-hit effect a correcting function was applied and the corrected result is shown in the right-hand side of Fig. 3.16. As shown the linearity is maintained to within ±1%, the desired level for data-taking. The data in the high charge region in these plots is bounded from above by QBEE saturation, which sets in at around 1200 p.e.

3.4 Timing calibration

The relative timing of the PMTs is also important for accurate reconstruction of event vertices and directions. The time elapsed between Cerenkov radiation emission and the complete readout of event information includes the Cerenkov photon time of flight (the

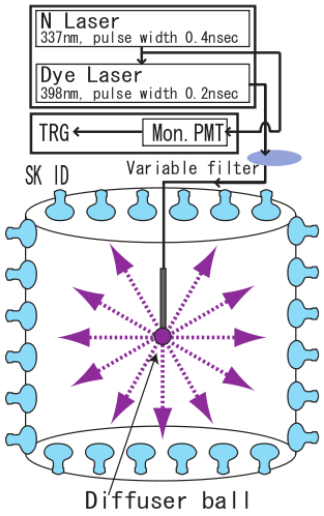

Figure 3.17: The setup used for the timing calibration measurement.

time for the photons to travel from their emission point on the charged particle's track to the PMT surface), the time for the photoelectron avalanche to pass through the PMT, travel the length of the cable from the PMT to the QBEE, and finally be collected and read out by the QBEE boards. The time interval between the photon hitting the PMT and the global trigger not only differs for each PMT, but also exhibits a dependence on the charge of the event (termed the "time walk") due to the fact that events with more charge pass the QBEE discriminator threshold level sooner than events with less charge.

The goal of this calibration is to measure these time intervals for each PMT as a function of charge (from 0 p.e. up to QBEE saturation) with a calibration light source, model the distribution in the time-charge plane (the "TQ Distribution") by a polynomial function (the "TQ Map"), and then make a correction table which applies to each PMT so that the hit timing is a constant value independent of event charge. The N_2/dye laser is pulsed in short bursts, split and redirected to a monitor PMT for event triggering, passed through a filter which varies the light intensity and then spread out in the tank via the diffuser ball. A schematic is shown in Fig. 3.17.

A sample TQ distribution for a PMT channel before corrections from the TQ Map is

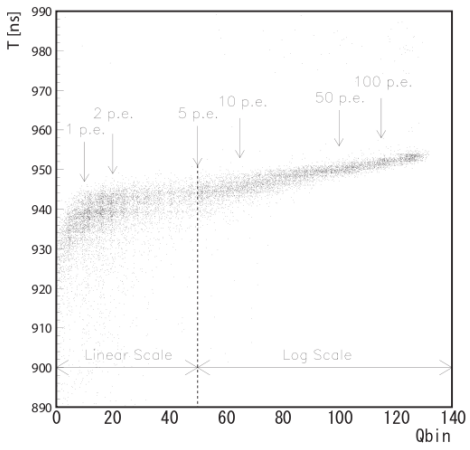

Figure 3.18: A typical TQ distribution before correcting with TQ Map table.

shown in Fig. 3.18. Note here that smaller values correspond to hits later in time because the axis represents time elapsed between the hit and the eventual global trigger. For each charge bin, Q_{bin}, on the horizontal access, scattering and reflection causes a vertical spread of time intervals. To make the TQ Map, the hit times in each bin are fit to a Gaussian to find the peak and standard deviation. The values of these peaks times for each charge bin are used to fit a seventh-order polynomial to all data points.

3.5 Energy scale

3.5.1 LINAC

Super-Kamiokande operates a LINAC on top of the tank to create electrons of known energies and sends them into the tank via a pipe whose endpoint position can be adjusted. This calibrates the absolute energy scale for lower energies (solar neutrinos, etc.) because the LINAC electrons have energies in the range 5-16 MeV. The accuracy of the absolute energy scale is found to be better than 1% with this measurement. This section will focus on calibration studies done at higher energies, so for more details on this the reader can refer to Ref. [51].

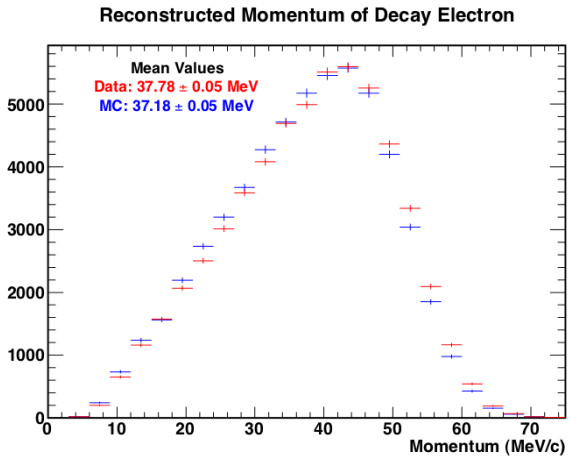

Figure 3.19: The data and MC energy distributions for stopping muon decay electron events.

3.5.2 Decay electrons

Decay electrons for stopping muons exist in large numbers in the SK data and are useful for checking the energy scale in the tens of MeV range. Fig. 3.19 shows the comparison between the measured energy spectrum and the Monte Carlo prediction for these events in units of MeV for SK-I data. The data and MC agree well, with the means differing by only about 2%. These data are also used to monitor the stability of the energy scale over time, showing stability within $\pm$ 1%. The SK-IV time variation of the mean is shown in Fig. 3.20.

3.5.3 Stopping muons

Particles emitting Cherenkov radiation have an opening radiation angle which is a known function of particle momentum. Estimating this opening angle allows one to calculate particle momentum independent of the PMT charge measurement and check for consistency. Stopping muons are used in this calibration. The opening angle function approaches a limiting value as the particle momentum increases, so only stopping muons with momentum less than 400 MeV/c are useful here. The ratio of the measured momentum to the momentum calculated via Cherenkov angle for MC and data are both taken, and the ratio of these ratios is calculated (a double ratio). This double ratio is plotted for SK-I in Fig. 3.23. As

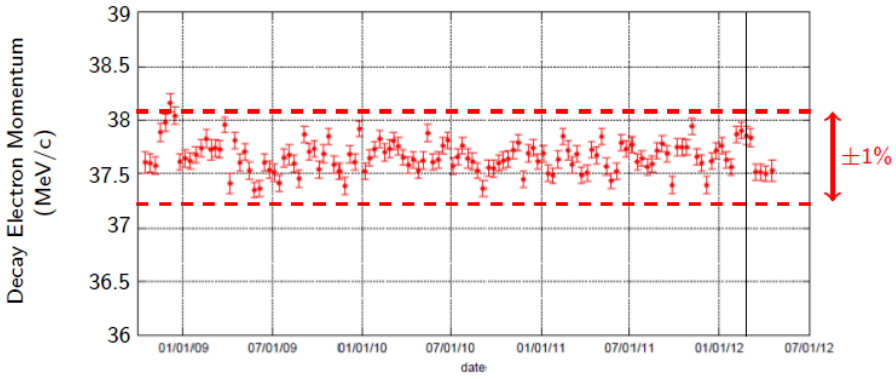

Figure 3.20: The time variation of the decay electron momentum mean from SK-IV data.

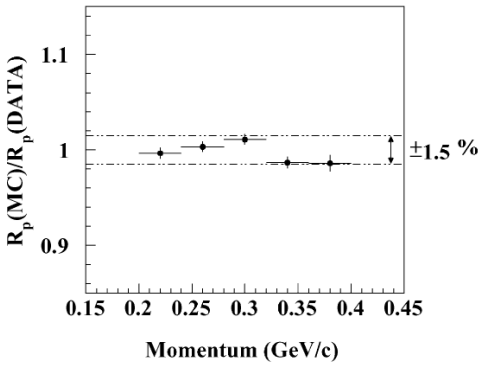

Figure 3.21: The ratio of MC to data of the ratio of measured momentum to inferred momentum from stopping muon opening angle.

seen in the figure the double ratio is consistent to within ± 1% for the momentum range between 0.2 and 0.4 GeV/c.

For higher energy stopping muons, the momentum loss is proportional to the track length, or range (this is because high energy muons lose energy at an approximately constant value per unit track length). The range is calculated by assuming the end point to be the location of the vertex of the decay electron event. The ratio of the momentum loss to the range as a function of range for a sample of stopping muons from an initial SK-I measurement is shown in Fig. 3.22. The data and MC have good general agreement, with

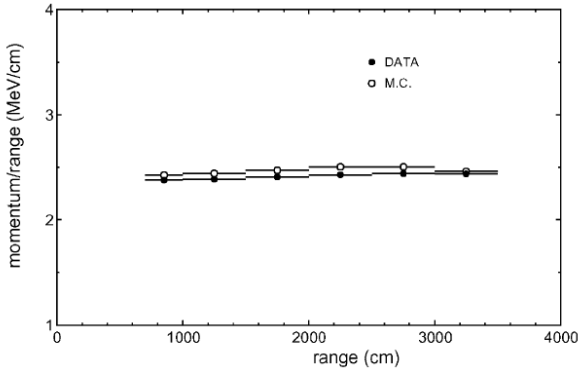

Figure 3.22: The ratio of momentum loss to range for stopping muons for both data and MC in initial SK-I calibration.

the ratio between the two staying almost constant over the measured values.

The SK-IV time variation of the momentum to range ratio is plotted in Fig. and is seen to be constant within ± 1%.

3.5.4 Neutral pions

Atmospheric neutrinos which interact in the detector via the neutral current often produce a single π^0 in the final state. These neutral pions are easily detected by looking for the signature of their decay to two gamma rays ($\sim$ 99% branching ratio.) These gamma rays create two showering (e-like) ring patterns. The invariant mass of 2-ring e-like events is reconstructed and the distribution is compared to the expected peak from π^0 decay. The resulting distributions of data and MC are shown in Fig. 3.24

Though the peak at 140 MeV/c is shifted relative to the value of the π^0 mass (135 MeV/c), the SK data and MC agree well with each other. The shift is caused by vertex reconstruction bias and other nuclear effects [12]. Most events in this sample have visible energy less than 1 GeV, because efficiency of cleanly detecting the two rings decreases with increasing π^0 energy from overlapping rings (decays with small opening angles) and asymmetric decays producing only one Cherenkov ring.

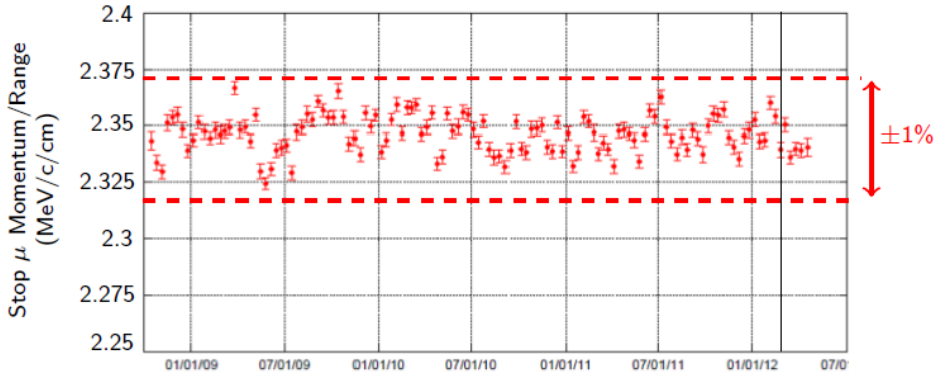

Figure 3.23: The time variation of the ratio of momentum to range for high-energy stopping muons for SK-IV.

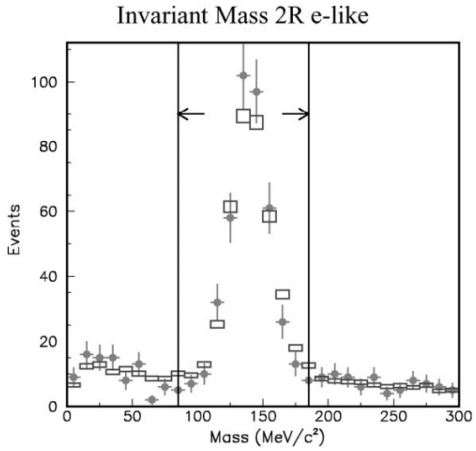

Figure 3.24: The invariant mass distribution of data and MC for 2-ring e-like events. Taken from Ref. [12].

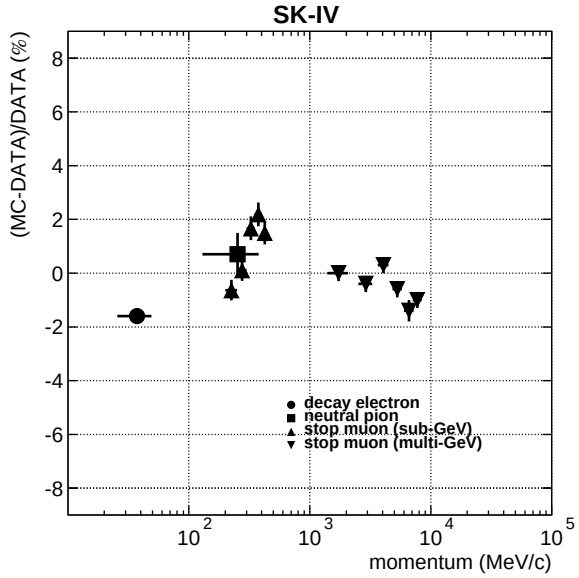

Figure 3.25: A summary plot showing the data and MC agreement for all energy scale calibration measurements as a function of energy.

3.5.5 Energy scale calibration summary

A summary of the agreement between data and MC for all of the above-mentioned energy scale calibrations in SK-IV is shown in Fig. 3.25. As shown in the figure the agreement between data and MC is within ± 2% across a wide range of energies including the energies of atmospheric neutrinos analyzed in this work.

3.6 OD calibration

The outer detector is mainly used as a veto for incoming cosmic ray muons and to identify the exit points of outgoing charged particles. Therefore, the timing and charge precision requirements are not as strict as in the ID. Calibration of the OD was most recently performed at the start of SK-IV upon installation of the new electronics, and that calibration is briefly described here. At the time of the SK-IV upgrade, OD PMT gains were lowered (200 V for new PMTs and 400 V for old PMTs) to reduce crosstalk with ID electronics. Light from the same N_2/Dye laser used in ID calibration is split and redirected to the OD

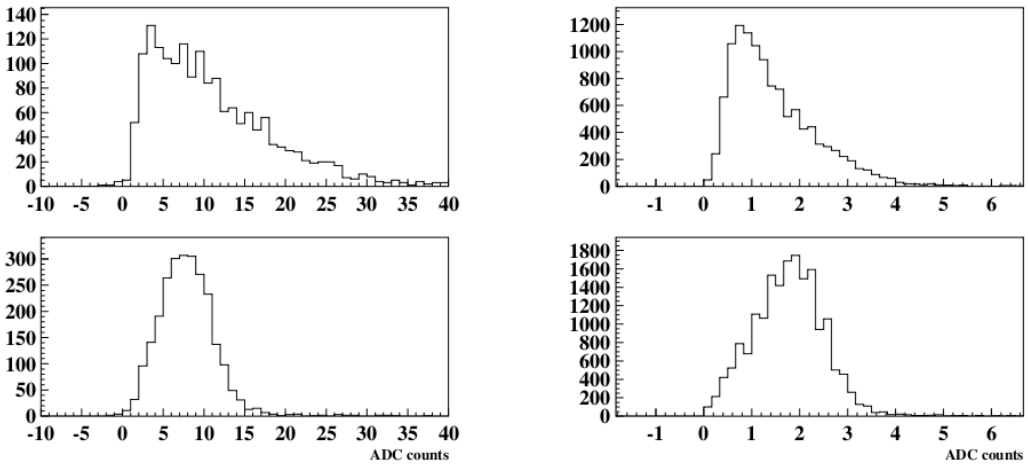

Figure 3.26: Example 1-p.e. distributions for old (top) and new (bottom) OD PMTs before (left) and after (right) SK-IV gain adjustment.

via optical fibers as one calibration light source. The fiber ends were mounted to various positions along the top, barrel, and bottom of the outer wall of the detector.

The single-p.e. distributions are in general different for old and new OD PMTs. Fig. 3.26 shows an example 1-p.e. distribution for an old (top) and new (bottom) PMT for both before (left side) and after (right side) the SK-IV gain adjustment.

The OD PMT gain measurement was performed by both the laser light and dark rate measurements. The laser light was flashed at low light levels to determine charge per p.e. for each PMT. The mean number of output ADC counts from this measurement was used as the single p.e. level. In addition to this the dark rate noise hits outside the trigger window, which have a high probability of being sinle p.e. hits, were also used to measure the same ADC count value after pedestal subtraction. The ADC measurements from this were found to agree to the laser measurements to within 10%, so this method was primarily used. For SK-IV, typical counts-per-p.e. ranged from 2-6 for OD PMTs.

The measured charge as a function of input charge for a wider charge range was also measured with the laser. The curve from this measurement is shown in Fig. 3.27. A saturation effect is seen at high p.e. levels (hundred's of p.e.s upward) and this effect is also

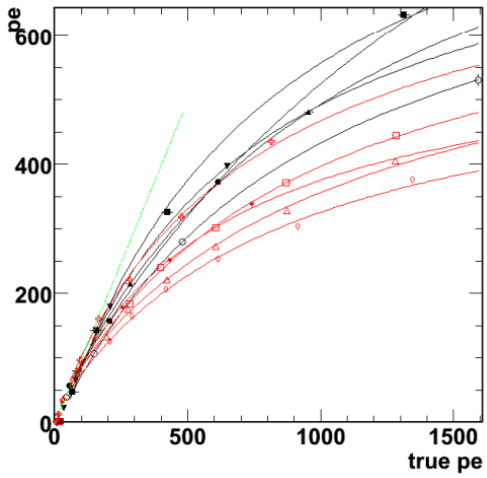

Figure 3.27: Measured versus input charge for old (red) and new (black) OD PMTs from laser measurements.

modeled in the MC simulation code.

The goal of the OD timing check was to confirm that the timing offsets relative to the ID PMTs and to the other OD PMTs was not too large ($\leq$ few ns). The cable length for each PMT, ranging from 70 to 78 m, was taken into account for this study. The offsets were determined by flashing the laser in both the ID and OD with identical cable and diffuser ball, and this confirmed that the offset was sufficiently small. Cosmic ray muons were also used to check the agreement by comparing the timing difference for each pair of ID and OD PMTs that was closest to the muon track at any given point along the track.

Finally, a new calibration study was introduced in SK-IV to check the relative efficiencies of the old and new OD PMTs. A laser diode and diffuser ball was inserted into the barrel portion of the OD and flashed at 100 Hz at various heights. Old and new PMTs were grouped into pairs with each other such that the distance and relative position (above or below) for each PMT in the pair was identical (though not necessarily from the same diffuser ball height). With these conditions 15 pairs of PMTs were chosen. For each PMT and each run the occupancy, defined as

Figure 3.28: A photograph of the NIM modules used in the SN Burst test which the author of this work arranged to simulate a SN signal.

$$\text{occupancy} = \frac{N_{hits}^{ontime} - N_{hits}^{offtime}}{N_{triggers}} \tag{3.11}$$

was measured and then the ratio taken of old and new PMTs for comparison. The average of the ratio for all 15 pairs was used as the tuning input parameter for the detector simulation, which is described in more detail in the following chapter.

3.7 Supernova burst test

With the installation of the new SK-IV front-end electronics the SK detector's ability to process high-rate data from nearby supernova events was improved. A new Supernova Burst test system was constructed and tested prior to SK-IV QBEE installation. The system consisted of NIM logic modules arranged to simulate a supernova burst signal. This was done by using a NIM pulse generator in combination with gate and delay modules to generate sequences with as many as $\sim$ 28 million pulses over a 10-second time window whose time profile simulated that of neutrino events in SK from a galactic supernova. A picture of the NIM module setup is shown in Fig.3.28.

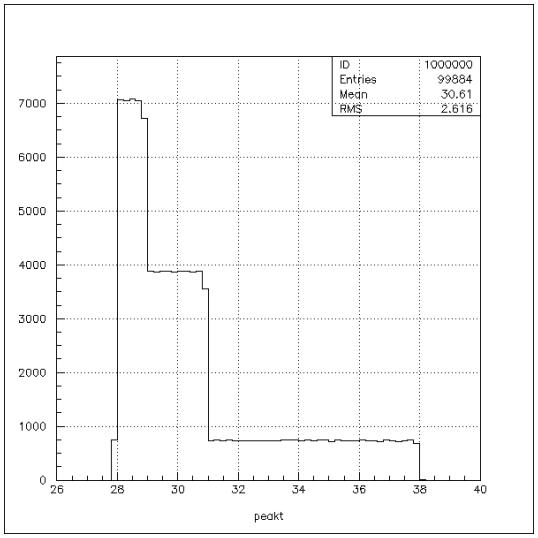

Figure 3.29: A sample of the triggering profile during the SN Burst test taken during SK-IV test installation.

These pulses were fed into an LED light system whose 375 nm output was directed into the SK tank from above via an optical fiber. A diffuser ball was attached to the end of the optical fiber to spread the light throught the tank. An example of the triggering pattern that occurred in the detector is shown in the time profile in Fig. 3.29. This profile closely mimics the expected supernova neutrino curve. The tesitng system was first installed during the SK-IV test installation in summer of 2008 and has been in place throughout the duration of SK-IV.

Chapter 4

ATMOSPHERIC NEUTRINO MONTE CARLO

Experimental particle physics analyses generally proceed by comparing final data samples to predictions from Monte Carlo which simulates the models being analyzed as well as the response of the detector to the interactions under study. Atmospheric neutrino oscillation studies at SK use this same procedure, and the goal of this chapter is to describe in detail the Monte Carlo samples produced for these studies. The three main pieces of the Monte Carlo which will be described are the atmospheric neutrino flux, the neutrino interactions, and the detector response. Monte Carlo sample are generated for each unique detector phase (SK-I, SK-II, SK-III and SK-IV). The analyses in this work feature updated MC samples for the first three SK running periods, as well as SK-IV samples which are used for the first time in physics analyses.

4.1 Atmospheric neutrino flux

The Monte Carlo begins with a simulation of the atmospheric neutrino flux starting with primary cosmic rays. At low energies ($\lesssim$ 1 GeV) the primary flux is well-known, but the earth's magnetic field and solar activity have large effects on cosmic rays in this region. The Earth's magnetic field creates a rigidity (momentum/charge) cutoff for incoming charged particles. Additionally, the solar wind reduces cosmic ray flux via its magnetic field. Periods of peak solar activity create flux reductions by as large as a factor of two. At energies $\sim$ 10 GeV and upwards, the flux becomes less well-known, but the influence of geomagnetic and solar effects diminishes. The accuracy of cosmic ray flux measurements below 100 GeV primary energy is about 5% and gets worse with increasing energy value[65]. The flux model used for the numbers and figures in this work is the Honda 2011 model[49], which is an update to the model used in previous SK analyses [48, 47]. The monte carlo events were initially generated with the Honda 2006 flux[48] (at the time of production the most

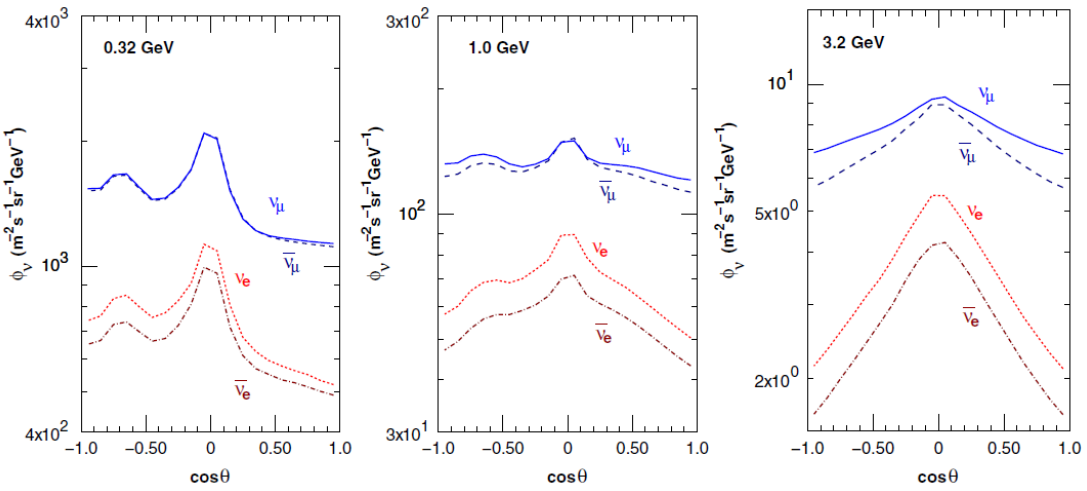

Figure 4.1: The zenith angle dependence of the Honda 2011 flux for atmospheric neutrino flux at Kamioka averaged over azimuthal angle, taken from [49].

recent available model) and then reweighted afterwards to match the Honda 2011 model. The solar wind and geomagnetic effects are accounted for in the flux calculations. The local magnetic field strength near Kamioka is larger than the global average, resulting in a slight up-down asymmetry in the neutrino flux.

The Honda flux assumes the primary cosmic rays are dominantly H nuclei with small contributions from He and other nuclei. The subsequent hadronic interactions are modeled to produce an atmospheric muon flux. A combination of two hadronic interaction models is used in the updated 2011 model. At low energies (atmospheric muon Energy $<$ 32 GeV/c) a modified version of the JAM model[40], found to have good agreement with atmospheric muon flux data, is used for the first time. A modified DMPJET-III model[103], used in the previous versions of this calculation, is used for primaries that produce atmospheric muons above 32 GeV/c. The main difference as a result of the new low-energy model is a small increase in the atmospheric muon flux below 1 GeV/c. The model is three-dimensional, meaning that the secondary particles are not confined to travel in the same direction as their parent particle. The zenith-angle dependent aziumuth-averaged neutrino flux for three different energies is shown in Fig. 4.1.

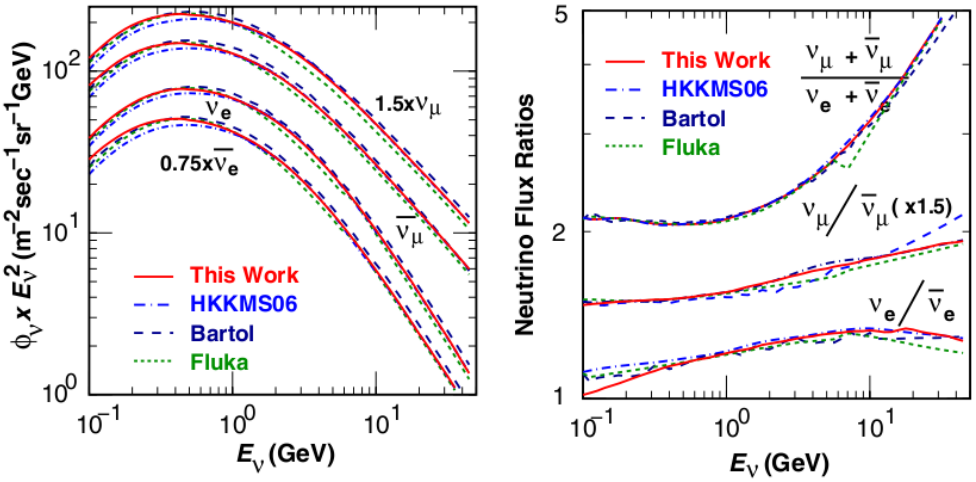

Figure 4.2: The energy dependence of flux for each neutrino type (left) and important flux ratios (right). HHKMS06 is the Honda 2006 flux[48], and Bartol[3] and Fluka[4] are existing alternative flux calculations. Taken from [49].

The zenith-angle dependence shows a peak in the near-horizontal direction. Secondary particles travel a longer distance in the atmosphere when coming from these directions and therefore have a greater probability to decay and produce a neutrino than those from other zenith angles. The deflection of low energy secondary particles by the geomagnetic field enhances the peak at lower energies. There is an additional geometric enhancement from the 3D nature of the simulation (relative to previous 1D models) because the effective area from which a neutrino can be produced is larger near the horizon when the neutrino is not constrained to the same dimension as the parent cosmic ray. The resulting calculated neutrino flux as a function of energy is shown for each neutrino type in the LHS of Fig. 4.2. The ratios of μ-type to e-type and ν to $\bar{\nu}$ are shown on the RHS of the figure. Overall there are more neutrinos than anti-neutrinos expected in the flux and the ratio $\frac{\nu_\mu+\bar{\nu_\mu}}{\nu_e+\bar{\nu_e}}$ is approximately two at low energies and increases at higher energies.

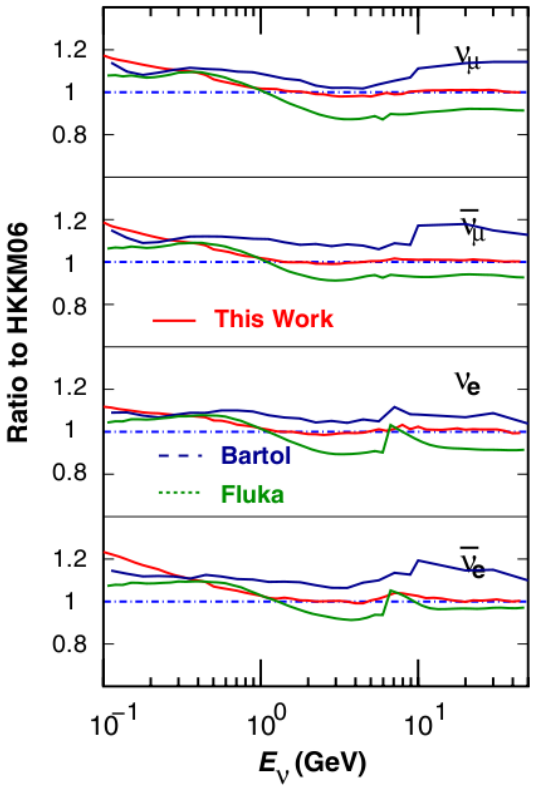

Figure 4.3: The ratios of the direction-averaged flux for Kamioka in the Honda 2011("This model"), Bartol[3] and Fluka[4] models relative to the Honda 2006 flux[48], Taken from [49].

4.2 Neutrino interaction simulation

Neutrino interactions on nucleons and nuclei are simulated by the NEUT program[82, 83], a custom program for SK written in Fortran. Interactions of neutrinos on protons, neutrons, oxygen and other nuclei are modeled and interactions can take place in the detector water or in the rock surrounding the tank. Interactions within the detector are assumed to occur on the nucleons and nuclei of water molecules, while those in the rock surrounding the detector assume silicon dioxide (SiO_2). NEUT covers a wide range of energies spanning from several tens of MeV up to hundreds of TeV. Charged and neutral current interactions of the following modes are included in the program:

$$\begin{aligned}
\text{CC/NC quasi-elastic: } & \nu N \rightarrow l N^{'} \\
\text{CC/NC single-}\pi\text{ production: } & \nu N \rightarrow l N^{'} \pi \\
\text{CC/NC single-}\gamma\text{ production: } & \nu N \rightarrow l N^{'} \gamma \\
\text{CC/NC single-K production: } & \nu N \rightarrow l \Lambda K \\
\text{CC/NC single-}\eta\text{ production: } & \nu N \rightarrow l N^{'} \eta \\
\text{CC/NC deep inelastic scattering: } & \nu N \rightarrow l N^{'} \text{hadrons} \\
\text{CC/NC coherent-}\pi\text{ production: } & \nu^{16} O \rightarrow l \pi X
\end{aligned}$$

where N and $N^{'}$ are differing nucleons (protons or neutrons), l is a lepton and X is the post-interaction nucleus. NEUT provides the cross-sections of the interactions listed above and selects an interaction mode for each event. Interactions of neutrinos on electrons are ignored because their cross-sections are smaller than nucleon cross-sections by a few about 10^3 at energies around 1 GeV. NEUT also simulates meson interactions in the target (nucleus) as well as nucleon re-scattering.

4.2.1 Elastic and Quasi-elastic Scattering

For quasi-elastic scattering NEUT considers both free and bound nuclei. Quasi-elastic scattering on a free nucleon is simulated by the model of Llewellyn-Smith[106]. For bound

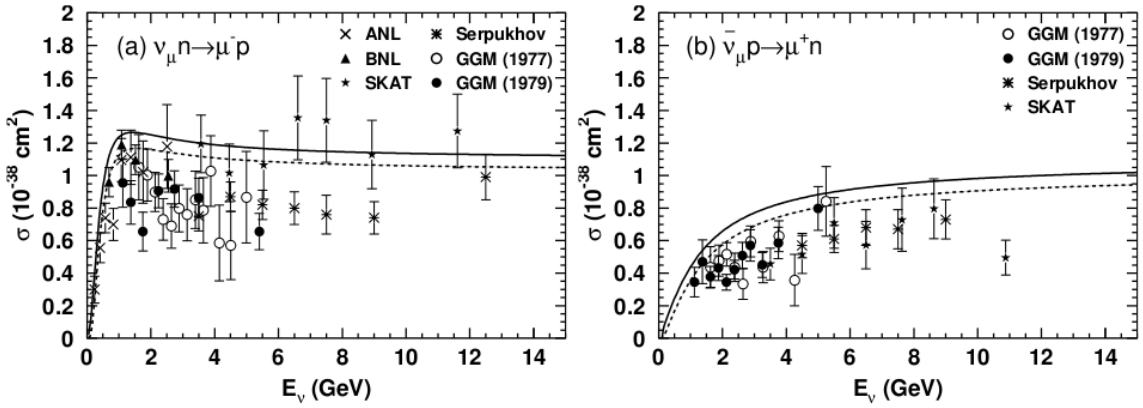

Figure 4.4: The ν_μ and $\bar{\nu_\mu}$ CCQE cross-sections for NEUT (line) and various experimental measurements. See [83] for details.

nucleons in a nucleus the model of Smith and Moniz[107] is used. The latter is a relativistic Fermi gas model which assumes a flat momentum distribution with a Fermi surface (which follows from the Pauli exclusion principle, allowing only one fermion per quantum state) of $p_F = 225$ MeV/c. The axial-vector form factor (the component of the weak interaction current in which the non-conservation of parity is manifested) is assumed to be a dipole and the axial-vector mass, M_A, is set to a value of 1.21 GeV/c, which is in agreement with recent experimental results[45, 24]. The predicted charged-current quasi-elastic (CCQE) cross-sections from NEUT as well as experimental measurements for ν_μ and $\bar{\nu_\mu}$ are shown in Fig. 4.4.

The calculation of neutral current quasi-elastic cross-sections was recently updated within NEUT. The NCQE interaction between a neutrino and oxygen can produce γ-ray decays with energies of a few to 20 MeV. These gamma rays can be a serious background for supernova relic neutrino (SRN) detection, so estimating the interaction's cross-section accurately can improve background estimates. Previously, NCQE cross sections were roughly estimated as ratios of known CCQE cross-sections. After the update, the correct form factors for these interactions were used to directly calculate the cross-sections. An additional nuclear medium correction, the spectral function, for $\nu - ^{16}$O interactions was included. This

function calculates the probability of removing a nucleon from a nucleus, given a nucleon momentum of p and a residual nucleus state of energy E, and is used in calculating the differential cross-section. After this addition the $\nu + p$ cross-sections were nearly identical, but the new ν + n cross-sections differed by $\sim$ 20 - 40 percent as a function of energy, so this update was limited to only oxygen cross-sections.

4.2.2 Meson and Photon Production

Production of mesons such as the π, K and η (hadronic particles each made of a quark and anti-quark) is simulated by the Rein and Sehgal model[101]. The model assumes an interaction via a nuclear resonance of the form

$$\nu + N \rightarrow l + N^*$$
$$N^* \rightarrow m + N^{'}$$

where N^* is the baryonic resonance and m is a meson such as a pion. The Rein and Sehgal model provides the probabilities for resonance production. NEUT then multiplies that number by the probability for each resonance to decay to one meson (π, K, η) or γ, and one nucleon to calculate the cross-section for their respective productions. In these calculations a total of 18 resonances below 2 GeV/c^2 are considered. As in quasi-elastic scattering, the axial-mass is set to 1.2 GeV/c^2. For pion production, the angular pion distribution was calculated as in the Rein and Sehgal model for the $\Delta(1232)$ resonance, and was assumed to be isotropic for the other resonances. NEUT's predicted π^+ angular distribution agrees well with the measured experimental results for $\nu + p \rightarrow \mu^- + p + \pi$ from The Pauli blocking effect is also included. This effect is based on the Pauli exclusion principle and suppresses cross-sections by a few percent by forbidding scattering states which produce fermions of momentum less than the Fermi momentum. Delta decays which produce a lepton and nucleon but no pions are also included and this accounts for $\sim$ 20% of all decays.

Coherent pion production is a special subset of meson production which is also included in NEUT. In this process the nucleus is left in an unchanged state after an interaction which produces a single pion ($\pi^{\pm}$ in CC and neutral π in NC). The cross-section is calculated analytically and relies on pion-nucleon cross-sections taken from Rein and Sehgal's model[101].

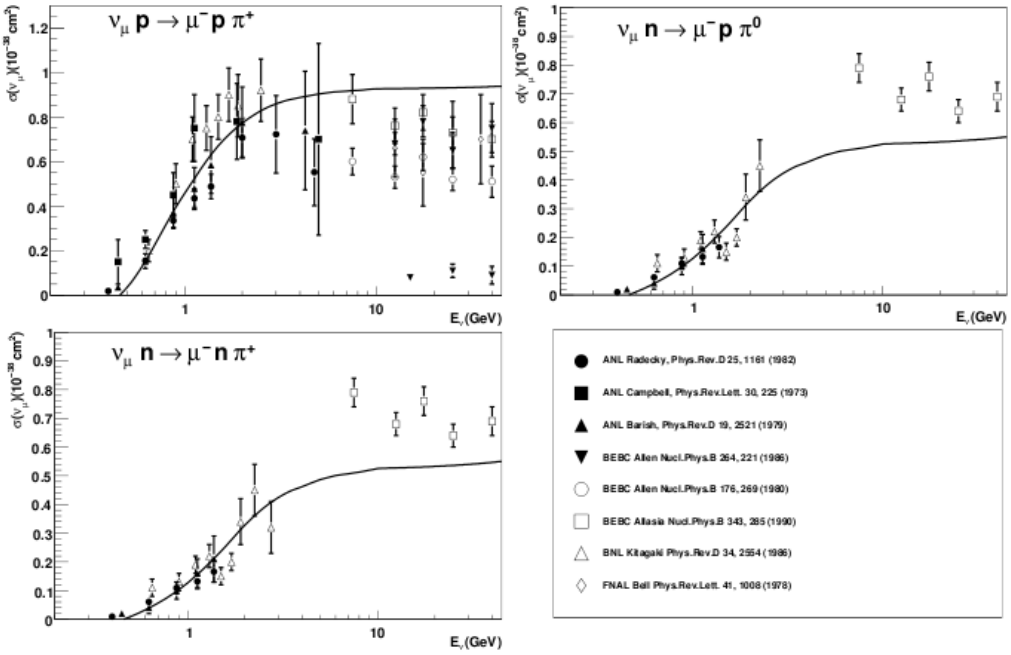

Figure 4.5: The cross-sections for CC single-π production for (a) $\nu_\mu p \rightarrow \mu^- p\pi^+$, (b) $\nu_\mu n \rightarrow \mu^- p\pi^0$ and (c) $\nu_\mu n \rightarrow \mu^- n\pi^+$. The solid line shows the NEUT calculation and the dots show the data points summarized in the bottom right. Taken from [83].

The NC process is especially important for backgrounds in accelerator beamline experiments searching for ν_e appearance candidates because the π^0 decay γ's can mimic e-like rings in the ν_e signal energy region.

4.2.3 Deep Inelastic Scattering

Deep inelastic scattering (DIS) becomes the most dominant interaction neutrino cross-section at higher energies. This is the interaction which was used to probe the inside of nucleons and helped establish the first evidence of quark structure. In DIS interactions the target nucleon is not kept in tact and there are many hadronic particles in the final state, so the invariant mass of the hadronic system is larger than that of the original nucleon. NEUT directly calculates the CC DIS cross-section by integrating the differential cross-section above hadronic invariant masses of 1.3 GeV/c^2. The parton distribution functions, which describe the momentum distributions of quarks inside the proton, are taken from GRV98 [78] with corrections from Bodek and Yang [6]. A pion multiplicity function is used to describe multiple pion production. Single pion production was handled as described in the previous section to avoid double counting. This function took the form $n_\pi = 0.09 + 1.83 \ln W^2$, where n_π is the mean number of pions produced and W is the hadronic system invariant mass. The NC multiple pion production rates were treated simply by multiplying CC interaction rates by coefficients, whose value was different depending on energy region[83]. Hadronic final states are simulated by a combination of custom NEUT code[50] used up to masses of 2.0 GeV/c^2, and Pythia/JETSET[105] for higher energy interactions.

4.2.4 Nuclear Effects

The particles which are generated in the primary neutrino interaction can undergo interactions in the nucleus before escaping. Therefore, the particles eventually observed by the detector outside the nucleus may not be the same as those initially generated by the interaction. The nuclear effects are therefore very important and NEUT simulates these effects for pions, kaons, etas and nucleons. These final state interactions (FSI) for pions were recently updated. Pions in particular are important because the cross-sections of pion production

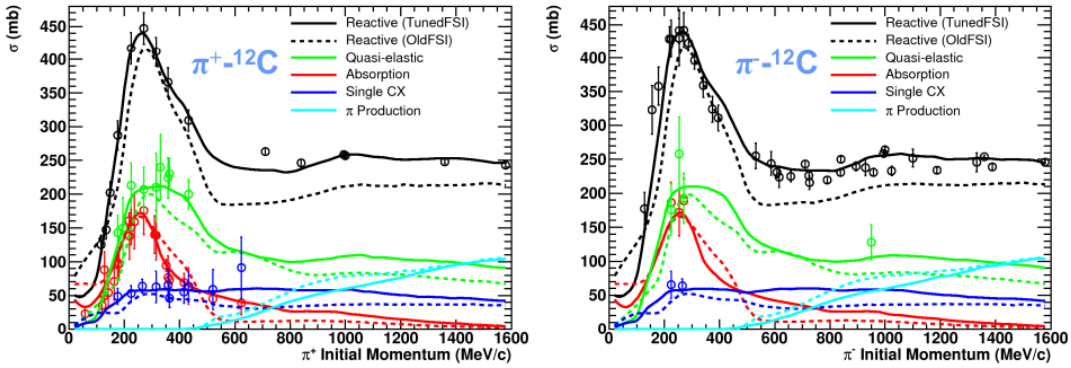

Figure 4.6: The cross-sections from old and new pion interaction models in NEUT compared to data as a function of pion momentum.

in neutrino interactions and subsequent pion-nucleon interactions are relatively large. The propagation of the π through the nucleus is done by stepping it through the nucleus and calculating the probability of interaction at each point using the mean free path (MFP) information. The interactions of pions within the nucleus that occur with high probabilities include charge exchange ($\pi^{\pm} \rightarrow \pi^{0}$), quasi-elastic scattering (affects kinematics), and absorption (loss of a pion, typically produces nucleons).

For low energy pions, $p_{\pi} < 500$ MeV/c, the interaction probability per step is calculated by the model of Salcedo and Oset[104]. Their model includes Fermi motion in the nucleus and Pauli blocking effects, as well as a density-dependent Fermi surface momentum. As a result the pion interaction probabilities depend on the momentum as well as the position within the nucleus. The LE probability table was recently tuned to achieve better agreement with $\pi^{+} + C$ scattering data. This was done by altering the momentum dependence of the interaction probability per step.

The scattering kinematics are determined by a phase-shift analysis of free nucleon scattering data[30, 58] which was unchanged from previous analyses. For $p_{\pi} > 500$ MeV/c, the nucleons are assumed to be quasifree particles. The $\pi^{\pm}$P cross-sections are used directly to calculate interaction probabilities. As part of the recent updates, the elastic and charge-exchange cross-sections, σ_{el} and σ_{CX} were scaled by a factor of 1.8, motivated by the most

recent high energy π^+-C data. The scattering kinematic calculations were also changed to use the same phase-shift method as the low energy scattering. In the case of pion absorption, NEUT previously did not generate any additional particles. This was updated so that now ejection of protons and neutrons after such pion interactions (absorption and also scattering) is modeled. This is important for vertex activity studies in neutrino interactions in current and future detectors. This implementation referenced both π-nucleus absorption data [26] and π-d data[102] for consistency.

4.3 Detector Simulation

After the neutrino interactions modeled by NEUT, the outgoing particles are fed into a simulation which tracks them in the detector. This detector simulation is responsible for tracking the charged particles path in water, their cherenkov radiation, any secondary interactions they may undergo, reflection from Tyvek in the detector scaffolding and finally the PMT and electronics responses. The detector simulation is a customized program called "skdetsim" based on CERN's GEANT package[7] (in particular, GEANT3). The simulation includes many physics effects within the tracking. Photons can undergo pair production and compton scattering. The photo-electric effect at the photocathode surface is also modeled. All charged particles ($e^{\pm}, \mu^{\pm}$, Hadrons) can emit Cherenkov radiation, undergo multiple scattering, ionzation, Bremsstrahlung, as well as in decay in flight (μ and Hadrons), among other processes (see [88] for more details).

The photon propagation in the simulation models the Cherenkov radation with a wavelength-dependent group velocity. The calibration procedures described in the previous chapter determine the parameters which go into the effective index of refraction, which is used to calculate the velocity. Photons can be absorbed or scattered by water molecules and their intensity is assumed to decrease according to equation 3.1. As mentioned in the Calibration chapter, both Mie and Rayleigh scattering are considered and are tuned for agreement with the calibration data. The reflection and absorption of photons on the detector materials such as PMTs and black scaffolding sheets are calculated from probability functions of the photon incident angle that are estimated from direct calibration measurements. The PMT response is modeled by assuming the measured quantum efficiency for each tube. The to-

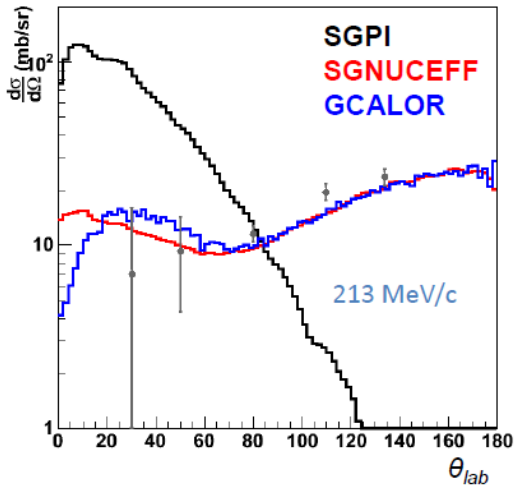

Figure 4.7: The QE differential cross-section for pion scattering on a thin-water target. The new SGNUCEFF model agrees with scattering data much better than the previous SGPI model.

tal charged detected by each PMT is taken to be the summation of all p.e.s weighted by the single-p.e. distribution. The hit timing is also smeared by the measured PMT timing resolution. The simulation also accounts for the reduced number of PMTs in the SK-II run period.

The hadronic interaction model for pions in water was recently updated in SKDetsim to improve agreement with recent data. Pion interactions are modeled by two separate codes depending on the pion momentum. In both cases the pion hadronic interaction length is determined by the total cross-section given by

$$\sigma_{\mathrm{T}} = \sigma_{\mathrm{Oxygen}} + 2\sigma_{\mathrm{H}}. \tag{4.1}$$

The GCALOR package[113] is used for modeling high-energy interactions ($p_\pi gt$ 500 MeV/c) and shows good agreement with the data. For low-energy pions ($p_\pi \leq 500$ MeV/c) custom codes[50] are used and these have been recently updated. The previous code[50] called SGPI relied on older data which was tuned to ^{27}Al pion scattering. The new model, called SGNUCEFF, uses an improved measurement of Eq. 4.1 tuned to ^{16}O data with

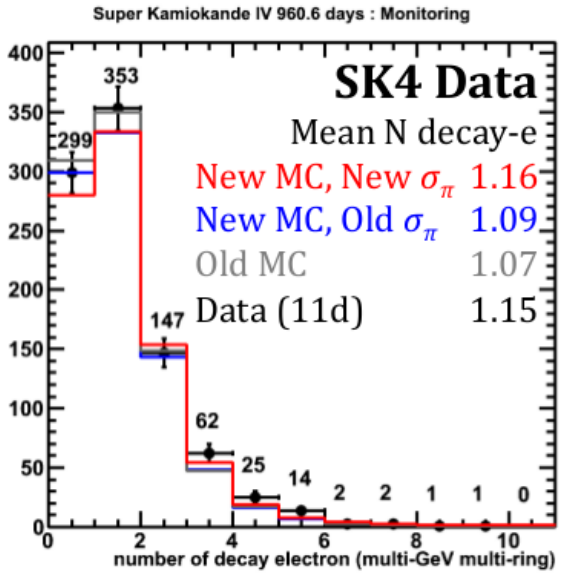

Figure 4.8: Number of decay-electrons for a selected SK-4 event sample. The black is data, the gray the MC used in previous SK analyses, and the blue and red histograms are the predictions from the new MC with old and new pion interaction cross-sections, respectively.

the interaction channels determined by the NEUT cascade model. The ^{1}H cross-sections are modeled as fractions of scattering cross-sections on H_2O. The improvements to the QE differential cross-section of pion scattering (p_π = 213 MeV/c) from a thin-target water simulation are shown in Fig. 4.7. The SPNUCEFF model shows good agreement with data at low pion momentum, unlike the previous SGPI model which showed a forward-peak bias. These updated pion interactions were included in the monte carlo detector simulation used in the analyses described in this work. These changes in general decreased the pion interaction cross-sections, leading to more pion decays producing decay-e, an example of which is shown in Fig. 4.8 (the data sample shown in this plot is explained in the following chapter). As seen in the plot the mean number of decay electrons predicted in the monte carlo (red histogram) is increased by the updated pion cross-sections relative to the old MC (gray histogram).

4.3.1 OD Tuning

As part of the detector simulation process there are a set of parameters specific to the OD which its response and are specific to each phase of the detector. These parameters describe the PMT response (dark rate, collection efficiency, single-p.e. response, wavelength-shifting plate characteristics) as well as the PMT support structure materials (reflectivity/transmission rate of the Tyvek sheets) independently for the top, barrel and bottom portions of the detector. The tuning method was updated recently during the SK-IV run period. Brief descriptions of the original methods and the SK-IV improvements are described here. A more detailed description of the previous method can be found in [111].

Originally the tuning was done manually by looking at distributions of all relevant variables until sufficient achievement is found. This was done for detector phases SK-I, SK-II, SK-III, and initially in SK-IV. Cosmic-ray muon samples were used as the data for tuning. Through-going muons which enter from the top and stopping muons which enter from the side were chosen for the sample. MC muons with the same directions and energies as the reconstructed muons from the data are generated and the detector response between the two is compared and tuned until agreement is satisfactory. The light reflection model of the Tyvek includes both Gaussian and Lambertian (isotropic diffuse reflection) components. The fraction of each component is based on the measurements of [8].

The single-p.e. response is measured by taking hits in the muon data sample which occur before the event itself because these dark noise mostly represent one photoelectron. A PMT response function made from the combination of a plateau response at low charge and exponential response at higher charges was constructed for each detector phase. PMT responses in the simulation randomly sampled this distribution. PMT saturation is relevant for hit PMTs close to the entrance or exit points of energetic muons and two parameters in the tuning account for this.

Recently the tuning process has undergone an upgrade which introduces some automation. In SK-IV, the simulated charge in the OD top was determined to be too low relative to the data samples after initial tuning. This is because the cosmic-ray muons samples mentioned above do not provide a good sample for tuning the top of the OD. To improve

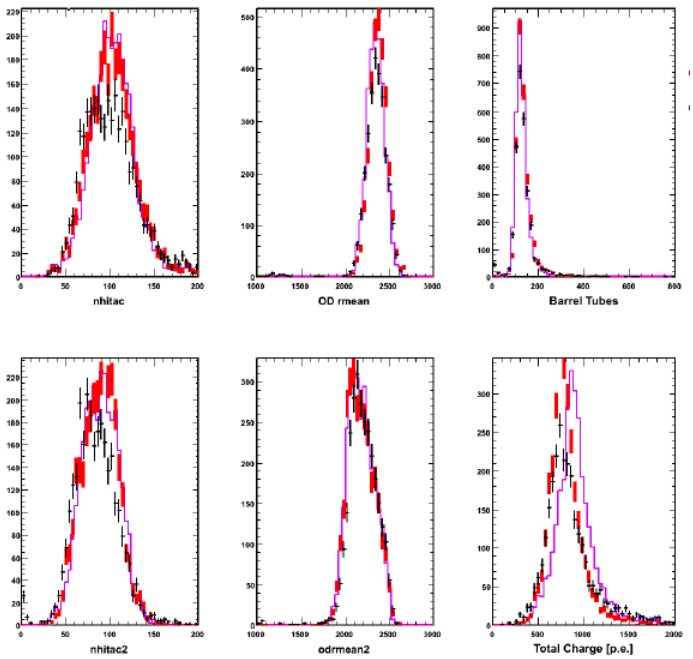

Figure 4.9: Distributions of SK-IV OD variables for cosmic ray data (black), MC with old tuning (purple) and MC with the most recent tuning (red).

this, a monochromatic MC sample of muons which exit the top of the detector was generated and added to the set of data histograms used in the tuning. Additionally, the process was partially automated by defining a grid for all the OD tuning parameters and generating distributions (comparing updated data to MC samples) on all points of this grid. A Kolmogorov-Smirnov test is performed for each set of generated distributions and the tuning parameters which provide the best result from this test are chosen. The distributions used in this tuning included nhitac (number of hits in the OD cluster with the most charge), nhitac2 (number of hits in the second-largest OD charge cluster), Odrmean (average distance among all pairs of OD hits), total OD charge and top OD charge. The resulting distributions of the tuned MC for the original and updated SK-IV tunings are shown in Fig. 4.9. In general the agreement is improved by the new tuning.

The old (from IMB) and new (made for SK) OD PMTs have different relative efficiencies which were also included in the tuning. The new calibration study described in the previous chapter was performed and the average relative efficiency for old versus new tubes was measured to be 0.96 ± 0.03.

Chapter 5

ATMOSPHERIC NEUTRINO DATA REDUCTION

The SK data stream processes about 10^6 trigger events per day. The large majority are background events, such as cosmic ray muons, gamma rays from radioactive atoms such as Radon, and PMT internal discharges triggering a flasher event. These are filtered out by the reduction process, thus producing the SK data set requires a thorough and efficient sequence of reduction steps. There are three main reduction chains categorized broadly by event geometries: Fully Contained (FC), Partially Contained (PC) and Upward-Going Muons (UPMU), listed in order of increasing average energy. For atmospheric neutrino analyses only events with a visible energy above 30 MeV are passed on to reduction.

The first two categories, FC and PC, comprise events with an interaction vertex located within the fiducial volume of the ID, which is defined to be greater than 2m away from the IDs surface. FC events deposit all of their lepton's Cherenkov energy in the ID (in other words, the Cherenkov radiation emission track does not make it out of the ID. PC events have higher energies on average and are characterized by the charged lepton exiting the detector and creating an exit point cluster in the OD in the process. PC events are assumed to be from muons because electrons generally do not travel far enough to exit the detector.

The UPMU sample is made up of high-energy muon events which have an interaction vertex in the rock beneath and surrounding the detector. Only upward-going muon events are chosen because neutrino-induced muons cannot be isolated from the high rate of downward-going cosmic ray muons penetrating the detector. These are further separated into two categories, stopping and through-going, based on whether or not the reconstructed muon track exits the detector. Schematics of the main event categories are shown in Fig. 5.1. Each of these three broad event categories contains more detailed event sub-categories whose characteristics will be described in the following sections. All data samples are di-

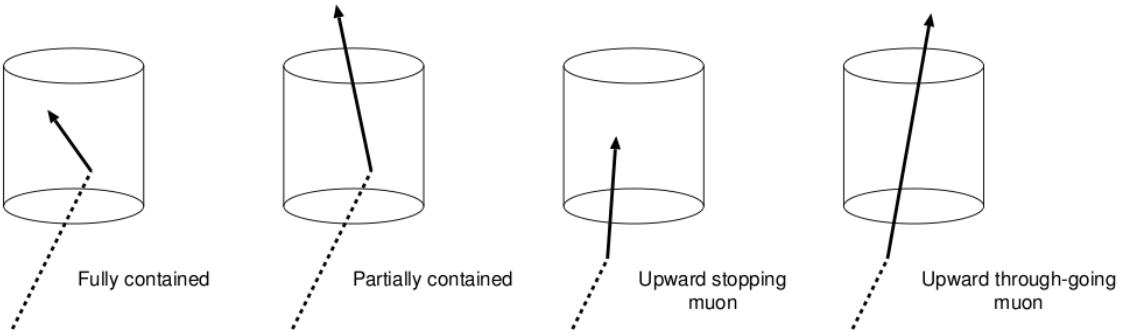

Figure 5.1: Typical neutrino (dashed) and resulting charged lepton (solid) tracks for the fully contained (FC), partially contained (PC), upward-going stopping (Up-Stop) and upward through-going (Up-thru) event types, shown left to right.

vided by the four detector phases: SK-I (1996-2001), SK-II (2002-2005), SK-III (2006-2008), and SK-IV (2008-present). The analyses in this work uses SK-IV data for the first time.

The SK data is divided into run files which are limited to 24 hours at most. Runs can be less than 24 hours especially in cases where calibration or other detector maintenance is taking place. A typical 24-hour run corresponds to about 150 GB of data, the bulk of which is just low energy background events. Each run is divided into many subruns which are each stopped at either ten minutes of data or ten MB of data (whichever limit is reached first). Each of the three reduction streams described here have become automated within the past few years so that the most recent data is run through the reduction daily.

5.1 Fully Contained Reduction

FC events are first separated from PC events by requiring the number of hits in the largest OD cluster to be fewer than 10. The following are the five main steps in the reduction process:

5.1.1 First Reduction

An event passes the first reduction step if it satisfies the following criteria:

1. $\mathrm{PE}_{total} > 200$ p.e.s (100 p.e.s for SK-II), where P.E. is the total ID charge collected

in a 300 nsec time window.

2. $\text{NHITA}_{800} \leq 50$ where NHITA is the number of OD hits in an 800 nsec window surrounding the trigger timing.

The first criterion eliminates low-energy background events from radioactivity. A 200-p.e. event corresponds to an electron momentum of 22 MeV/c. Because the analysis event energy threshold is 30 MeV, this cut does not eliminate analysis-worthy events. The second cut removes cosmic ray muons, which deposit energy in the OD as they enter the detector. The output rate for the FC1 reduction is 1500 events/day on average.

5.1.2 Second Reduction

1. $\text{NHITA}_{800} \leq 25$ for events with $\text{PE}_{total} < 100,000$ p.e.s (50,000 p.e.s for SK-II)
2. $\text{PE}_{max}/\text{PE}_{300} < 0.5$, where PE_{max} is the maximum number of p.e.s observed by a single PMT within the event and PE_{300} is the total number of p.e.s observed in the ID in a 300 nsec sliding time window

The first criterion performs a stricter cut on cosmic ray muon events. The second criterion helps remove events caused by electronics noise, which tend to have a single PMT discharge with a signal much larger than an average PMT signal and make up the majority of charge for an event. After FC2 reduction there are about 200 events/day remaining.

5.1.3 Third Reduction

The FC3 reduction cuts reduce the event rate to about 30 events/day. The majority of remaining backgrounds which are put into the third reduction are low-energy radioactivity events and cosmic ray muons which do not produce much OD activity. The following are specific categories of background which are removed by targeted reduction cuts.

Through-going muons

Through-going muons deposit large amounts of energy in the ID and if their OD activity is minimal they survive the first two reduction cuts. For events with at least 1000 ID PMTs

each detecting more than 230 p.e.s a special through-going muon fitter is applied. With the assumption that such a muon caused the ID light pattern, the fitter sets the entrance point to be the earliest hit PMT among the entrance cluster. The exit point is defined to be the center of all PMTs which are saturated around the muon's exit location. A goodness-of-fit parameter is constructed by the function

$$\text{goodness} = \frac{1}{\Sigma_i \frac{1}{\sigma_i^2}} \times \sum_i \frac{1}{\sigma_i^2} exp\left(-\frac{(t_i - T_i)^2}{2(1.5 \times \sigma_i^2)}\right) \tag{5.1}$$

where i is the PMT index, t_i and σ_i are the i-th PMTs observed hit timing and timing resolution, and T_i is the estimated hit timing based on the muon's assumed entering point and track. After this is calculated, the cut criteria are defined as

1. goodness > 0.75
2. NHITA$_{in} \geq 10$ or NHITA$_{out} \geq 10$

where *in* (*out*) represents the number of hit OD PMTs located within 8 m of the assumed entrance (exit) point within an 800 nsec time window. Events which pass these cuts are rejected as through-going muons.

Stopping Muon Cut

Cosmic ray muons which stop in the detector are also eliminated in a similar manner. The fitter estimates the entrance point via the same method as through-going events, and relies on the same goodness of fit as in Eq. 5.1. All events which have NHITA$_{in} \geq 10$ OR events with NHITA$_{in} \geq 5$ and goodness > 0.5 are rejected in this cut. The muon direction is reconstructed so that the number of p.e.s within the cone half-opening angle of 42° (the relativistic limit of the Cherenkov radiation opening angle) is maximized.

Cable Hole Muons

The top of the detector includes twelve holes through which the cables supplying the high voltage and return signals of the PMTs pass through. Because of the cable bundles there are no OD PMTs to act as vetos installed at these positions. As a result, cosmic ray muons

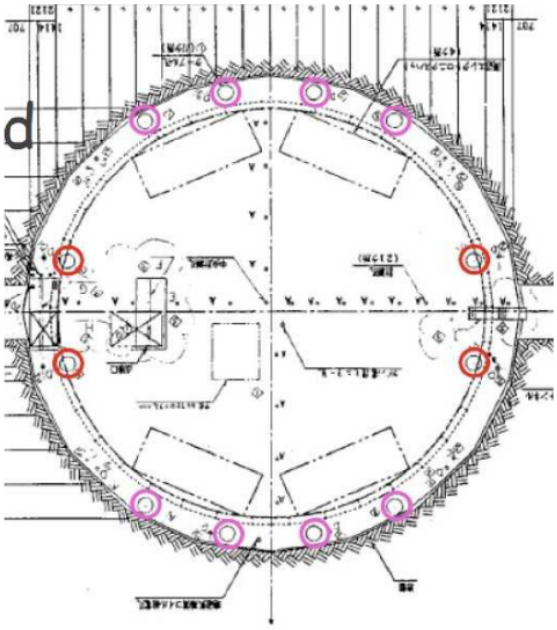

Figure 5.2: Location of the cable holes in the top of the tank. Red circles indicate holes with veto counters and pink circles those without. Taken from [92].

which pass through these holes can enter the ID without depositing appreciable energy in the OD. Special veto counters and a dedicated set of cuts were used to remove these events from the reduction. These cuts have an inefficiency (incorrectly eliminating true neutrino events) of less than 0.01%. The veto counters, which are 2 $\times$ 2.5 m plastic scintillation counters, were installed in four of the twelve cable holes in 1997. A schematic of the twelve holes and the four veto counters is shown in Fig. 5.2.

Events with at least one veto counter hit and a reconstructed vertex within 4 m of any of the veto counters were rejected. A new cut was introduced in SK-IV to reject events which pass through cable holes that do not have veto counters. The criteria for this cut are:

1. goodness ≥ 0.4 (Eq. 5.1
2. $\mathrm{PE}_{total} > 4000$ p.e.s (total number of ID p.e.s)
3. reconstructed as downward-going ($\cos\theta < -0.6$)
4. $\mathrm{L}_{veto} < 2.5m$, where L_{veto} is the distance from reconstructed vertex to cable hole

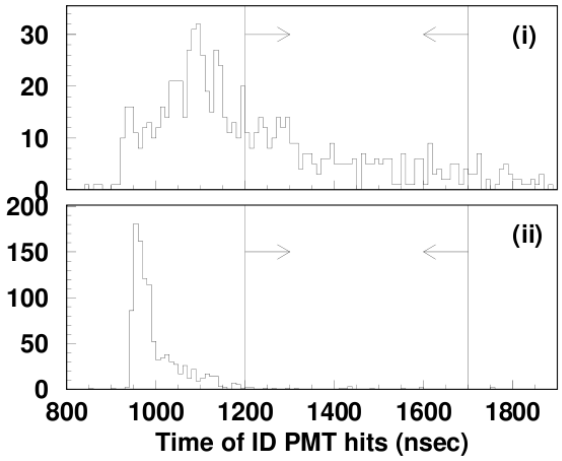

Figure 5.3: Typical flasher (i) and FC neutrino (ii) event timing distributions. Taken from [87].

Flasher Event Cut

Flasher events are caused by repetitive internal discharges of PMTs and have a broader event timing than actual neutrino-induced events. They are removed as events which satisfy the following criteria:

1. SK-I: $\mathrm{NMIN}_{100} \geq 10$ OR $\mathrm{NMIN}_{100} \geq 10$ if the number of ID PMT hits ≤ 800
2. SK-II,-III and -IV: $\mathrm{NMIN}_{100} \geq 20$

where NMIN_{100} is the minimum number of ID hits found in a sliding 100-nsec window that follows the event trigger. The timing distributions of typical flasher and FC neutrino events are shown in Fig. 5.3. The distributions of the variables used in these selection cuts for FC data and MC are shown in Fig. 5.4. As shown in the figure the cuts remove a majority of flasher events in the data which tend to have larger NHIT_{100} values.

Other Cuts

Accidental coincidence events occur when a low energy background event causes a trigger to be applied while a cosmic ray muon coincidentally passes through in the same trigger

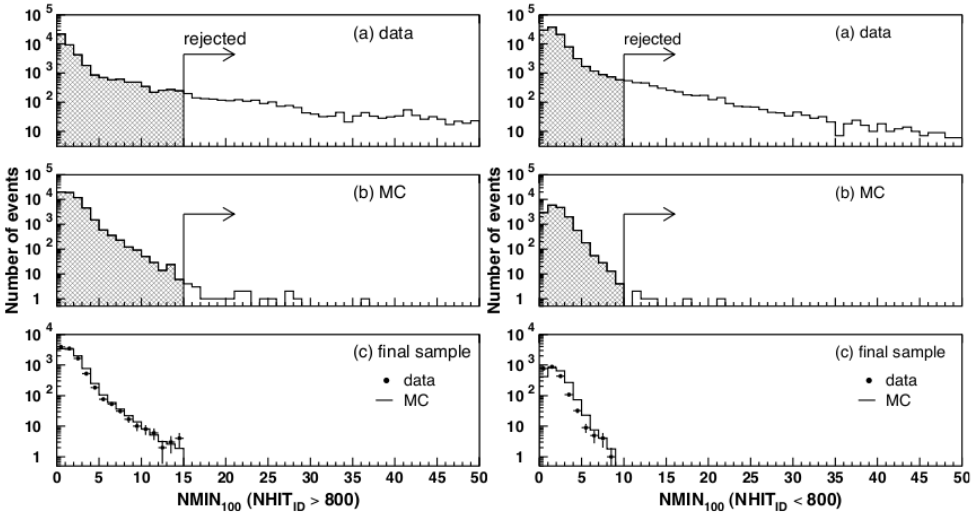

Figure 5.4: Typical NMIN_{100} distributions for data (a), MC (b) and post-FC3 data and normalized MC (c) samples. Taken from [87].

window. These events can survive the first FC reduction steps because their OD activity surrounding the initial low-energy event timing is zero or negligible while the muon event deposits a significant amount of energy in the ID. These events can be removed by requiring that $\mathrm{NHITA}_{off} \geq 20$, where NHITA_{off} is the number of OD hits within +400 nsec to +900 nsec after the event timing, and $\mathrm{PE}_{off} > 5000$ p.e.s (2000 for SK-II), where PE_{off} is the number of total p.e.s detected in the ID within the same 500 nsec timing window. Remaining low energy events from radioactive backgrounds or electronics noise are removed as events which have $\mathrm{NHIT}_{50} < 50$ (25 for SK-II) where NHIT_{50} is the number of hits in a sliding 50 nsec window. The PMT timings are corrected to include photon TOF after assuming a single vertex source for all photons which is determined by the peak of the timing residual distribution. After all cuts in FC3 reduction are applied, there are approximately 35 events/day remaining.

5.1.4 Fourth Reduction

The FC fourth reduction is dedicated to remove remaining flasher events. Periodic flasher events tend to have a physical charge pattern which is highly correlated to all other events caused by the same flashing PMT. An example of two flasher events separated by about 5 minutes is shown in Fig. 5.5. An algorithm designed to identify flashers is applied to for the fourth reduction. The algorithm includes:

1. Divide the ID surface into 1450 patches, each including between 6 and 9 PMTs
2. Calculate a correlation r for each patch based on its charge for pairs of events, where r is
$$r = \frac{1}{N}\sum_{i}\frac{(Q_i^A - \langle Q^A\rangle)\times((Q_i^B - \langle Q^B\rangle))}{\sigma_A \times \sigma_B}, \tag{5.2}$$
where N is the number of patches, i is the PMT index, A and B represent the two events in consideration, $\langle$Q$\rangle$ is the averaged charge and σ is the charge distribution's standard deviation.
3. Calculate the distance DIST$_{max}$ between the PMTs which have maximum charge in each event and apply an offset $r = r + 0.15$ if DIST$_{max} < 0.75$ m.
4. Mark A and B as matching events if the $r > r_{th}$ where r_{th} is a threshold quantity that is a function of the total number of ID p.e.s in each event.

The same procedure is applied for 10,000 events before and after the target event each making a pair with the target event, and the number of matching events are tallied. Events are then removed by a 2-dimensional cut using r and N_{match} as the selection variables. A sample plot of this selection for SK-I is shown in Fig. 5.6.

5.1.5 Fifth Reduction

The fifth and final stage of FC reduction aims to remove all remaining background events. The specific backgrounds which are targeted are as follows.

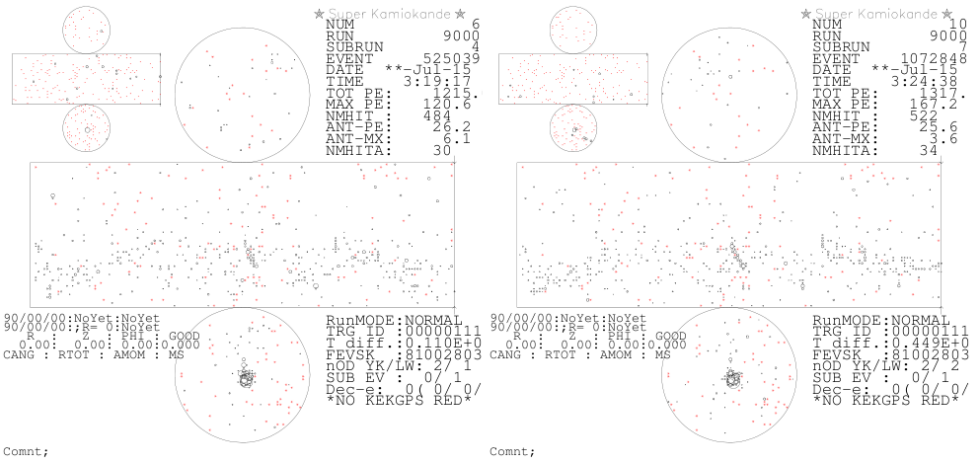

Figure 5.5: A typical pair of flasher events caused by the same PMT separated by 5 minutes. Taken from [88].

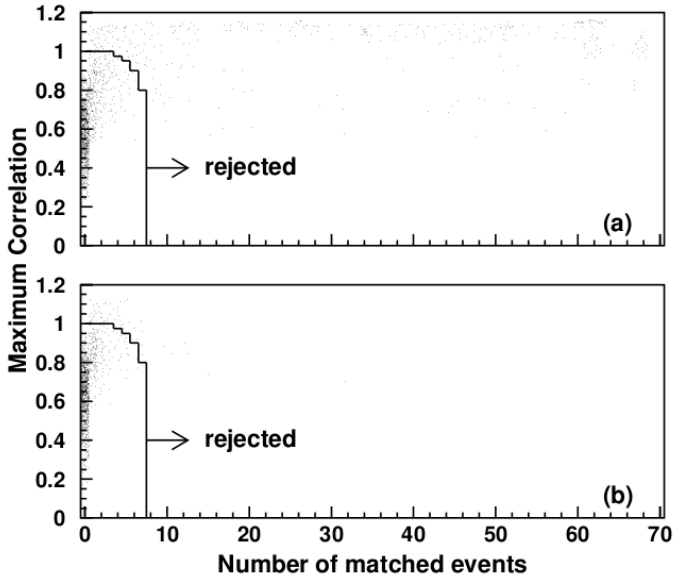

Figure 5.6: The criterion for removing flasher events in FC4. Vertical axis shows correlation (r) and horizontal axis shows number of matching events. Taken from [88].

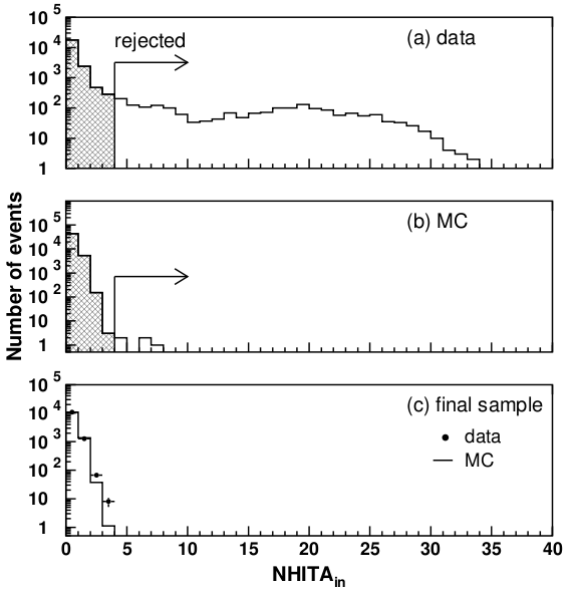

Figure 5.7: The removal of stopping muons in FC5. NHITA$_{in}$ is shown for (a) data, (b) MC and (c) final FC sample with normalized MC. Taken from [88].

Stopping Muons

Stopping muons which were not eliminated in FC3 are now removed with a similar cut that reconstructs the muon entrance point in a more precise manner. Events with NHITA$_{in} \geq 5$ where NHITA$_{in}$ is the number of OD PMT hits within 8 m of the reconstructed entrance point in a sliding 200 nsec window that covers $\pm$ 400 nsec around the event time. The entrance point is estimated by constructing the distribution of PMT residual times for each possible candidate vertex and selecting the point which yields the sharpest peak in the residual time distribution. The entrance point is then estimated as the backward extrapolation of the vertex. Fig. 5.7 shows the effect of this cut.

Invisible Muons

Muons which are below Cherenkov threshold can escape detection yet produce a decay electron which is reconstructed as an FC neutrino event. These events can be identified by an OD signal (from the muon before it goes under Cherenkov threshold) detected ahead of

a low-energy signal in the ID from the electron. Events satisfying the following criteria are removed:

1. PE_{tot}inID < 1000 p.e.s
2. $NHITAC_{early} > 4$, where $NHITAC_{early}$ is the maximum number of OD hits in a cluster in a large timing window (-8800 nsec to -100 nsec) preceding the ID event.
3. $NHITAC_{early} + NHITAC_{500} > 9$ if $DIST_{clust} < 500$ cm OR $NHITAC_{early} > 9$ if $DIST_{clust} \geq 500$ cm, where $NHITAC_{500}$ is the number of OD PMT hits in the cluster in a (-100 nsec, +400 nsec) window surrounding the event, and $DIST_{clust}$ is the distance between the two OD clusters described by the other variables.

Other Cuts

Accidental coincidences of a low-energy event and a muon are further removed by selecting events with more than 20 late hits in a 200 nsec sliding window which starts searching 400 nsec after the event timing. This cut is found to be effective in reducing background without significantly removing any data. Finally, flasher events which have a long timing distribution tail are removed by a stricter version of the corresponding FC3 cut. Events found to have a goodness $5.1 < 0.4$ and at least five hit ID PMTs in a 100 nsec sliding window covering the interval [+300,+800] nsec relative to event timing are selected for removal.

5.1.6 Final FC Sample

The official event criterion for FC events remaining after all reduction stages are (1) vertex inside ID fiducial volume, (2) NHITAC (number of hits in the largest OD cluster) < 9, (3) visible energy (assuming electron event) > 30 MeV. The efficiency (calculated as percentage of true FC events that survive the reduction) of FC reduction is estimated by the atmospheric FC MC and is found to be greater than 99%, with an estimated systematic uncertainty of less than 1%. The fiducial volume cut in addition to the cuts mentioned above greatly reduce the background from radioactive sources and cosmic ray muons. These background contaminations are each estimated to be less than half a percent for all FC event samples[88]. The final fiducial volume FC sample (FCFV) has approximately 8-9 events/day.

5.2 Partially Contained Reduction

The PC sample represents events with higher average energy than the FC sample. PC event tracks penetrate the wall separating the ID and OD and cause at least 10 OD hits. The additional OD activity is the only main difference from FC events but this causes the reduction steps to differ drastically because many of the FC cuts are OD-based. PC events are predominantly muons because electrons rarely travel far enough above Cherenkov threshold to exit the OD. The main goal of the PC reduction process is to eliminate cosmic ray muons background events, which can either be through-going or stopping. An overview of the reduction steps is written here, while more thorough descriptions can be found in the theses [88, 19].

5.2.1 First Reduction

The first step in the PC reduction, which is run online, removes easily identifiable low-energy events and cosmic ray muons. Events satisfying the criteria

1. Total number of ID p.e.s $\geq$ 1000
2. Width of hit OD PMTs' timing distribution $\leq$ 260 ns
3. Number of OD hit clusters $\leq$ 1

pass through the first reduction. The first cut corresponds to a minimum momentum of 310 MeV/c for muons, safely below the event threshold of 500 MeV/c for exiting PC events which is used. The second and third cuts are effective at removing cosmic ray muon backgrounds. Through-going muon backgrounds pass through the OD twice, so they typically produce multiple OD hit clusters with a broad overall timing distribution. Here a cluster is defined as all PMTs with hits within 8 m of a PMT that detects at least 8 p.e.s. Approximately 14,000 events/day remain after PC1 reduction.

5.2.2 Second Reduction

PC2 reduction uses a different cluster definition algorithm to remove backgrounds. The ID and OD walls are divided into a grid of isolated patches, 21x21 and 11x11 in number,

respectively. The charge in each grid (sum of charges of all PMTs in the grid box) is calculated, and the charge vector gradient is taken for each grid to separate all grid boxes into clusters. After constructing the clusters events meeting the following conditions are saved:

1. Number of OD hit clusters with more than 6 hit PMTs ≤ 1
2. Endcaps vs wall cut: events which a small number of hits in the endcaps (top and bottom of the detector) relative to their wall (barrel) hits are saved. The 2-d function which determines the threshold is shown in Fig. 5.8. Events above the red line are rejected as corner clipper events.
3. Number of p.e.s within 200 cm of the PMT with the highest charge in the ID hit cluster closest to the OD cluster is above a threshold which is a function of the OD cluster hits (see [19] for details).

The first cut is designed to remove more through-going muons. The second cut is a topology-based cut which identifies corner clipper events that deposit most of their energy on the edge of the detector between the top and barrel or the bottom and barrel. The third cut here identifies and removes stopping muons which deposit charge in the OD but not significantly in the ID. These cuts reduce the PC event rate to approximately 2000 events/day.

5.2.3 Third Reduction

A test for flasher events is applied in the third reduction by cutting events with broad timing distributions, as in FC reduction. This is done by removing events for which $NMIN_{100}$ (the minimum number of hit ID PMTs in a sliding 100nsec window from +300 to +800 nsec after the event) > 14 or $NMIN_{100} > 9$ if the number of hit ID PMTs is < 800. A fitter called `pfit` is used to reconstruct the particle's interaction vertex and direction. The entrance point is estimated by extrapolating the vertex backward with this direction, and events for which the number of hits in the OD within 8 m of this entrance point is fewer than or equal to ten survive the reduction. Events are required to meet both of these criteria to be saved. Plots showing the removal of events based on the last cut for data, MC and the final samples for both are shown in 5.9

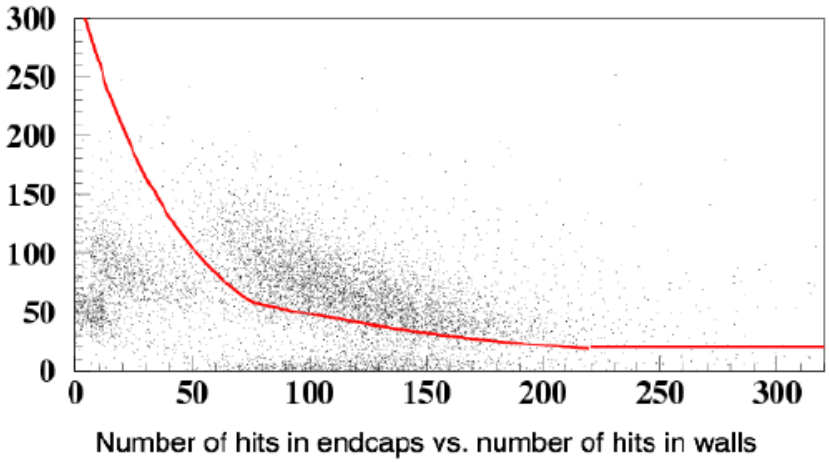

Figure 5.8: Number of PMT hits in top and bottom versus number in barrel for PC data. Events above the red line are rejected. Taken from [19].

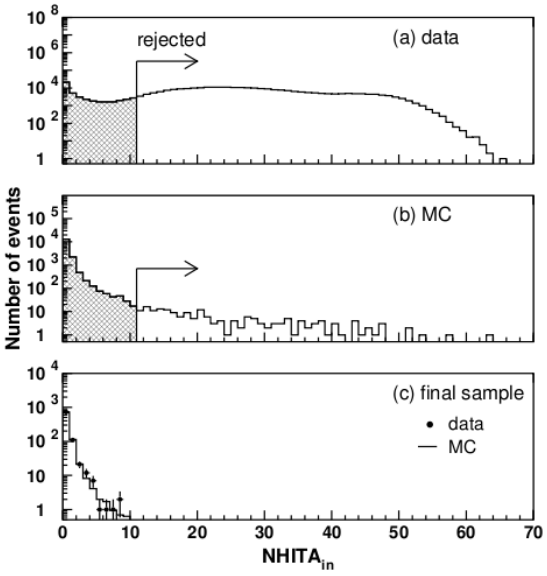

Figure 5.9: Distributions of NHITA$_{in}$ for data (a) and MC (b) for the PC3 cut, and the final data and MC samples (c). Taken from [88].

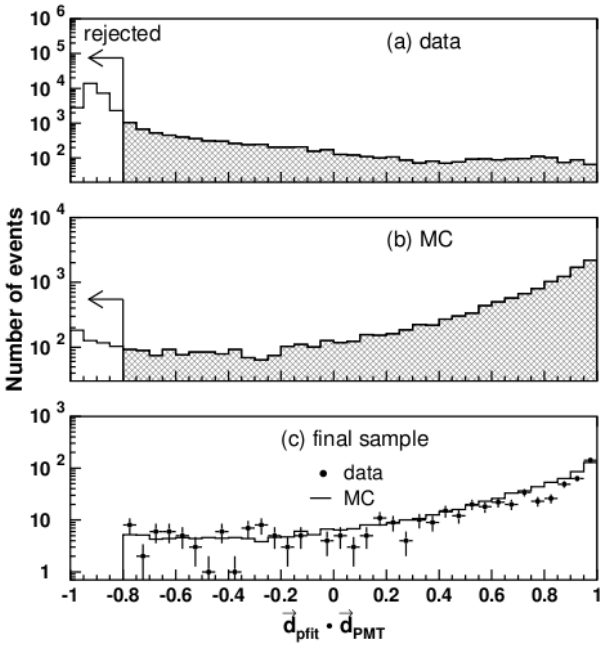

Figure 5.10: The effect of the PC4 cut which is based on the pfit direction and the direction from the vertex to the earliest saturated PMT. Shown for SK-1 data(a), MC(b) and their final samples(c). Taken from [88].

5.2.4 Fourth Reduction

Fourth reduction relies on the muon fitters `pfit` and `mfmufit` to remove mostly cosmic ray muons with little OD activity. The latter fitter determines the entrance point of the particle to be the location of the earliest ID cluster. Events with a total ID charge (`Qismsk`) greater than 1000 p.e.s are saved. Events with longer track lengths are typically cosmic muons and those with a length greater than 3000 cm are removed. A goodness of fit for the muon fitters is calculated and events for which this value is above 0.85 (a good fit indicating a high probability of a through-going muon) are rejected. Events in which the distance between the vertex as calculated by the point fitter and the corner of the tank is greater less than 150 cm are also removed. These events would eventually be removed by the fiducial volume cut but their removal during PC4 saves computation time.

Finally only events satisfying $\vec{d}_{pfit} \cdot \vec{d}_{PMT} > -0.85$ are saved. These vectors are the track

direction as found by the point fitter ($\vec{d}_{pfit}$) and the direction from the vertex to the earliest saturated ID PMT ($\vec{d}_{PMT}$) and this cut removes cosmic muons which are likely to have opposite directions for these two vectors. A sample plot for SK-1 data and MC showing the effect of the vector cut is shown in Fig. 5.10. The output of PC4 is approximately 20 events/day.

5.2.5 Fifth Reduction

The fifth and final stage of the PC reduction includes many specific cuts targeting the remaining backgrounds. In this step more precise fitters (called `apfit`, `stmfit`, `pfdofit` and `msfit`) are used to fit the event. Events with a total (ID) charge greater than 3000 p.e.s are saved, removing low energy events. A detection of 3000 p.e.s indicates a muon of approximate momentum 500 MeV/c and because muons which exit the ID and reach the OD typically have at least 700 MeV/c, this cut is safe. The number of OD hits, `nhitac`, is used to distinguish stopping ($<$ 16 PMTs) and through-going ($\geq$ 16 PMTs) PC events. Next a combination of hits based on OD cluster information are applied. Multiple OD clusters are assumed and they are ranked according to their charge. Events which have fewer than 2 hits in their third-highest charge cluster, a distance between the two highest-charged clusters of less than 20 m (through-going muons are likely to fail this cut) or which have fewer than 10 p.e.s in the second-highest charge cluster are all saved (only one of these three conditions needs to be satisfied). Additionally there are cuts made on events which fall into calibration time windows and runs which exhibited problems with the electronics huts.

Junk cuts include those events for which activity spread across two triggers or in which the OD had a problem are also applied. Cable hole muon cuts are applied similarly to the FC reduction. Events with one veto counter hit and $\vec{d}_{ring} \cdot \vec{d}_{veto-vertex} > -0.8$, were $\vec{d}_{ring}$ is the reconstructed ring direction and $\vec{d}_{veto-vertex}$ is the direction from the reconstructed vertex to the hit veto counter, are considered cable hole muons and removed.

A set of cuts for removing remaining stopping and through-going muons is also added here. To eliminate stopping muons, events which have more than ten entry hits in the entrance cluster found by `msfit` are removed. The charge in a cone of radius 8 m around

the ID entrance location from the reverse extrapolation of the `pfdofit` direction is required to make up 60% of the ID total and contain fewer than six hits. The number of hits within 8 m of the OD entrance point (`Umehit8m`, same as above) as calculated by `apfit` is required to be fewer than ten. The angle between the fitted direction and the direction from the vertex to the highest charge OD cluster (all calculated with the precise fitters) is required to be no more than 90°.

Through-going muons which travel vertically downward in the region between the ID and OD leave a track which resembles a millipede are removed by the so-called `geji`[1] cut[19]. A separate clustering algorithm called `grad cluster` is used to identify OD clusters and the two with the most hits are each required to have fewer than 10 hits. If the entrance and exit hit clusters as found by msfit have at least five hits each, then events for which the time difference between the average top and bottom hit timing divided by the distance separating them is between 0.75 and 1.50 are removed as through-going candidates. The visible energy as calculated by `apfit` (a different version of the variable `Evis`) along with the estimated track length between vertex and OD exit position are used to remove remaining corner clipper events. Finally low energy events with `Evis` < 350 MeV within the fiducial volume are removed.

5.2.6 PC Reduction Summary

The PC reduction was found to have efficiencies of 88% (SK-I), 83% (SK-II), 96% (SK-III) and 96% (SK-IV) for the data sets used in the analyses described in this work. These numbers are taken from collaboration meeting slides. The final background contamination comes mainly from cosmic ray muons and is accounted for by manual eye scanning of the final event sample. The majority of this background is outside the FV and the contamination within the FV is found to be less than 1.0% for each detector period. A systematic uncertainty is estimated for the PC reduction by comparing data and MC (for ID cuts) and generating toy MC sets with different OD tuning parameters and seeing how they differed (for OD cuts). The uncertainties from each stage of reduction were then added in

[1] "Geji" is the word for millipede in Japanese.

PC	SK-I	SK-II	SK-III	SK-IV
reduction step	selection efficiency %			
1st	98.98	98.58	99.09	99.63
2nd	96.74	93.43	98.52	98.73
3rd	95.69	92.32	98.51	98.68
4th	89.86	84.60	97.87	97.42
5th	88.66	74.80	96.61	96.15
5th (FV)	80.98	74.80	88.80	86.30
Cosmic Ray BG Contamination	0.2%	0.7%	1.8%	0.6%

Table 5.1: A summary of the PC reduction efficiencies for each detector phase (top) and the estimates of the corresponding cosmic ray background contamination percentages.

quadrature to calculate the overall uncertainty. The efficiencies for each reduction stage and run period along with the estimated background contaminations are shown in Table 5.2.6. The selection efficiencies shown in the table are for events with real vertices in the fiducial volume, number of OD hits > 15 (9 for SK-II) and total observed charge > 3000 p.e.s.

5.3 Upward-going Muon Reduction

The upmu sample represents muon-like events with the highest average energy among all atmospheric neutrino data samples. Upmus are created when a muon neutrino scatters from a nuclei via a charged-current weak interaction in the rock either beneath or next to the detector cavity. An example Feynman diagram for this interaction is shown in Fig. 5.11. There is also a small contribution to the upmu sample from neutrinos scattering from oxygen nuclei in the OD water and then entering the ID with upward momentum. The produced muon enters SK with net upward momentum and deposits energy in both the ID and OD. The fundamental difference between the FC/PC samples and the Upmu sample

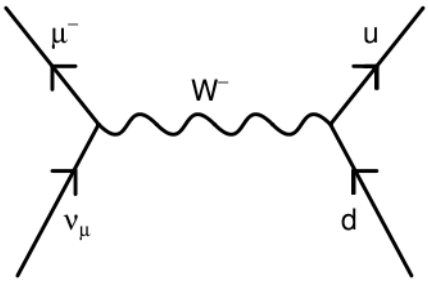

Figure 5.11: Charged-current weak interaction which produces can produce an upmu. Taken from [110].

is that the vertex of the neutrino interaction is outside the ID. This topology implies that the measured energy represents at best a lower bound on the muon energy. The upmu sample is used in zenith angle oscillation analyses such as the ones described here, and is also effective for astrophysical neutrino studies because astrophysical neutrino signals are expected to have a harder energy spectrum than atmospheric neutrinos (see [110],[109] for SK analyses on such topics). The final upmu data samples contain between 1.4 and 1.5 events/day.

Upmu events are divided into the three sub-categories of stopping (muons which stop in the detector), through-going non-showering (more energetic events which pass through the entire detector) and through-going showering (the highest energy events). A χ^2 measure is used to separate the through-going sample into showering and non-showering events. Showering events are characterized by the drastic (less uniform than typical ionization energy loss) mechanisms of energy loss which occur such as Bremsstrahlung radiation, pair production and photo-nuclear processes. Typical parent ν_μ energies are tens of GeV for stopping, few hundreds of GeV for thru, and many hundreds of GeV to one thousand GeV for showering. The muons created from their interaction are roughly a few GeV, tens of GeV, and a few hundred GeVs for the same categories, respectively [110]. True energy distributions for SK-III MC for these particles and event categories are shown in Fig. 5.12.

The upmu reduction is designed to reject background events while saving true upmu events and nearly-horizontal events. Much like FC and PC reductions, multiple fitters are

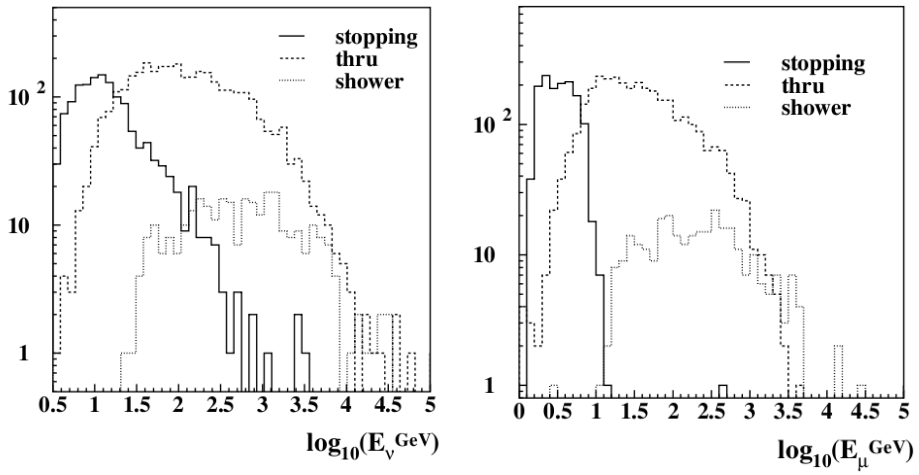

Figure 5.12: Neutrino (top) and muon (bottom) energies for the three upmu samples as generated in SK-III MC (from [110].

applied during the reduction and nearly-horizontal events which were initially classified as downward-going may become upward-going after the application of more precise fitters. Additionally nearly-horizontal events are used to estimate the background of cosmic ray muon events which up-scatter into the detector and are mistakenly categorized as an upmu. As detailed below eye scanning will constitute the final check of the upmu sample and this helps to remove backgrounds such as corner clippers, multi-cluster events (multiple muons typically) and very high energy downward-going showering events which saturate the detector and are mis-reconstructed as upward-going.

5.3.1 Upmu First Reduction

The first step in this reduction chain is the `umred1st` program which runs continuously online. The subruns (ten minutes of data or ten MB of data, whichever occurs first) are merged together into larger subruns) which are easier for processing. A flow chart of the `umred1st` selection criteria is shown in Fig. 5.13. Events from the HE trigger stream are passed to the first step saves ultra-high energy (UHE) events, characterized by having a charge greater than 1.75 Mp.e.s, for astrophysical studies. UHE upmu events are very rare and a past analysis with SK-I data found only one event, against an expected background

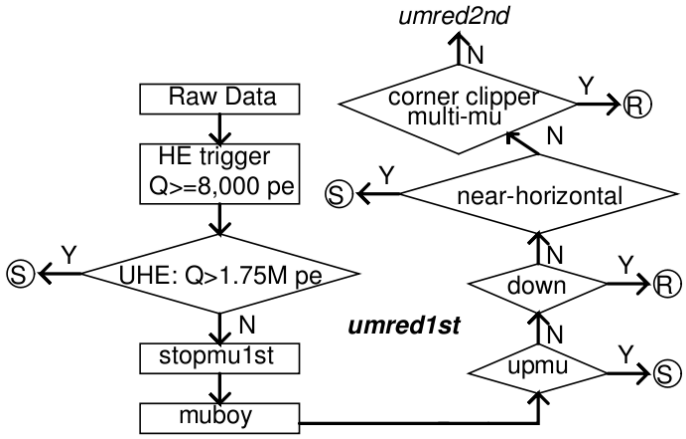

Figure 5.13: A flow chart describing the umred1st selection and rejection steps. Taken from [110].

of 0.46 ± 0.23 events[46].

Next two routines called `stopmu1st` and `muboy` are applied. The former uses mostly OD information to apply one of eight flags to each event, as shown in Table 5.2 without estimating any directional information. The OD cluster-finding algorithm is based on the idea that for typical muon events passing through a PMT result in nearly the same timing and charge information for all nearby surrounding PMTs. Clusters are found by centering the search on PMTs which have a local maximum charge value and requiring at least seven nearby neighbors to have at least 8 pe within a specified 800 nsec window. One check for this algorithm is the number of clusters found; events which are found to have exactly two clusters are classified as thru-going while those with two or more clusters separated by at least 8 m are tagged as multi-muon events. More details can be found in Reference [18].

The latter fitter `muboy` is very important in the upmu reduction process because it most background events are rejected by this fitter. It began as a fitter for muons which produce spallation products that are backgrounds in low-energy analyses, and was adapted for use in high-energy studies[14]. It is similar to `stopmu1st` but in addition estimates a unit vector for the direction of the muon (`muboy_dir[i]`, where i can correspond to x(1), y(2) or z(3) directions), a track length and an associated goodness of fit quantity (`muboy_goodness`). It

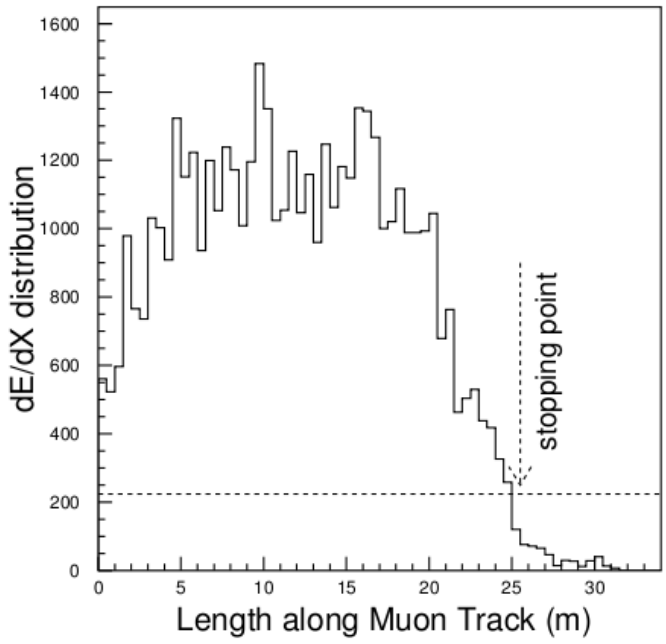

Figure 5.14: The dE/dx histogram for stopping muons used to estimate track length by `muboy`[18].

is important to note here that the index i represents the cosine of the unit direction vector with respect to each axis, so that upward-going muons will have a dir[3] component which is negative because this means the z-component of the direction vector is greater than 90° down from the upward-pointing local z-axis.

The track length is calculated by constructing a dE/dx histogram of the muon's energy loss. The point along the track where the number of photons emitted in a 1-meter interval goes below less than 40% of the average from the first 1.5 m of the track is defined as the stopping point. A typical dE/dx histogram for this calculation is shown in Fig. 5.14. The table of possible `muboy` flags is shown in 5.3. Muboy mainly uses ID information for assigning these flags.

Events which have `muboy_goodness` > 0.3, `muboy_class` (flag number) $\neq 0$, and $0 \geq$ `muboy_dir[3]` ≥ 1 are saved as upmu candidates. Near-horizontal events for which `muboy_dir[3]` indicates a nearly horizontal direction are also saved with a near-horizontal

Flag	Meaning
0	thru-mu candidate
1	ID off / calibration
2	decay electron
3	$Q < 8{,}000$ p.e.s (3,000 p.e.s for SK-II)
4	stopping candidate
5	multi-muon
6	no result
7	pedestal event

Table 5.2: A summary of all possible flags for each event that passes through `stopmu1st`.

flag. Events which are identified as being downward-going, having multiple muon rings, very short tracklengths or large forward/backward charge ratios were rejected here. The upmu first reduction output contains about 9,000 events/day on average.

The output of first reduction is passed to a merger program which merges the many subruns into a smaller number. After merging each run typically contains 3 or 4 merged subruns.

Flag	Meaning
0	invalid fit
1	thru-mu, good fit
2	stop-mu, good fit
3	multi-muon, type 1
4	multi-muon, type 2
5	corner clipper

Table 5.3: A summary of all possible flags for each event that passes through `muboy`.

5.3.2 Upmu Second Reduction

The second upmu reduction, `umred2nd`, has more time-consuming fitting algorithms designed to more carefully separate upmus from downward-going muons and other backgrounds. The first fitter is called `stopmu2nd` and its responsibility is to fit the direction of events which were classified as stopping in the first reduction. The algorithm first makes guesses for the entrance and exit points and then calculates goodness parameters which are based on how many PMT hits fill the center of the Cherenkov cone ring and the sharpness/fuzziness of the ring edges (more details in [18]). The entrance point is then fixed and the muon track direction varied while another goodness of fit parameter (similar to 5.1) based on residual PMT timing is maximized.

The event's directional information puts it into one of six distinct categories: failed fit, downward-going ($\cos(\theta) <$ -0.12), near-horizontal (-0.12 $\leq \cos(\theta) <$ 0), regular upmu, downward-going (top entry) and nearly-horizontal (top entry). Two fitters designed for fitting through-going events, called `thrumu1st` and `thrumu2nd`, are called next. The former assigns essentially the same flags as `stopmu2nd` except for the definition of the threshold for downward-going, which is set to -0.1 instead. It is designed to be a quick fitter and as a result is more likely to return misfits than the other fitters. The latter specializes in messy fits such as showering muons and multi-muon events and has the same set of flags for assignment. The flags from the two fitters are combined and events which are categorized as downward-going are rejected, whereas horizontal and upmu events are saved along with their stopping/thru-going decision. The output of upmu second reduction is typically around 250 events/day.

5.3.3 Precise Fitter

The next step applies the most precise fitting in the reduction chain with a program called `precisefit`. The fit is not applied to events with fewer than 8000 p.e.s (amount of light too small to find good fit) and events with more than 175000 p.e.s (saturation of the ID prevented the fitter from working well) (for SK collaborators this information can be found in the header file `umparm.h`). It uses three fitters `upmufit`, `OD-fit`, `TDCfit`. `upmufit` was

taken from the FC/PC `msfit` algorithm and adapted for upmu fitting. It works by taking a given entry point and direction and compares the expected number of p.e. to the observed number in each PMT, then calculates a χ^2-statistic to quantify this. The calculation of the expected number of p.e.s from Cherenkov light is given by the expression

$$N_i^{exp} = \left(\alpha_u \frac{1}{l_i(\sin\theta_i + l_i \frac{d\theta}{dx})} \sin^2\theta_i + N_i^{\delta}(\theta_i) \right) exp\left(-\frac{l_i}{L_{atten}} \right) f(\Theta) + S_i \qquad (5.3)$$

where i is the PMT index, α_u is a normalization factor, θ_i is the angle of incidence relative to normal, N_i^{δ} is the number of p.e.s expected from interactions caused by the ionized electrons (sometimes called δ-rays, hence the index), L$_a tten$ is the water attenuation length from 3.3 and $f(\Theta)$ is the angular dependence of the PMT acceptance. The term following the normalization factor represents the change in the Cherenkov opening angle due to the muon losing energy. A log-likelihood is calculated from this number and the number of observed p.e.s and this is used to create a χ^2-statistic. This statistic is calculated for all possible entry and exit points and the points which minimize this value are taken for the fit.

The second fitter `OD-fit` uses only OD clustering information to fit a vertex and direction. This is useful for events which undergo energy loss via Bremsstrahlung radiation, which creates a fuzzier ring edge than typical ionization events. Clusters are defined to have at least 8 nearby neighbor PMTs surrounding a PMT with hits between 800 ns and 1300 ns timing relative to the trigger. The cluster with the earliest average timing is chosen as the entrance cluster and the cluster with the maximum number of hit PMTs is assumed to be the exit cluster.

The third and final fitter in this step is `TDCfit`, which is also adapted from a contained event fitter. The first step to this fitter is to find a rough vertex and direction by minimizing the differences of all timing residuals. Next, a charge statistic is constructed to test the quality of the Cherenkov ring edge location for varying track directions (details in **??**). The track which yields the maximum effective charge in the ring for this statistic is temporarily stored. Finally a finer vertex fit is achieved by taking into account light scattering effects and testing the goodness of fit based on the residual timing information again. These steps

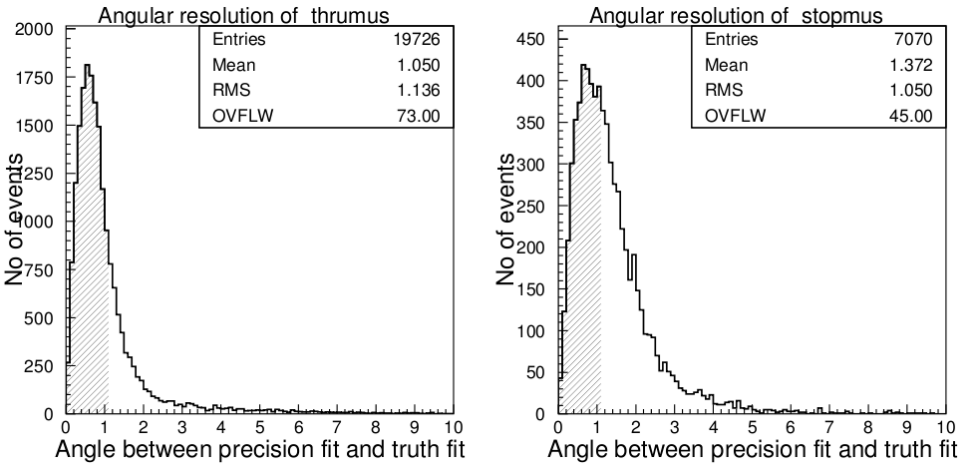

Figure 5.15: The distributions of precise fit direction and true direction for a 40-year SK-I MC sample. Taken from [18].

are iterated until successive vertices are found which differ by no more than 50cm. For all events the three above-mentioned fitters are applied and the eventual final fit is chosen from one of them. The number of events which met the charge requirements outlined at the beginning of this section and were subsequently passed through the precisefit algorithms was approximately 100 events/day.

The precise fitter is found to have good agreement between the true direction and its fitted direction. This was tested with a 40-year MC sample when it was first implemented in SK-I. A plot of the angle between the precisefit and true directions is shown for thru-going muons and stopping muons in Fig. 5.15. As shown in the figure the resolutions are found to be approximately 1°.

Showering Algorithm

A showering algorithm used to identify very high-energy muons which lose energy through processes such as pair production, Bremsstrahlung and other electromagnetic shower cascades as opposed to ionization (the most dominant form of energy loss for muons up to many hundreds of GeV) is applied as a subroutine within the precise fitter. The energy losses from

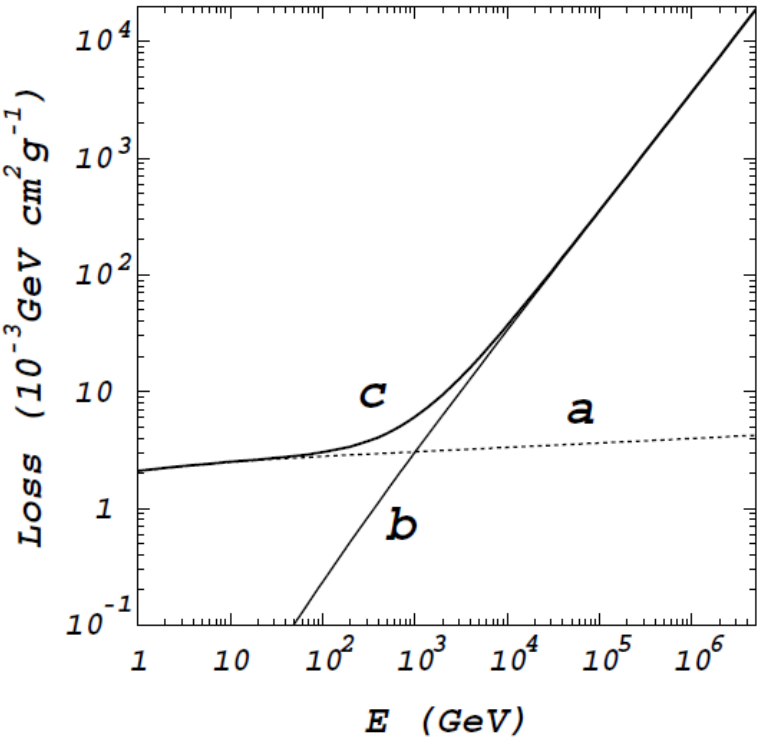

Figure 5.16: Muon energy losses in water. Curve (a) shows losses due to ionization, (b) shows radiative losses, and (c) shows the sum of both[91].

these showering mechanisms become equal to those from ionization for muons with energies around 1 TeV. A diagram of muon energy losses in water is shown in Fig. 5.16[91]. Events which are tagged as through-going pass through this algorithm. A χ^2-statistic is defined which adds contributions from fluctuations in charge deposition above the average value. Ionizing muons lose energy at the roughly steady value of 2.2 MeV/cm, whereas showering muons undergo more sudden, drastic energy loss.

.

The track of the muon is broken up into 50 cm intervals and the corrected charge deposited on the PMTs from each segment (Q^i_{corr}) is compared to the average from all segments ($\langle Q_{corr} \rangle$). Additionally this average corrected charge is compared to the average value for non-showering muons, which is given as a function of the track length. The χ^2-statistic takes the form

Phase	δ Q
SK-I	0.10
SK-II	2.50
SK-III	-0.30
SK-IV	-0.30

Table 5.4: A table of the δ Q tuning parameters for the showering upmu selection.

$$\chi^2 = \sum_{i=3}^{N-2} \left\{ \frac{[Q^i_{corr} - \langle Q^i_{corr} \rangle]^2}{\sigma^2_{Q^i_{corr}}} + \frac{[\langle Q^i_{corr} \rangle - Q(l)]^2}{\sigma^2_{Q(l)}} \right\} \tag{5.4}$$

where the σ variables are the statistical errors of their corresponding charges. The bounds on the sum ignore the first and last meter of the track. Since showering events are by definition through-going, this corresponds to ignoring the contributions near the walls of the detector, where the corrected charge is harder to calculate. This is calculated for all track segments which have $Q^i_{corr} - Q(l) \geq -2.0$. This latter condition prevents the calculation from including events which have large energy loss fluctuations below the average which are not considered contributions to a showering-type event. This occurs for approximately 0.5% of events in the MC - usually through-going muons with poor fits or stopping muons which were incorrectly classified as through-going. A second variable, Δ, is also calculated to identify these types of events. It is defined by

$$\Delta = \langle Q_{corr} \rangle - Q(l) - \delta Q \tag{5.5}$$

where δQ is a tuning parameter that changes for each SK run period and is set so that the peak of the Δ histogram for MC is at zero. A table of the tuning values for each SK run period is shown in 5.4. After this tuning the distribution of Δ is not perfectly peaked at zero and a systematic uncertainty which will be described in detail later in this section is calculated to account for this. The variables Δ and χ^2 are calculated for each through-going event (and saved in the variables `sh_delta` and `sh_chi1p`, for those using the SK data).

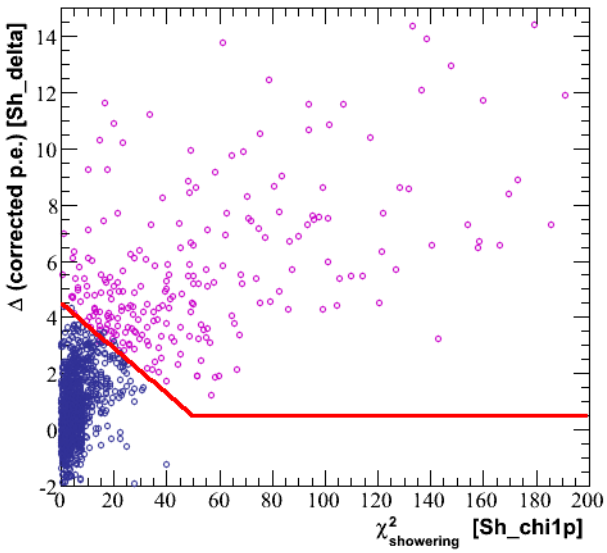

Figure 5.17: A 2-dimensional scatter plot of Δ (vertical axis) and χ^2 (horizontal axis) for showering event selection for SK-IV data. Magenta events above the red line are saved as showering, and blue ones below as non-showering.

The showering events are then officially selected by the following cuts:

$$\Delta > 0.5, \quad \chi^2 > 50.0$$
$$\Delta > 4.5 - 0.08\chi^2, \quad \chi^2 \leq 50.0$$

Scatter plots of these two variables for SK-I,-II,-III and -IV MC samples (taken from 200-years samples) are shown in Fig.5.17. The SK-II scatter plot exhibits a different topology due to the significantly reduced photocathode coverage. A study done with SK-III MC found that this cut selects about 70% of true showering events properly (for details please see [109]), which was deemed to be sufficient for studies of astrophysical neutrinos. In the case of atmospheric neutrino oscillations, the showering sample does not undergo significant oscillations due to its very high energies.

5.3.4 Upmu Third Reduction

The third reduction applies the selection cuts to the upmu data after the events have been given precise fits. The main goal here is to separate the stopping and through-going events. The criteria for through-going events are the following:

1. Number of entrance hits within 8m of entrance point (`Um_ehit8m`) > 10 (16 for SK-II)
2. Number of exit hits within 8m of entrance point (`Um_ohit8m`) ≥ 10 (16 for SK-II)
3. `precisefit` fitted track length ≥ 700 cm
4. `precisefit` fitted z-direction (`Fit_dir[3]`) ≤ 0

and the criteria for stopping events are:

1. Number of entrance hits within 8m of entrance point (`Um_ehit8m`) > 10 (16 for SK-II)
2. Number of exit hits within 8m of entrance point (`Um_ohit8m`) < 10 (16 for SK-II)
3. `precisefit` fitted momentum ≥ 1.6 GeV/c
4. `precisefit` fitted z-direction (`Fit_dir[3]`) ≤ 0

The `precisefit` fitted momentum is estimated from the total number of p.e.s in the Cherenkov ring detected in the ID. Note that in these cuts the direction is taken such that cos(z) = -1 corresponds to upward-going, and cos(z) = 0 is downward-going. For through-going events, the track length is easily estimated by the combination of entry and exit points. Thus, the track length cut is used to select those events. However, for stopping muons, there is no exit point and therefore the track length cannot be estimated this way. Therefore a cut is made on the momentum instead because it is known that a muon with a reconstructed momentum of 1.6 GeV/c has a range of approximately 7 m in water (see [109] for details). The distributions of MC and data for SK-IV are shown for the fitted tracklength and momentum in Fig. 5.18. After all third reduction selection cuts are applied, there are approximately 2.5 events/day remaining including all three event types.

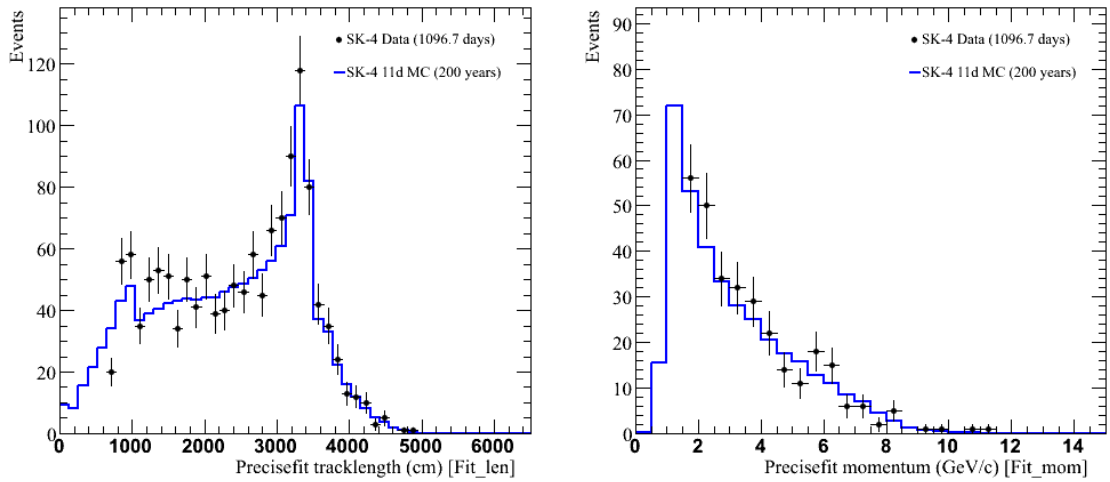

Figure 5.18: The distributions of fitted tracklength (left) for through-going events and fitted momentum (right) for stopping events from precisefit for SK-IV data and MC. Final data cuts are applied to the data, but not the MC.

5.3.5 Upmu Fourth Reduction

This is the final step in automated portion of upmu reduction and was introduced for the first time in SK-III. Most of the cosmic ray background is removed by the previous reduction steps. The majority of the remaining background are corner clipper events which deposit charge near one of the detector edges and have a very short track length. These events are not fit well by the precise fitter in many cases. Before the beginning of SK-III, the OD was optically segmented so that the top/bottom and barrel regions became distinct. After this separation identification of corner clipper was made easier[109]. Additionally in SK-III an extra step in the reduction process was added to reduce these events even further. This uses a precise OD-cluster fitting algorithm to remove events which had at least two OD clusters and whose fits from `muboy` and `precisefit` differed considerably. The total upmu data rate after this stage was approximately 1.75 events/day. From MC studies it is found that the efficiency of all automated upmu reduction steps was 98% or greater (depending on the zenith angle; upward-going events had nearly 100% efficiency). The purity of the event samples before the fourth reduction is only $\sim$ 55%, but the fourth reduction removes

a majority of background events and leaves the upmu sample with about $\sim 85\%$ purity in the end.

5.3.6 Automated Reduction

The author of this work has recently completed a software package which automates the upmu reduction steps mentioned above. Until this was implemented, each reduction stage after `umred1st` was run manually. In the new automated framework, a daily cron job manages a set of shell scripts which determine which new `umred1st` files are made each day, and then run them through all reduction steps. The reduction jobs are submitted to the parallel-computing cluster (`nqs`) and the number of events saved in each reduction step is tallied and shown in plots on a web page. The web page also includes a shift check so that AtmPD group members can monitor the quality of the new data as it is processed. A plot showing the event rates for all stages of upmu reduction which was made by this software package is shown in Fig. 5.19. The event rate for all stages is steady throughout the SK-IV period. The scripts and organization for this software are based upon those written for the FC automated reduction.

5.3.7 Eye Scanning

The final stage in upmu reduction is a manual scanning of all events which make it through all prior reduction steps. An expert trained to distinguish good upmu events from mis-categorized background scans the event displays for each event individually and decides whether to accept or reject each event. This is mainly used to remove corner clipper events with poor fits and very high-energy down-going muons which receive an upward-going fit because they have nearly saturated the detector. Since the addition of upmu fourth reduction in SK-III the purity of the eye scanning sample is very high to begin with. Of the approximately 1.75 events/day that survive all automated reduction cuts approximately 1.5 events/day survive the eye-scanning stage as good upmu events.

The eye-scanners look at event displays of each event and use the quality of the fits (from `muboy` and `precisefit`), the timing and charge information and the OD cluster information

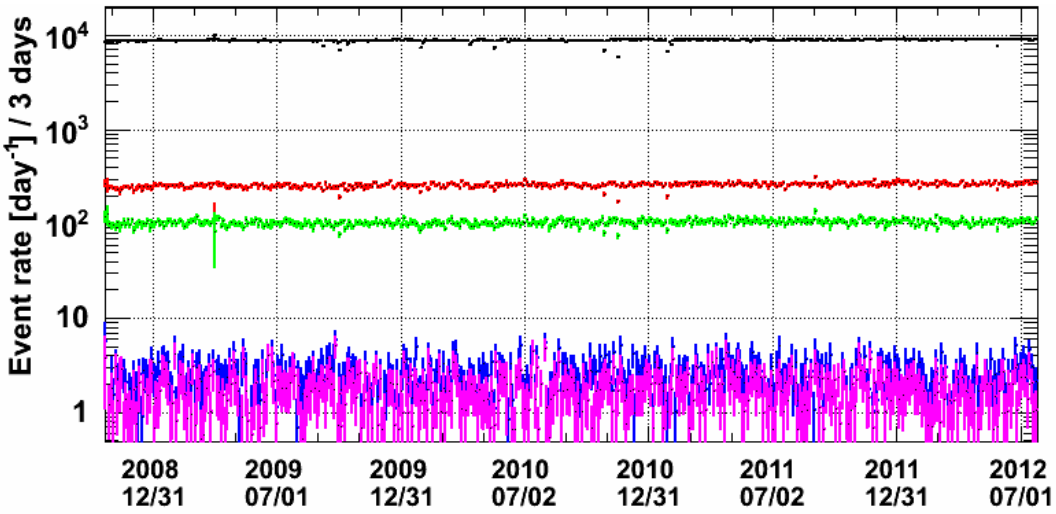

Figure 5.19: The event rate output of `umred1st` (black), `umred2nd` (red), `precisefit` (green), `umred3rd` (blue) and `umred4th` (magenta) for SK-IV from the automated upmu reduction software.

to save good upmus and reject backgrounds. The charge deposited on the PMTs can be color-coded by quantity (charge mode) or by time of signal (timing mode). The latter is useful in reconstructing the direction of events for which the fit is ambiguous. The eye scanner can also choose to apply a manual fit to the event, and if the direction from this manual fit differs from the computer's fit by at least 5° then the event is rejected, and by less than 5° the event is saved (even in the case of slightly downward-going events; this will be rejected by the final official event cut which requires an upward-going muon).

5.3.8 Background Subtraction

The upmu reduction process combined with eye-scanning produces a data set which is mostly free from backgrounds. The signals of high-energy upward-going muons in SK are mostly well-fit by the fitters mentioned previously and easily verified by their OD clustering, charge and timing information. The only significant background sources for upmu events are cosmic ray muons which up-scatter just before entering the detector. These events produce a muon-like track which is upward going and can easily be accidentally included in the final

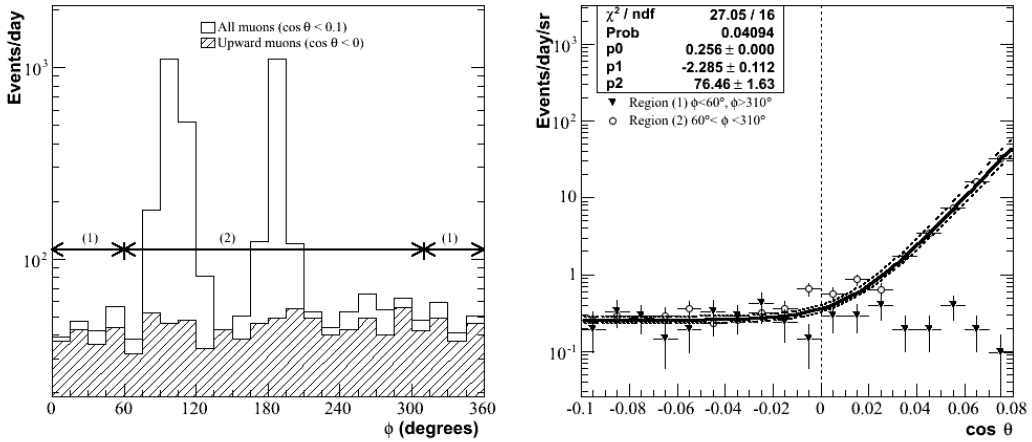

Figure 5.20: The background subtraction method for near-horizontal upward-going muons, shown for SK-IV through-going muons. The LHS shows the azimuthal distribution of events summed over all zenith angles, and the RHS shows the zenith angle distribution of events with the BG fit function overlaid.

data set.

The SK detector is located under an overburden of 2,7000 m.w.e. which greatly reduces the cosmic ray background. However, the rock surrounding the detector is not uniformly thick in all azimuthal directions. There are thin regions of rock which allow more cosmic ray muons to enter than others. A map showing through-going muon data as a function of azimuthal angle integrated over all zenith angles is shown in Fig. 5.20. The background is estimated by fitting the three parameters $p0$, $p1$ and $p2$ as a function of the cosine of the zenith angle with the dependence

$$f[\cos(\theta)] = p0 + e^{p1+p2\cos(\theta)}. \tag{5.6}$$

The parameter $p0$ is first quantified as the average event rate per day per steradian from region 1, which does not contain either of the thin regions. The number of events in the thin regions of the rock, which can clearly be seen as the places where the number of through-going muons spikes within region 2, is then fit with this function and fixed $p0$ to determine $p1$ and $p2$. The best-fit parameters after the fit to region 2 are then used to estimate the number of BG events entering the two most-horizontal bins by integrating over

the relevant zenith angles:

$$N_{BG} = \int_{\cos\theta_x}^{0} e^{p1+p2\cos(\theta)} d\cos(\theta) \tag{5.7}$$

The RHS of Fig. 5.20 shows the zenith-angle distribution of through-going muons in SK-IV with the result of the fit function overlaid. The number of BG events estimated in each of the two most horizontal bins is taken from this fit and subtracted from the actual datasets before their use in analyses. The uncertainty of the BG subtraction is estimated by the 1σ deviations in the fitted curve itself, as shown by the dashed lines surrounding the fit.

Chapter 6

EVENT RECONSTRUCTION

As part of the reduction processes described in the previous chapter, events undergo reconstruction which converts their PMT timing and charge information into kinematics variables suitable for physics analyses. The reconstruction processes are identical for data and MC samples. The information which the reconstruction calculates includes vertex fitting, ring finding an counting, particle identification, direction and momentum reconstruction among others. The analyses described in this work eventually bin all events according to their direction (cosine of the zenith angle), their e-like or μ-like nature, and their lepton momentum. The reconstruction methods described below mainly apply to the contained events in the data sample. The PC and Upmu events are all treated as single-ring μ-like events so some, but not all, of the following methods apply to their reconstruction. The following are the main steps in the reconstruction process (for a more detailed description, please refer to [108].

6.1 Vertex Fitting

The reconstruction begins by vertex fitting, which is done in three steps.

6.1.1 Point Source Fit

The first step in vertex fitting is simple and assumes a single point source for all ID photons. The time of flight is then subtracted for all photons detected at the PMTs according to their relative position to the assumed point source. After this subtraction a distribution of PMT hit residual times is constructed. The vertex is then estimated to be the point at which a maximal goodness-of-fit is achieved assuming a Gaussian distribution of the form

$$G_P = \frac{1}{N}\sum_i \exp\left(-\frac{(t_i - t_0)^2}{2(1.5\times\sigma)^2}\right) \tag{6.1}$$

where N is the total number of PMTs registering hits, i is the i-th hit PMT, t_i is the residual time, t_0 is a free parameter chosen to maximize G_P and σ is the PMT timing resolution which is taken to be a constant 2.5 nsec. The point which returns the maximum value of G_P is taken to be the vertex. The particle direction $\vec{d_o}$ is then estimated by taking a charge-weighted vector sum over all hit PMTs, with the form:

$$\vec{d_0} = \sum_i q_i \times \frac{\vec{P_i} - \vec{O_0}}{|\vec{P_i} - \vec{O_0}|} \tag{6.2}$$

Here $\vec{O_0}$ is the vertex position found by the above method, $\vec{P_i}$ is the vector from that point to the i-th PMT, and q_i is the charge on each PMT.

6.1.2 Ring Edge Search

Assuming the point-fit vertex position the edge of the brightest ring in the Cerenkov cone is measured next. The angle between the axis of the particle's direction and the edge of the Cerenkov cone is taken to be the opening angle. The edge of the ring is determined by an estimator, which is a function of opening angle, given by

$$Q(\theta_{\rm edge}) = \frac{\int_0^{\theta_{\rm edge}} PE(\theta) d\theta}{\sin\theta_{\rm edge}} \times \left(\frac{dPE(\theta)}{d\theta}\right)^2 \times \exp\left(-\frac{(\theta_{edge} - \theta_{exp})^2}{2\sigma_\theta^2}\right) \tag{6.3}$$

where $PE(\theta)$ is the angular distribution of the observed charge as a function of the opening angle θ, θ_{edge} is the opening angle at the current tested ring edge, θ_{exp} is the expected opening angle from the charge in the cone and σ_θ is the angle's resolution. The observed charge in this calculation is corrected for PMT angular acceptance, attenuation length and scattering. The ring edge position θ_{edge} is required to be greater than the angle at which the most charge is deposited ($\theta_{\rm peak}$ and the second derivative of the corrected charge distribution with respect to angle is required to vanish. The corrected charge distribution $PE(\theta)$ and its second derivative are shown for a typical event in Fig. 6.1.

The estimator in 6.3 is calculated while varying the both the particle direction $\vec{d_o}$ found in 6.2 and the opening angle. The pair which maximize the estimator are used to determine the ring edge.

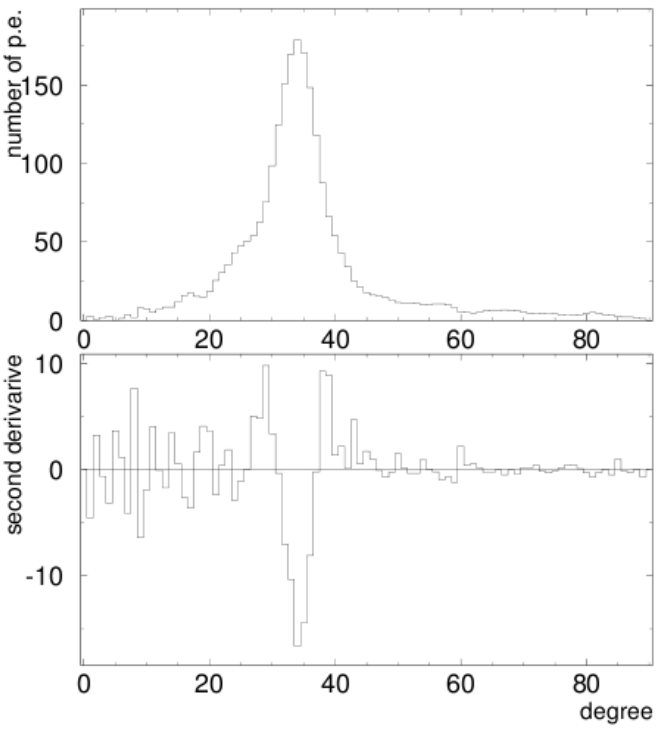

Figure 6.1: Typical angular distribution of the observed, corrected charge in number of p.e. (top) and its second derivative with respect to angle (bottom), which are used in the ring edge search algorithm. Taken from [108].

6.1.3 Precise Vertex Fit

After locating the edge of the Cerenkov ring a more precise vertex fitter called `TDC-fit` is applied. Casting away the previous point-source vertex assumption, this fitter now takes into account the track length of the charged lepton and also scattering effects for the photons emitted. The fact that photons are now generated along the length of the track is reflected in the definition of the PMT timing residuals, defined as:

$$t_i = t_i^0 - \frac{1}{c} \times |\vec{X}_i - \vec{O}| - \frac{n}{c} \times |\vec{P}_i - \vec{X}_i|, \text{ for PMTs inside Cerenkov ring}$$
$$t_i = t_i^0 - \frac{n}{c} \times |\vec{P}_i - \vec{O}|, \text{ for PMTs outside Cerenkov ring}$$

Here i is the PMT index, $\vec{O}$ is the vertex position, $\vec{X}_i$ is emission point along the track for photons reaching PMT i, n is the refractive index of water, and $\vec{P}_i$ and t_i describe the position and hit timing of the i-th PMT.

The goodness-of-fit is now calculated in separate ways for PMTs inside and outside of the Cerenkov ring. For those inside the ring the goodness-of-fit has the same form as 6.1. For PMTs outside the main ring a modified goodness is calculated which includes scattering effects for those hits which occur later than t_0 (for details please see [108]. The final goodness-of-fit is estimated by combining the in-ring and out-ring parameters and the vertex which maximizes this is chosen. The vertex position from this calculation is used for events which will be found to have multiple rings. A distribution of the difference between true and reconstructed vertex position for one such sample, the SK-IV FC multi-GeV multi-ring μ-like sample, is shown in Fig. 6.2. The resolution for this sample is found to be 87.8 cm. Resolutions for older samples are detailed in [108] and in all cases are found to be near 100 cm or less.

6.2 Ring Counting

After determining the vertex and the main Cherenkov ring, a search for other ring candidates based on the Hough transformation method[15] is performed. A schematic showing the basic principle of this method is shown in Fig. 6.3. This image depicts hit PMTs and their proposed Cherenkov ring viewed from a plane perpendicular to the ring's plane. The hit

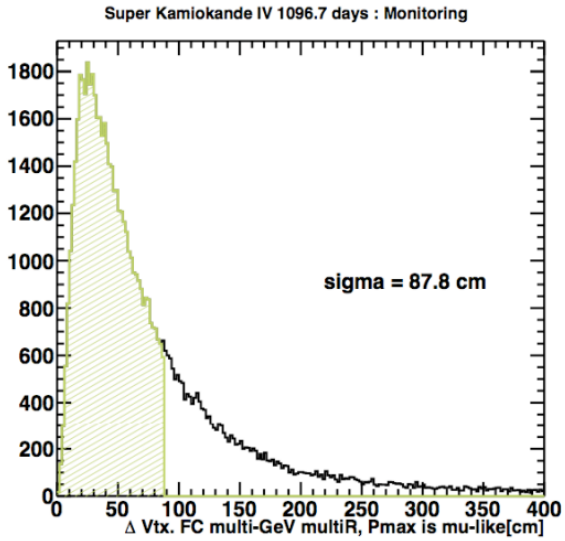

Figure 6.2: Difference between true and reconstructed vertices for SK-IV FC multi-GeV multi-ring MC. The shaded region covers 68% of all events. Taken from [92].

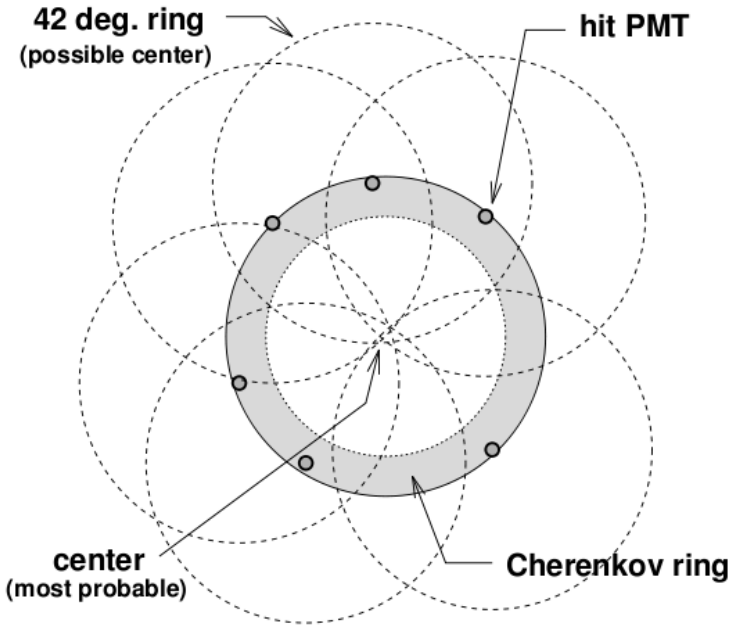

Figure 6.3: The Hough transformation method for finding Cerenkov rings. Ring candidates are guessed by drawing circles with 42° opening angles surrounding all hit PMTs and intersection points are assumed to be the center of the ring.

PMTs are surrounded by dashed circles, which are ring candidates with opening angles of 42° centered on each hit PMT. The intersection point of many of these candidate rings is taken to be the center of the final proposed Cherenkov ring. In practice the expected distribution of charge around hit PMTs is not a circle with a fixed radius, so instead a more complicated charge distribution function f(θ) is drawn on a spherical coordinates plane (Φ, Θ) for each hit PMT. The distributions from all initial candidate rings overlap so that peaks of charge, rather than intersecting lines, represent likely true ring centers.

The hypothesis of the existence of rings is quantitatively tested with a Likelihood method. Given N rings previously found, the likelihood for the N+1-th ring is defined by:

$$L_{N+1} = \sum_i \log\left(\text{prob}\left(q_i^{obs}, \sum_{n=1}^{N+1} \alpha_n \times q_{i,n}^{exp}\right)\right) \tag{6.4}$$

where the hits from all N+1 PMTs are included in the sum. In this expression q_i^{obs} and q_i^{exp} are the observed and expected charge in the i-th PMT and the index n represents the ring index, so that the sum inside the probability function represents the sum of charges expected on each PMT from each contributing ring candidate. The coefficients α_n are varied so that the expression is maximized. The probability function is described by the convulotion of the single-p.e. response and a Poisson distribution for low charge ($q^exp < 20$ p.e.) and a Gaussian distribution at higher charge.

If this algorithm finds a valid second ring, then it will continue searching for a third ring, and so on, until it reaches a maximum of five rings. $N + 1$ ring candidates where $L^{N+1} \geq L^N$ are considered and if they pass quality cuts based on the p.e. distributions under both assumptions then they are kept. Efficiencies for ring-counting with this method are generally found to be above 90% for almost all relevant event samples. Differences between data and MC are taken as sources of systematic uncertainty in the event selection for analyses. Plots showing the ring-counting seperation for single-ring and multi-ring FC events for data and MC are shown in 6.5

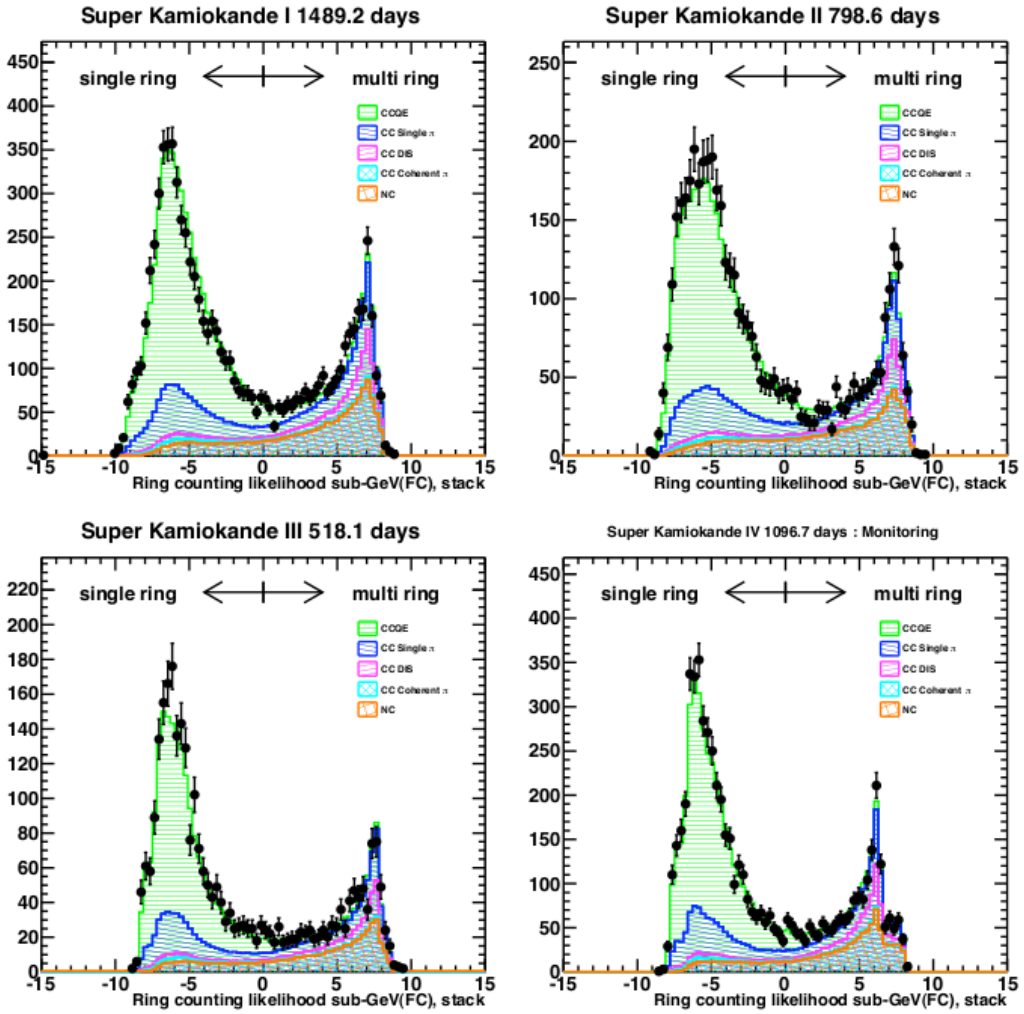

Figure 6.4: Ring-counting separation for sub-GeV events for SK-I,-II,-III and -IV. Data are in black and oscillated MC ($\sin^2(2\theta_{23})$=1.0,Δm^2_{23}=2.5×10^{-3}) are the colored histograms.

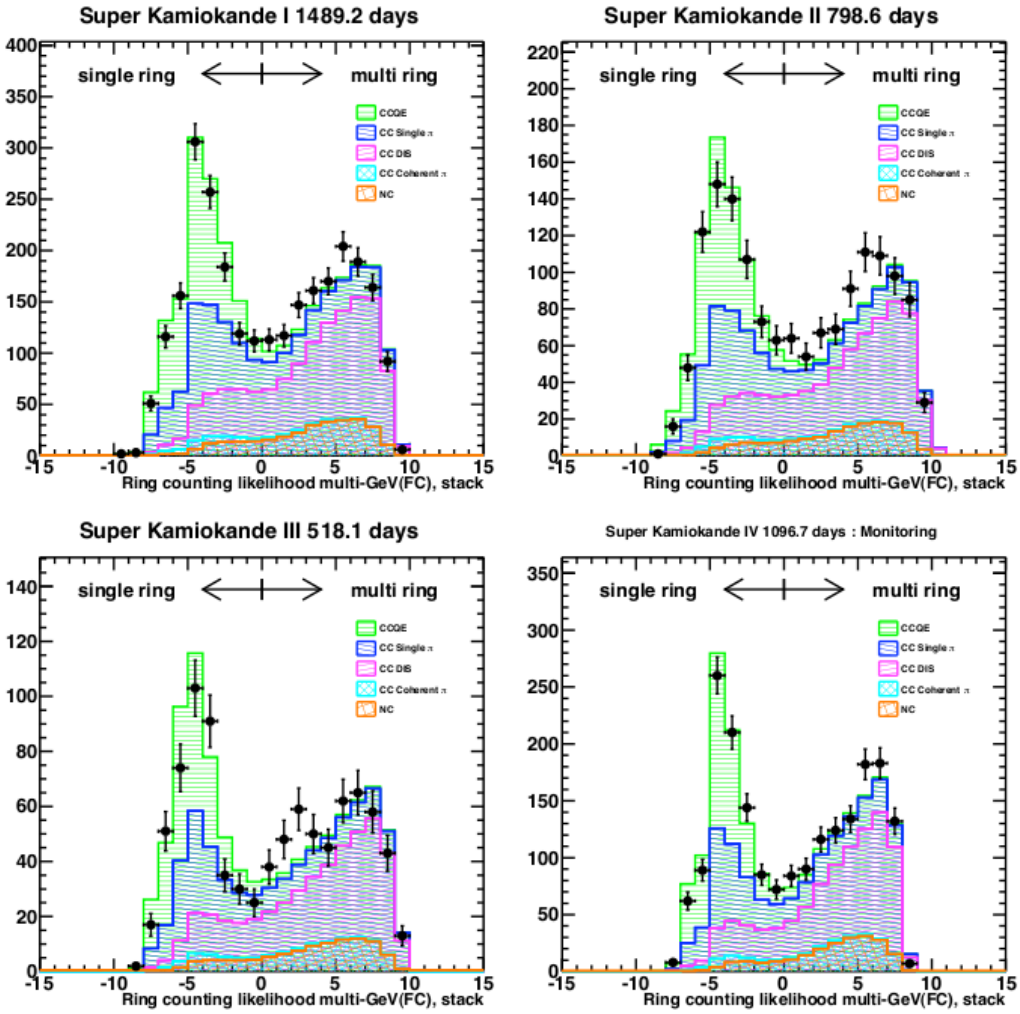

Figure 6.5: Ring-counting separation for multi-GeV events for SK-I,-II,-III and -IV. Data are in black and oscillated MC ($\sin^2(2\theta_{23})$=1.0,Δm^2_{23}=2.5×10^{-3}) are the colored histograms.

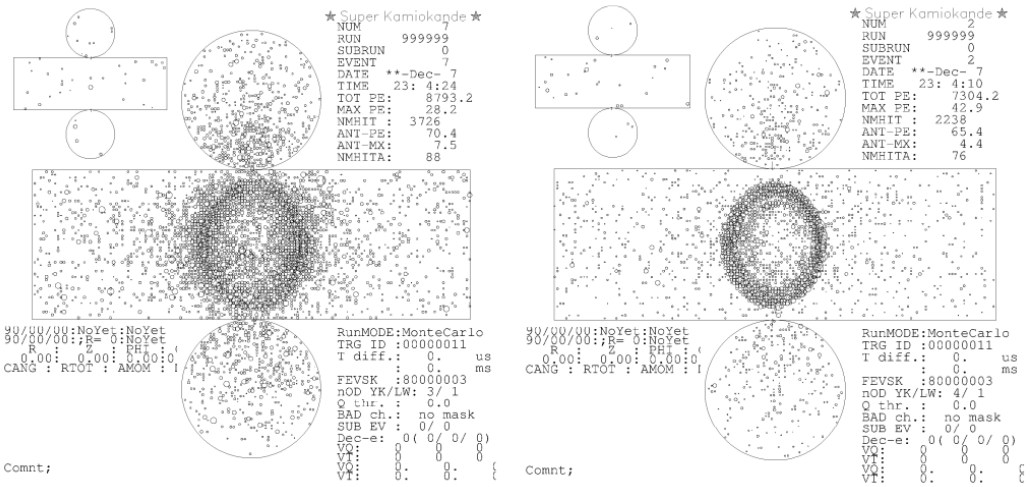

Figure 6.6: Event displays for typical (1 GeV) e-like (left) and μ-like (right) MC events.

6.2.1 Particle Identification

A particle identification algorithm called PID is next applied to classify the rings as showering (e-like) or non-showering (μ-like). Showering rings can be produced by electrons as well as γ-rays, which have diffuse, "fuzzy" ring edges due to electromagnetic shower production and electron multiple scattering effects. This is because electrons are likely to scatter multiple times along their track and also emit hard photons upon scattering, which may cause pair-production and further electron scattering. Non-showering rings are produced by more massive particles such as muons and pions and have a very distinct, sharp ring edge. Event displays of e-like and μ-like rings of 1 GeV monte carlo events for comparison are shown in Fig. 6.6.

The PID algorithm first calculates the expected number of p.e.s in each PMT from either an electron or muon. In the electron case, a MC simulation of test events with various momenta is generated with a test vertex at a distance 16.9 m from the wall. These momenta distributions are used in the calculation of the expected light distribution for e-like events. The expected number of p.e.s in this calculation accounts for scattering, PMT angular acceptance, light attenuation and geometric factors such as distance dependence of the

light intensity. For the muon case the expected light distribution is calculated analytically using muon energy loss and Cherenkov radiation models. This calculation includes effects from knock-on electrons as well as the decrease in the Cherenkov opening angle as the muon loses energy (note that this effect is not included in the electron simulation, where is is assumed electrons are always highly-relativistic and thus have opening angles of 42°.

A likelihood function is then calculated from the expected charge distributions of both e-like and μ-like assumptions for each ring in an event. From this likelihood function a probability function is calculated, and the overall PID probability distribution is defined as

$$P_{PID} = \sqrt{-\log P_\mu} - \sqrt{-\log P_e}. \tag{6.5}$$

This function is defined so that $P_{PID} < 0$ is e-like and $P_{PID} \geq 0$ is μ-like. Distributions for this likelihood variable for SK-I,-II,-III and -IV data and MC are shown in Fig. 6.7 for a single-ring sample and 6.8 for a multi-ring sample. The separation is generally better for single-ring events.

6.3 Precise Vertex Fitting

A more precise vertex fitter is applied next. The previously-mentioned fitter, `TDC-fit` used only the PMT timing information. This results in a marginal performance for μ-like events which have longer tracks because the point-source emission assumption for these events does not accurately reflect time-of-flight corrections. This precise fitter, called `MS-fit`, also incorporates the PID and Cherenkov opening angle information. The proposed direction and vertex are varied while holding the Cherenkov ring angle fixed and the expected light pattern is compared to the observed pattern. The process is iterated until the goodness-of-fit along with the PID likelihood are both maximized. The fitter performs well and examples of the vertex and direction resolutions are shown in Figs. 6.9 and 6.10 for both e-like and μ-like events.

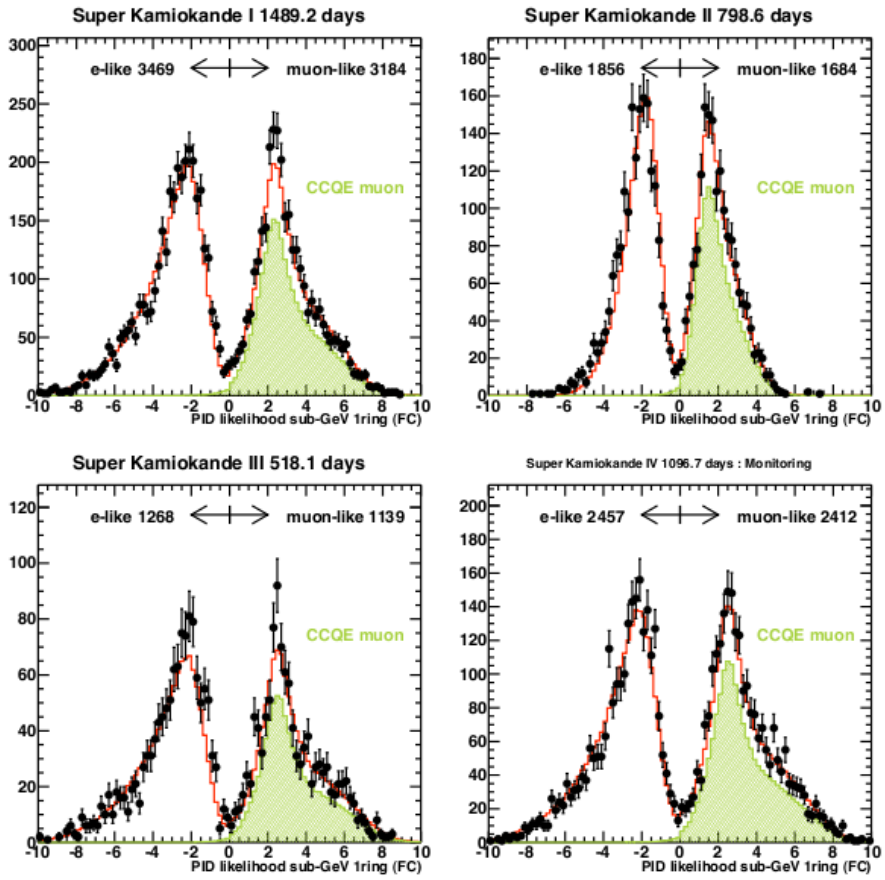

Figure 6.7: PID separation for SK-I,-II,-III and -IV FC sub-GeV single-ring samples of data (black) and MC (histograms).

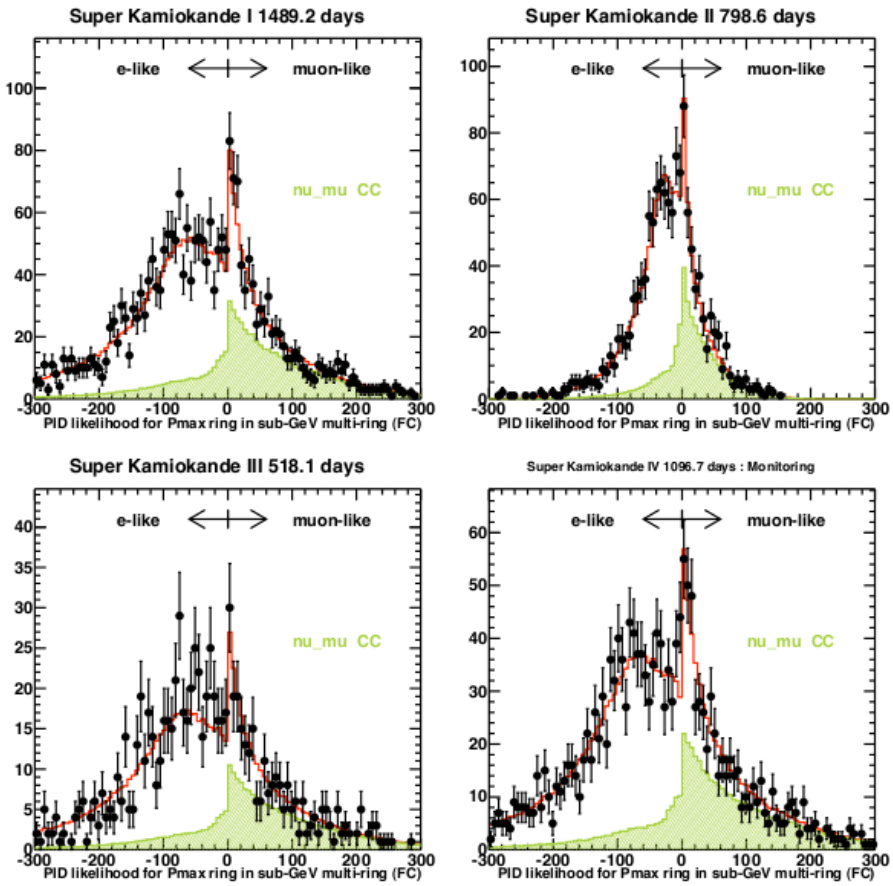

Figure 6.8: PID separation for SK-I,-II,-III and -IV FC sub-GeV multi-ring samples of data (black) and MC (histograms).

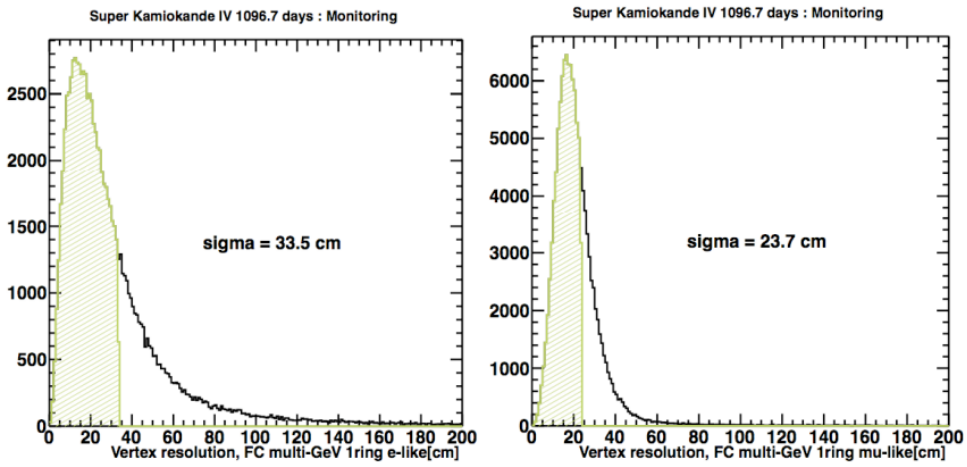

Figure 6.9: Distance between true and reconstructed vertex for SK-IV FC MC e-like (left) and μ-like (right) samples. Sigma (shaded region) represents 68% of the full area.

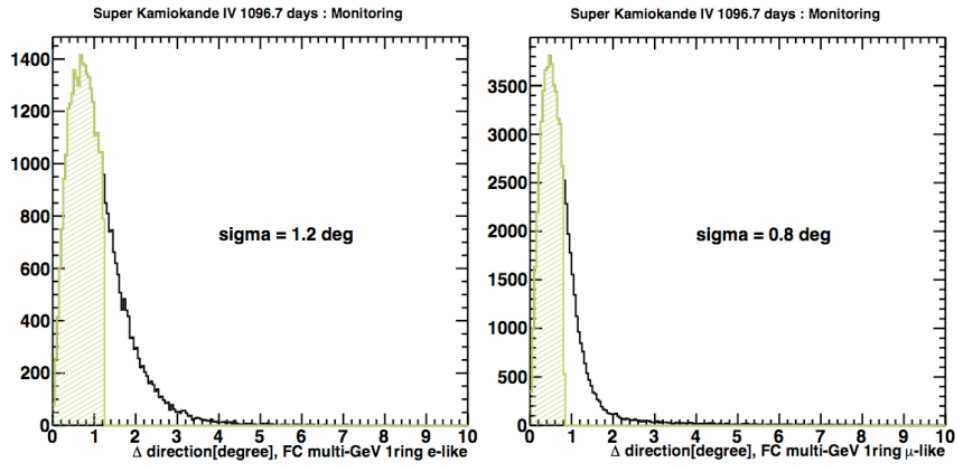

Figure 6.10: Angle between true and reconstructed direction for SK-IV FC MC e-like (left) and μ-like (right) samples. Sigma (shaded region) represents 68% of the full area.

6.4 Momentum Determination

Precise momenta are also assigned to events after ring-separation and particle identification have been performed. The momentum of each particle is estimated by the number of observed p.e.s found within a cone of half-angle 70° surrounding the reconstructed direction. The observed p.e.s are separated according to their contributions in each ring in order to find individual ring momenta. The total number of p.e.s is calculated after correcting for light attenuation, scattering, and PMT acceptance effects, and their sum is taken. The sum is restricted to the time window from 50 nsec prior until 250 nsec following the peak of the hit timing distribution after subtracting for time-of-flight. These limits exclude effects from muon decay electrons. The reconstructed momenta are estimated to have resolutions of 1.7 + $0.7/\sqrt{p\,\mathrm{GeV/c}}$% and 0.6 + $2.6/\sqrt{p\,\mathrm{GeV/c}}$% for electrons and muons, respectively.

6.5 Reconstruction Improvements

Improvements were made to the reconstruction of events recently and these changes were incorporated into the datasets used in this analysis. A very brief summary of the changes will be described here. The `msfit` algorithm was updated after not having been changed for all of SK-I,-II and -III. The photon density table, which is used to estimate the number of corrected photons as a function of distance from the charged particle's track, was limited to distances of less than 15 m and angles of less than 90 degrees from the reconstructed vertex. This was improved to include distances up to 40 m and angles within 180 degrees. This improved the agreement between MC and data for corrected photons at large distances from the vertex. This resulted in significant improvements in reconstructed vertex resolutions. In particular, for Multi-GeV electrons, the 68% vertex resolution improved from 44.5 cm to 26.7 cm. Additionally, the `POLfit` program, which is used in reconstructing π^0 events which decay to two gammas and produce two e-like rings, was also improved recently. The `RNGSEP` algorithm, used in reconstruction and identification of rings, was not applied to the reconstruction of the two gammas in these events. Applying `RNGSEP` results in a better resolution of the reconstructed invariant π^0 mass peak. The effect is shown in Fig.6.11, where the old fitter is shown in blue and the improved fitter in red. The peak and resolution of the

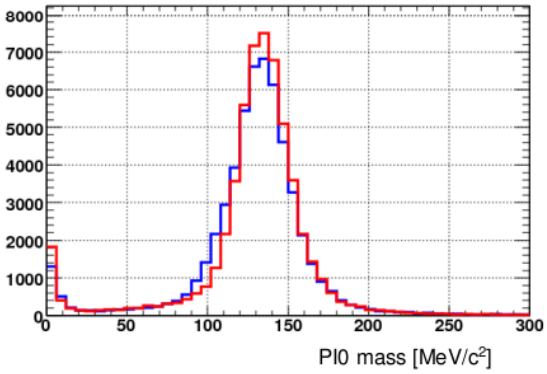

Figure 6.11: Improvement to the reconstructed invariant π^0 mass with an updated fitting algorithm shown in red compared to the original algorithm in blue.

π^0 mass were 134.9 and 15.7 MeV/c after the update, compared to 133.0 and 17.7 MeV/c before. This in turn improved the e/π^0 separation efficiency by reducing the number of π^0 backgrounds leaking into the ν_e samples while having no effect on the ν_e efficiency itself.

Chapter 7

TWO-FLAVOR OSCILLATION ANALYSIS

There are multiple atmospheric neutrino oscillation analyses that have recently been updated this year for the first time with the addition of the new SK-IV dataset onto the SK-I+II+III data. They can be divided into two main categories according to their binning schemes - zenith angle analyses and L/E analyses. The L/E analysis focuses on a smaller subset of the atmospheric neutrino data which has a well-defined L/E (for example, some of the FC and PC but no Upmu data are used). Details of this analysis can be found in [64]. Unlike the L/E analysis the zenith-angle analysis does not try to define a precise pathlength and energy to the neutrinos on an event-by-event basis. The L/E analysis is designed to produce a better constraint on the mass-squared splitting, while it is found that the zenith-angle analysis produces a slightly more restrictive bound on the mixing angle.

The analysis which is the subject of this chapter is a zenith angle analysis which assumes two flavor oscillations of the channel $\nu_\mu \rightarrow \nu_\tau$. The oscillation probability for this channel is expressed as

$$P(\nu_\mu \rightarrow \nu_\tau) = \sin^2(2\theta_{23})\sin^2\left(\frac{1.27\Delta m^2_{23}L}{E_\nu}\right) \tag{7.1}$$

where Δm^2 is in units of eV^2, L units of km, and E units of GeV. This analysis is therefore a ν_μ disappearance search as the majority of the ν_τs do not reach the energy threshold of 3.4 GeV necessary for a tau particle to be produced in a weak charge-current interaction. The two parameters which are constrained by this analysis are the mass-squared splitting Δm^2_{23} and the mixing angle θ_{23}. SK first published evidence pointing to ν_μ disappearance consistent with oscillations in 1998[66] and then published an updated zenith-angle analysis with the full SK-I dataset in 2005[65]. This analysis constrained the mass-squared splitting to $1.5 \times 10^{-3} < \Delta m^2 < 3.4 \times 10^{-3}$ eV^2 at 90% C.L. and the mixing angle to $\sin^2 2\theta > 0.92$.

Enhanced analyses searching for sub-leading effects from θ_{13} [57] and differences in oscillations between neutrinos and anti-neutrinos[37] using the same zenith-angle binning and

the SK-I+II+III datasets have since been published. Additionally a full three-flavor analysis using the same dataset and binning scheme as this work has also been completed recently and is described in [92]. The search for differences in the signatures of normal hierarchy versus inverted hierarchy was the motivation for the update to the binning scheme that will be described in this chapter.

7.1 Analysis Space

The range of parameters tested in this zenith-angle analysis is motivated by the current constraints on the two atmospheric parameters by previous SK analyses and other experiments such as K2K and MINOS[34]. In particular, the most recent published result from the ν_μ disappearance analysis by MINOS[54] found $|\Delta m^2_{23}| = 2.32^{+0.12}_{-0.08} \times 10^{-3}$ eV^2 and $\sin^2 2\theta_{23} > 0.90$ at 90% C.L. In the present analysis we use the parameter ranges $0.001 < \Delta m^2_{23} < 0.01$ eV^2 and $0.7 < \sin^2 2\theta_{23} < 1.2$. A grid is defined in which each unique pair of (Δm^2_{23},$\sin^2 2\theta_{23}$) is assumed and fit against the data. There were 81 values of Δm^2_{23} tested and they were distributed on a log scale, while 71 values of the mixing angle were tested on a linear scale resulting in a total of 5,751 grid points tested.

7.2 Analysis Binning

The data and MC are binned according to their zenith angle direction and event classification based on the information from the reduction and reconstruction methods described in previous chapters. The binning scheme has been updated from previous SK zenith angle analyses. The number of bins has been increased from 420 to 480. Figure 7.1 is a schematic showing all the bins in the new binning scheme. The vertical axis represents increasing momentum with increasing height. All samples, except for the shaded ones in figure, are separated into 10 zenith-angle bins for each momentum bin. The binning is chosen such that there at least five expected MC events in each bin after scaling to data livetime. This guarantees the χ^2 function, which will be introduced later in this chapter, can be properly applied in this analysis.

The additional 60 bins come from a new event classification scheme in the FC multi-GeV single-ring and multi-ring samples. These events are now binned according to their

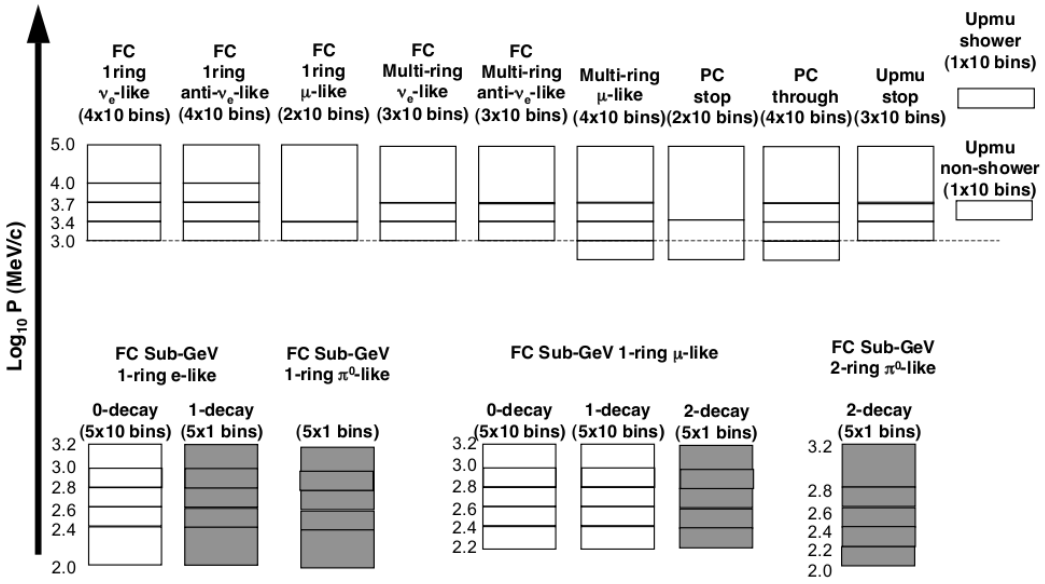

Figure 7.1: The layout of bins used in the zenith-angle analyses. There are 370 for FC, 60 for PC, and 50 for Upmu events, giving 480 in total. White boxes indicate those for which 10 zenith bins are defined and shaded indicates single zenith-angle bins.

ν_e-like and $\bar{\nu}_e$-like characteristics. Though SK cannot distinguish events as being induced by neutrinos or anti-neutrinos on an event-by-event basis, there are certain characteristics of the FC multi-GeV sample that allow it to be separated with reasonable purity. This binning scheme is motivated by the full three-flavor analysis which seeks to improve sensitivity to the neutrino mass hierarchy[92]. An enhancement of electron neutrino appearance from the matter effect occurs for neutrinos in the normal hierarchy and ant-neutrinos in the inverted hierarchy. The multi-GeV ν_e-like and $\bar{\nu}_e$-like event separation criteria are as follows. For single-ring events, a simple separation where all events with 0 decay electrons are considered $\bar{\nu}_e$-like and events with 1 or more decay electrons are considered ν_e-like is used. The CC interactions of ν_e occur as:

$$\nu_e + N \rightarrow e^- + N' + \pi^+$$
$$\pi^+ \rightarrow \mu^+ + \nu_\mu$$

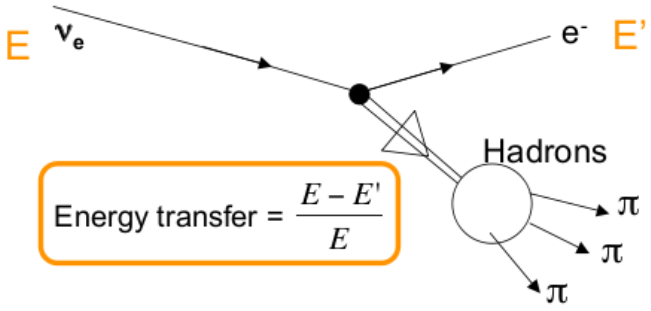

Figure 7.2: A typical CCν_e interaction which produces an e-like multi-ring event in SK.

The μ^+ from the pion decay then decays via $\mu^+ \rightarrow e^+ + \nu_e + \bar{\nu_\mu}$ and the e^+ can be detected as a decay electron. The splitting of these samples generates reasonable purities of 62.8% and 36.7%[92] when tested with SK-IV MC. For multi-ring events, a more complicated selection using a likelihood function is applied. A typical interaction producing a multi-ring event is shown in Fig. 7.2. For these interactions the energy transfer is typically larger for CCν_e than it is for CC$\bar{\nu_e}$ and as a consequence, the following facts can be used in constructing a likelihood function to separate the sample:

1. CCν_e events have a smaller momentum fraction for the most energetic ring
2. CCν_e events have a greater number of Cherenkov rings (from more outgoing pions)
3. CCν_e events have larger transverse momentum
4. CCν_e events have more decay electrons

The likelihood separation is found to produce ν_e-like and $\bar{\nu}_e$-like samples with 59.4% and 21.0% purities, which are modest values but are increases of a few percent above the original purities found in the non-separated sample[92].

The two flavor analysis assumes no oscillations involving electron-flavor neutrinos and anti-neutrinos, so there is no matter effect or sensitivity to the hierarchies in this work. However, the analyses are otherwise similar (they both use the same dataset, MC, zenith-angle binning and chi-squared statistic) and we use the same binning scheme here for consistency. The effect of splitting the bins is at most very small and would only come from muon-flavor

impurities (which can undergo oscillations) in the FC multi-GeV.

7.3 Monte Carlo

The monte carlo samples used in this work are 500-year samples of the FC, PC and tau, and 200-years of upmu event simulation. The MC samples used here have been newly regenerated from previous MC samples and have not been used in official analyses until now. They are produced with the Honda 2011 flux model[49] as well as the other modifications made to `NEUT`, `skdetsim`, and event reconstruction described previously. Oscillations are not applied to the MC during initial production. The monte carlo events are each individually binned according to their zenith angle, momentum and event classification, and after this binning each event is reweighted by the oscillation probability calculated from the energy and pathlength (which is determined from the true zenith angle direction) truth information.

The pathlength calculation also includes an averaging estimation of the neutrino production height in the atmosphere. For each event 20 oscillation probabilities from a sample of production heights are calculated and the average of these is taken as the final oscillation weight. The events are also reweighted to account for the solar wind's modulation of neutrino fluxes. Primary cosmic ray flux is at a minimum (maximum) when the solar wind is most (least) active and this affects the production of atmospheric neutrinos. After binning the weighted MC each combination of oscillation parameters is tested in this analysis so that for every pair of parameters, a uniquely weighted set of monte carlo including all event samples is binned with all the data and compared.

7.4 Dataset

The datasets used in this analysis include SK-I,-II,-III, and -IV. Up to and including the SK-III phase, the livetimes for the FC and PC data were not equal to that of the Upmu data. The FC and PC data are much lower energies than the Upmu data and so are more susceptible to problems in the detector. In SK-IV (and thereafter) the livetimes for all three samples are equal. Table 7.4 shows the livetimes for all datasets used in this analysis. The number of data and oscillation-weighted,livetime-normalized MC events in each event sample is listed in table 7.4.1.

Data sample	SK-I(days)	SK-II(days)	SK-III(days)	SK-IV(days)
FC	1489.2	798.6	518.1	1096.66
PC	1489.2	798.6	518.1	1096.66
Upmu	1645.9	827.7	635.6	1096.66

Table 7.1: A summary of the livetimes (units of days) for the data used in this analysis.

7.4.1 Event Categories

The official event categories for the analysis dataset were as follows. FC events were divided into Sub-GeV (visible energy < 1.33 GeV) and Multi-GeV (visible energy > 1.33 GeV). They were also subdivided according to various combinations of their ring PID (e-like, μ-like or π^0-like), the number of rings found (single or multi), the number of decay electrons, and their ν_e-like or $\bar{\nu}_e$-like probability. PC events were divided into stopping and through-going. PC stopping events were put into two momentum bins, while PC through-going were put into four momentum bins. The upmu sample was divided into stopping (3 momentum bins), through non-showering and showering (no momentum binning for through-going events). In most cases there 10 zenith divisions used, with FC and PC events binned into the range $-1.0 < \cos\theta_z < 1.0$ and upmu events in the range $-1.0 < \cos\theta_z < 0.0$. The samples which were put into one large zenith bin are shown as the shaded bins in Fig. 7.1.

7.4.2 Two-Flavor Oscillation Effects

The two-flavor oscillation channel $\nu_\mu \rightarrow \nu_\tau$ exhibits muon-type neutrino disappearnce and assumes no ν_e appearance. Assuming only mixing between the ν_μ and ν_τ implies that the μ-like samples will undergo oscillations while the e-like samples should be largely unaffected. A 2-dimensional plot of the predicted oscillation effects as a function of neutrino energy and pathlength assuming the SK-I+II+III best-fit values is shown in Fig. 7.3.

	SK-I		SK-II		SK-III		SK-IV	
	Data	MC	Data	MC	Data	MC	Data	MC
FC Sub-GeV								
1-ring e-like								
0-decay e	2992	2705.4	1573	1445.4	1092	945.3	2098	1934.9
1-decay e	301	248.1	172	138.9	118	85.3	243	198.4
π^0-like	176	160.0	111	96.3	58	53.8	116	96.2
μ-like								
0-decay e	1025	893.7	561	501.9	336	311.8	405	366.3
1-decay e	2012	1883.0	1037	1006.7	742	664.1	1833	1654.1
2-decay e	147	130.4	86	71.3	61	46.6	174	132.2
2-ring π^0-like	524	492.8	266	259.8	182	172.2	380	355.9
FC multi-GeV								
1-ring								
ν_e-like	191	152.8	79	78.4	68	54.9	156	135.9
$\bar{\nu_e}$-like	665	656.2	317	349.5	206	231.6	423	432.8
μ-like	712	775.3	400	415.7	238	266.4	420	554.8
multi-ring								
ν_e-like	216	224.7	143	121.9	65	81.8	175	161.9
$\bar{\nu_e}$-like	227	219.7	134	121.1	80	72.4	212	179.1
μ-like	603	640.1	337	337.0	228	231.4	479	499.0
PC								
Stop	143	141.4	77	71.3	54	52.0	109	115.0
Thru	759	772.4	350	377.3	290	304.0	626	629.9
Upmu								
Stop	429	425.5	210	211.6	193	166.3	284	276.4
Non-showering	1564	1340.1	725.3	689.6	612.9	497.8	1048	863.1
Showering	271.6	294.7	108.1	109.2	110	127.7	282.9	217.0

Table 7.2: A summary of the data and MC samples (with their oscillation weights applied) used in this analysis. The MC samples are normalized to the data livetimes.

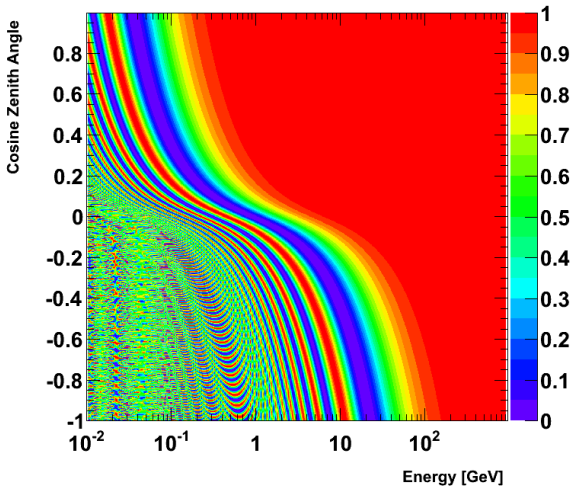

Figure 7.3: Contours of the probability of ν_μ survival as a function of pathlength and energy assuming two-flavor oscillations with ($\Delta m^2_{23} = 2.11 \times 10^{-3}$ eV^2, $\sin^2(2\theta_{23}) = 1.00$). Red areas indicate no oscillations and green areas indicate maximum oscillations.

7.5 Chi-Squared Analysis

The likelihood used in this analysis is based on Poisson statistics in order to reflect the fine binning. The Poisson distribution for the number of expected events E given a number of observed events $\mathcal{O}$ is given by

$$P(E, \mathcal{O}) = \frac{E^{\mathcal{O}}}{\mathcal{O}!} e^{-E}. \tag{7.2}$$

There is in general an expected contribution of 1 unit from each bin to the reduced χ^2 in the case where a small number (~ 1) events are expected in each bin. Assuming N total bins with index n a likelihood of the form is constructed:

$$\mathcal{L}(E, \mathcal{O}) = \prod_n \frac{E_n^{\mathcal{O}}}{\mathcal{O}_n!} e^{-E_n}. \tag{7.3}$$

Taking the log likelihood ratio of this expression (the ratio of the quantities expected given observed and observed given observed) the expression becomes

$$\chi^2 \equiv -2\ln\frac{\mathcal{L}(E, \mathcal{O})}{\mathcal{L}(\mathcal{O}, \mathcal{O})} = 2\sum_n (E_n - \mathcal{O}_n + \mathcal{O}_n \ln\frac{\mathcal{O}_n}{E_n}) \tag{7.4}$$

To incorporate the effects of independent systematics into the analysis, the so-called "pull" method for the χ^2 minimization is used[75]. This is equivalent to introducing a shift in the

number of expected events in each bin that is linearly proportional to a systematic error parameter. Mathematically we have

$$E_n \rightarrow E_n(1 + \sum_i f_n^i \epsilon_i) \tag{7.5}$$

where ϵ_i is the parameter for systematic error i and f_n^i is the fractional change (which is dependent upon individual bin contents and calculated with the MC ahead of time assuming the best-fit oscillations from [65]; For more details see [111]) that ϵ_i effects on the number of expected events. For each bin the effects of all systematic errors are summed (hence the sum over i) while allowing the ϵ_i parameters to vary. The ϵ_i parameters are varied so that the χ^2 is minimized during the fit and the distribution of ϵ_i/σ_i, where σ_i is the expected 1-σ variation of each systematic uncertainty, is expected to be Gaussian. A penalty term is added to Eq. 7.4 to constrain the size of the effect that the systematic error parameters have on the fit, so that the final χ^2 statistic takes the form:

$$\chi^2 = 2\sum_n (E_n - \mathcal{O}_n + \mathcal{O}_n \ln\frac{\mathcal{O}_n}{E_n}) + \sum_i \left(\frac{\epsilon_i}{o_i}\right)^2 \tag{7.6}$$

$$\chi^2 = 2\sum_n \left(E_n \rightarrow E_n(1 + \sum_i f_n^i \epsilon_i) - \mathcal{O}_n + \mathcal{O}_n \ln\frac{\mathcal{O}_n}{E_n \rightarrow E_n(1 + \sum_i f_n^i \epsilon_i)}\right) + \sum_i \left(\frac{\epsilon_i}{o_i}\right)^2 \tag{7.7}$$

With this equation in hand, the minimization of the χ^2 becomes equivalent to solving the equation $\frac{\partial\chi^2}{\epsilon_m} = 0$ for all m. This minimization is analogous to solving a system of linear equations, one for each systematic error parameter (for details see [65, 111]). After the minimization is done and the systematic error parameters are evaluated the data from the individual SK-I,-II,-III and -IV bins are merged together.

7.5.1 Systematic Error Terms

There are 150 ϵ_i systematic terms in total in this analysis, including terms common to all run periods (physics-related errors) and those unique for each run period (detector systematics). There are 19 terms each for neutrino flux uncertainties and neutrino interaction uncertainties, 68 related to event reduction (17 for each run period $\times$ 4 run periods) and 44

(11×4) related to event reconstruction and selection. The resulting pull values from the fit will be shown later in this chapter.

7.5.2 Neutrino Flux Errors

Absolute Normalization

The absolute normalization of the neutrino flux is based on the work of Honda et al[48] which is calibrated with atmospheric muon data. In that work they calculate an energy-depedent normalization uncertainty which is around 25% for low energies, decreases to to below 10% for energies between 1 and 10 GeV, and then increases again steadily for higher energies. A plot of this uncertainty is shown in 7.4. Two uncertainty terms for this enter the χ^2 minimization, one for E $<$ 1 GeV and one for E $>$ 1 GeV, and the energy dependence of these terms reflects the Honda calculation. The individual uncertainties of the pion production in hadronic interactions (δ_π), kaon production (δ_K), hadronic interaction cross-sections (δ_σ) and the density profile of the atmosphere ($\delta_{\rm air}$) entering the calculation are shown in the top plot in Fig. 7.4.

Flux Ratios

The value of the flavor ratio $(\nu_\mu + \bar{\nu_\mu})/(\nu_e + \bar{\nu_e})$ is known much better than the absolute normalization itself. The uncertainties used here are calculated from comparisons of the Honda[48], FLUKA[4] and Bartol[3] models. A plot of the ratios of these models to the Honda model is shown in Fig. 7.5. The uncertainty is estimated here to be 2% for E $<$ 1 GeV, 3% for 1 GeV $<$ E $<$ 10 GeV, 5% for 10 GeV $<$ E $<$ 30 GeV, and then increasing log-linearly in E up to 30% at 1 TeV. The convention here is that a positive value for the error parameter ϵ generates an increase the fraction of muon neutrinos. The ratio of neutrinos to anti-neutrinos $\nu_\mu/\bar{\nu_\mu}$ and $\nu_e/\bar{\nu_e}$ depends on the production ratios π^+/π^- and $\mathrm{K}^+/\mathrm{K}^-$ from the interactions in the flux calculations. This uncertainty is also estimated by comparing the flux models. The electron ratio is taken to be 5% below 10 GeV, 8% between 10 and 100 GeV, and a log-linearly increasing function which reaches 30% at 1 TeV. The muon ratio is smaller (2%) at low energies up to 1 GeV, 6% between 1 and 50 GeV, and then an

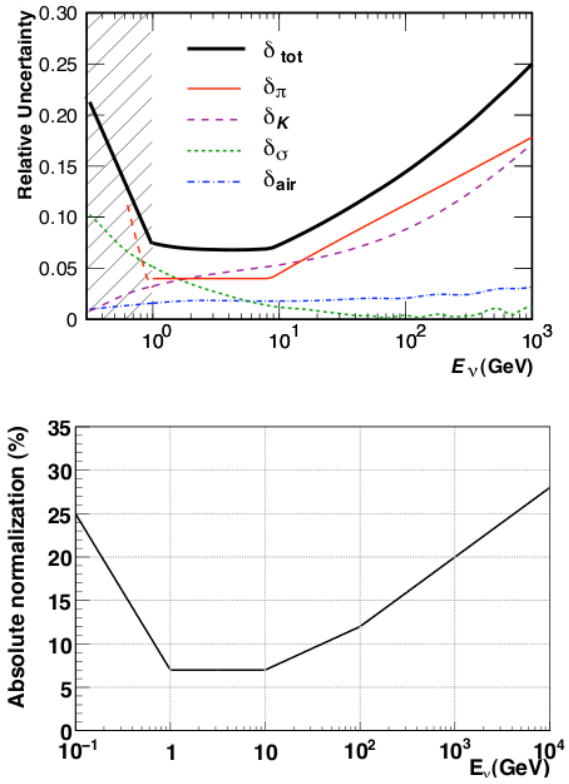

Figure 7.4: The components entering the absolute normalization uncertainty (top) and the overall uncertainty (bottom) as functions of energy[48].

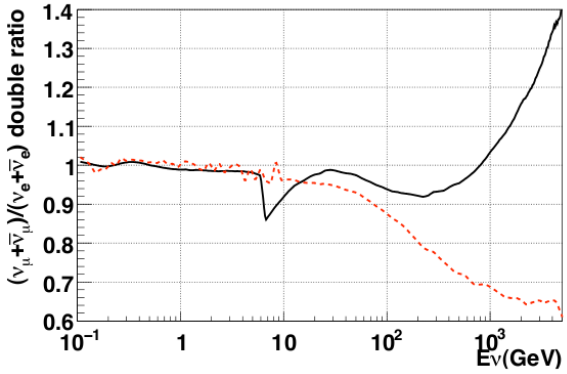

Figure 7.5: A plot of the ratios of the FLUKA[4] (dashed red) and Bartol[3] (solid black) flux models to the Honda[49] model.

increasing value reaching 60% at 1 TeV.

The up/down flux ratio also has an energy-dependent uncertainty from the geomagnetic field. For lower energies this uncertainty has less of an effect because the angular correlation of the charged lepton with the parent neutrino gets worse with decreasing energy. A comparison of the zenith angle distributions of the three flux models is used to estimate the uncertainty, which is taken to be 1%. The ratio of horizontal/vertical flux is also assigned at 1% uncertainty. The uncertainty comes from the differences of the 3-dimensional (or 1-dimensional) calculations of the flux in each of the models at lower energies, but is dominated by the production ratio of K/π at higher energies. This error is also estimated by comparing the zenith-angle distributions of the three flux models.

Production Ratios

Atmospheric neutrinos come primarily from pion decays at low energies. However at primary cosmic ray energies of a few tens of GeV and greater the component of K decay becomes increasingly large so the K/π ratio is taken as a systematic error. Recent measurements of the ratio[28] indicate an uncertainty of 3%. From these results and the dependence of neutrino energy on the hadron momentum the uncertainty in the K/π ratio is estimated to be 5% below 100 GeV and linearly increasing to 20% as a function of energy from 100 GeV to 1 TeV.

The ν production height is used in the calculation of the pathlength and this is a large percentage of the pathlength for downward and horizontal neutrinos, so a systematic error term is added for those events. The error is estimated by assuming a 10% variation in the density structure of the atmosphere (determined from comparisons of US-Standard '76 [98] and MSISE90[84]). The difference in the neutrino flux from path length variations in the different density structures is taken as the systematic error and its value is estimated to be 10%.

The primary cosmic ray energy spectrum is well modeled by the form $E^{-2.74}$ with a larger uncertainty for larger energies (i.e. above 100 GeV). Differences in the energy spectrum among the flux models considered are not sufficient to account for the different fluxes

calculated in the respective models, and so a sample-by-sample normalization error is applied to each of the FC, PC and Upmu samples to account for these differences. The error is set at 5% for each of the samples.

Solar flux activity is also taken into account when modifying the flux predictions in the monte carlo. The primary cosmic ray flux is modified on an 11-year cycle by the solar wind with an uncertainty of ± 1 year. This corresponds to errors on the solar activity term of 20%, 50%, 20% and 10% for SK-I,-II,-III and -IV, respectively.

Neutrino Interaction Systematics

Uncertainties in cross-sections and other terms related to the interactions are common across SK-I,-II,-III and -IV. The axial mass parameter, relevant for CCQE and single meson production interactions, is assumed to be 1.21 GeV in the MC production described in this work, with an uncertainty of 10%. The 10% comes from the difference in the spectra of squared-momentum transfer due to between this axial mass value and a value of 1.1 GeV from previous experimental measurements and used in previous SK analyses.

The CCQE interaction cross-section uncertainty for bound neuclei is estimated from the difference in the q^2 distribution of the Fermi gas model of Smith-Moniz model used in this work and that of Nieves et al[35]. It is taken to have a 1-σ width of 1%. The uncertainties for the CCQE cross-section $\bar{\nu}/\nu$ ratio and $(\nu_\mu + \bar{\nu}_\mu)/(\nu_e + \bar{\nu}_e)$ flavor ratio are estimated in the same manner and taken to be 1.0% each. Uncertainty of single meson production is estimated by comparing expected to experimental results of $\nu_\mu p \to \mu^- p\pi^+$ and is taken to be 20%. The production of single π^0 via the interaction $\nu_\mu n \to \mu^- p\pi^0$ is less well understood. An estimate of 40% for the ratio $\pi^0/\pi^\pm$ uncertainty is used. This is estimated by comparing the models used in this work to the Hernandez model[85]. Comparisons to the Hernandez model are also used to estimate the ratio $\nu/\bar{\nu}$ in single meson production, which is set to 1% for both e and μ.

Deep inelastic scattering uncertainties are divided into two regions: above and below 10 GeV. Above 10 GeV predictions agree with experiment to within 5% and this is used as the uncertainty. Below 10 GeV comparisons with the CKMT model are used and the 1-σ

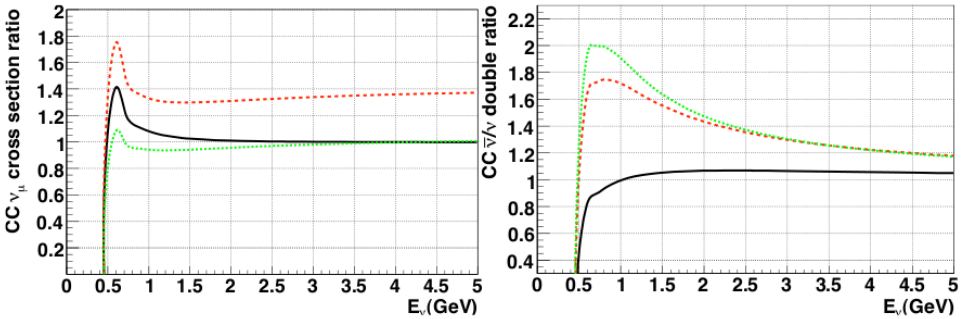

Figure 7.6: Predicted cross-sections (left) and $\bar{\nu}/\nu$ cross-section ratio for $\nu_\mu p \rightarrow \mu^- p\pi^+$ (solid), $\nu_\mu n \rightarrow \mu^- p\pi^0$ (dashed) and $\nu_\mu n \rightarrow \mu^- p\pi^+$ (dotted) for the Hernandez model[85] normalized to the Rein-Sehgal model[101].

width is set to 1.0%. The uncertainty of the squared-momentum transfater Q^2 distribution is estimated by comparing the present model to the original GRV98 model. Coherent pion production is not well-known. The error for NC and CC ν_e interactions is calculated to be 50% from the difference between the Rein-Sehgal[101] and experiment. The CCν_μ coherent pion production channel is completely unmeasured and so the uncertainty is set to 100%.

The overall NC/CC ratio uncertainty is included and is set to be 20%. Nuclear effects in oxygen were updated in the MC sample as described in a previous chapter and the method of calculating their uncertainty was updated as well. The cross-section of the pion final state interactions in the updated NEUT model is compared to experiment to estimate the uncertainty[17]. A new weighting method is applied which weights all possible interaction channels until a 1-σ difference between the simulation and data are found, as shown in 7.7.

7.5.3 Event Selection and Reconstruction Uncertainties

FC/PC Reduction

Errors are calculated for the event reductions by looking at the differences between data and MC for distributions of the variables used in the selection cuts. The FC reduction uncertainties are 0.2%, 0.2%, 0.8% and 0.3% for SK-I,-II,-III and -IV, respectively. For PC, the same reduction uncertainties were 2.5%, 4.8%, 0.5% and 1.0%. The FC/PC separation

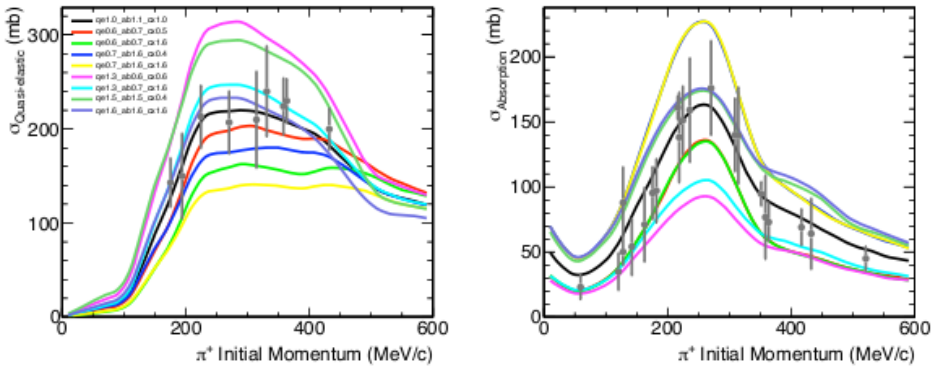

Figure 7.7: Comparisons between data and NEUT simulations for π^+ quasi-elastic (left) and absorption (right) interactions demonstrating the weighting method used in the nuclear effects uncertainty term.

is based on the number of hit OD PMTs in a cluster and the uncertainty is based on comparing the MC and data distributions of the `NHITAC` variable. These terms are assumed to be anti-correlated because a change in the number of FC events will simultaneously result in a change in the opposite direction for the number of PC events. This uncertainty for each run period is estimated to be 0.6%, 0.5%, 0.9% and 0.02%. Similarly, the PC stop/thru separation relies on OD charge distributions (through the ratio $\mathrm{PE}_{anti}/\mathrm{PE}_{exp}$) and terms for the top, barrel and bottom are separately included in the fit.

Upmu Reduction

Uncertainties for the upmu reduction are classified according to the three event categories: stop, thru and showering. Reduction uncertainties are calculated by fitting the reduction efficiency for MC events as a function of zenith bin to a constant and its uncertainty from the fitting is taken as the error. The errors for stopping are 0.7%, 0.7%, 0.7% and 0.5%, and through-going 0.5%, 0.5%, 0.5% and 0.3% for SK-I,-II,-III and -IV, respectively. The stop/thru separation is also treated as a separate error. This is calculated by varying the cut value of the variable `Um_ohit8m` (the number of hits within 8 meters of exit point in the OD) by ± 10% and calculating the percantage change in the stop/thru ratio for MC events.

These values for each run period are 0.5%, 0.8%, 0.7% and 1.0%.

Uncertainty from the Upmu stopping selection cut is accounted for by varying the reconstructed momentum cut value used in the selection (`Fit_mom`) by $\pm\Delta E$ (the energy scale uncertainty) and calculating the percentage change in the number of surviving MC events is the uncertainty estimate. These magnitudes of the errors are 0.9%, 1.3%, 2.0% and 1.7% for SK-I,-II,-III and -IV. For the through-going sample, the reconstructed pathlength (`Fit_len`) cut is varied and the percentage change in the number of through-going events is used as the uncertainty. These values are 1.5%, 2.3%, 2.8% and 1.5% for each detector phase.

Finally the separation of the showering and non-showering samples is also accounted for by varying the shifting the `Sh_delta` cut for MC events an amount based on the difference between the data and MC distributions for the same variable. The resulting percentage change in the showering/non-showering ratio is used for the uncertainty. The estimated values were 11.7%, 11.5%, 6.4% and 10.7% for SK-I,-II,-III and -IV, respectively.

Contamination Backgrounds

A handful of errors accounting for contamination backgrounds in the event samples are also used in the analysis. Examples of these contaminations include propagation of hardons which are reconstructed as μ-like for single-ring NC events, low-energy backgrounds for e-like events such as flasher PMTs and neutron-induced events, and contamination of all μ-like events from cosmic ray muons. Additionally the upmu sample undergoes background subtraction as described in the data reduction chapter and from this subtraction the uncertainty in the number of background events in the most-horizontal bins is accounted for in the χ^2 minimization.

7.5.4 Multi-GeV multi-ring separation

The new binning method includes the separation of the multi-GeV multi-ring sample into ν_e-like and $\bar{\nu_e}$-like categories (the single-ring sample is also separated but the selection criteria is much simpler than for multi-ring, using only the number of decay electrons). A systematic uncertainty is assigned to this separation based on the contents of the separation likelihood,

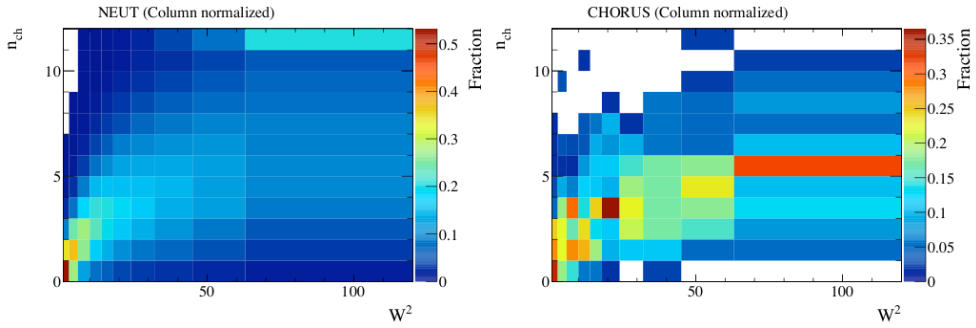

Figure 7.8: Pion multiplicity as a function of W^2 for NEUT predictions (left) and CHORUS experimental measurements (right).

which are the number of decay electrons, the number of rings and in turn pion effects (final state interactions, multiplicity, etc.). Pion final state interaction uncertainties are included as mentioned above by the newly-introduced MC weighting methods. Uncertainties in pion multiplicity are estimated by comparing the NEUT predictions to data from the CHORUS experiment[23]. Plots showing the pion multiplicity as a function of W^2 (W is the invariant mass of the final state particles) for NEUT predictions and CHORUS data are shown in 7.8.

A pion multiplicity weight is added to each MC event in addition to its FSI cross-section weight. The difference in the CCν_e purities of the original likelihood and the weighted likelihood is than calculated and taken as the systematic uncertainty. The values are found to be 7.16%, 7.91%, 7.68% and 6.82% for SK-I,-II,-III and -IV, respectively.

7.5.5 π^0-like selection

The identification of π^0-like events are dependent upon the π^0 mass reconstruction and likelihood distributions. Uncertainties here are again estimated by comparing MC and data distributions with separate error terms for each momentum region (because the π^0 likelihood distribution depends on momentum). The uncertainty also depends on the energy scale uncertainty and the calculation includes this contribution as well. Two-ring π^0-like events are also part of the final dataset and are dependent upon ring-counting and PID algorithms.

Their uncertainties are estimated to be 2.0% for SK-I and -II, 1.0% for SK-III and 1.8% for SK-IV.

7.5.6 Decay Electron Tagging

A cosmic ray muon sample is used to estimate the efficiency of tagging decay electrons. This study was completed in SK-I[67] and is assumed to be 1.5% for all detector periods. A component from π^+ decay is also considered because positive pions have a probability to decay before interacting in water. This decay probability depends on their momentum but can be more than 10% for some momenta. This decay uncertainty is included in the decay-electron tagging efficiency for the FC sub-GeV single-ring e-like sample.

7.5.7 Other Reconstruction Uncertainties

Ring separation and PID likelihood uncertainties are estimated by comparing their respective likelihood MC distributions to data. The absolute energy scale is also assigned an uncertainty, and the values are 1.1% for SK-I, 1.7% for SK-II, 2.7% for SK-III and 2.3% for SK-IV. This uncertainty also indirectly enters into the upmu stopping sample selection cut mentioned in earlier in this chapter. The energy scale uncertainty parameter is defined such that a positive value will increase the amount of visible energy in the MC. Uncertainty in the up/down asymmetry in the energy scale is also included and these values are 0.6% for SK-I and -II, 1.3% for SK-III and 0.3% for SK-IV.

7.6 Results

The results of the fit to the SK-I+II+III+IV full dataset are shown in Figs. 7.9 and 7.10 for the physical region. The 2-dimensional contour in Fig. 7.9 shows the allowed regions at 68% (blue), 90% (red) and 99% (green). The allowed regions represent regions in which $\Delta\chi^2$ ($\equiv \chi^2 - \chi^2_{min}$, or the difference between the χ^2 from the fit and the minimum χ^2 at the best-fit point) satisfies the conditions $\Delta\chi^2 \leq 2.3$, 4.6 and 9.2 for 68%, 90% and 99% C.L., respectively. The best-fit point is found at $\left(\Delta m^2_{23}, \sin^2(2\theta_{23})\right) = (2.30 \times 10^{-3}\ \text{eV}^2,$ 0.99) with χ^2/d.o.f = 555/478 and is indicated by the black star in Fig. 7.9. The 1σ and

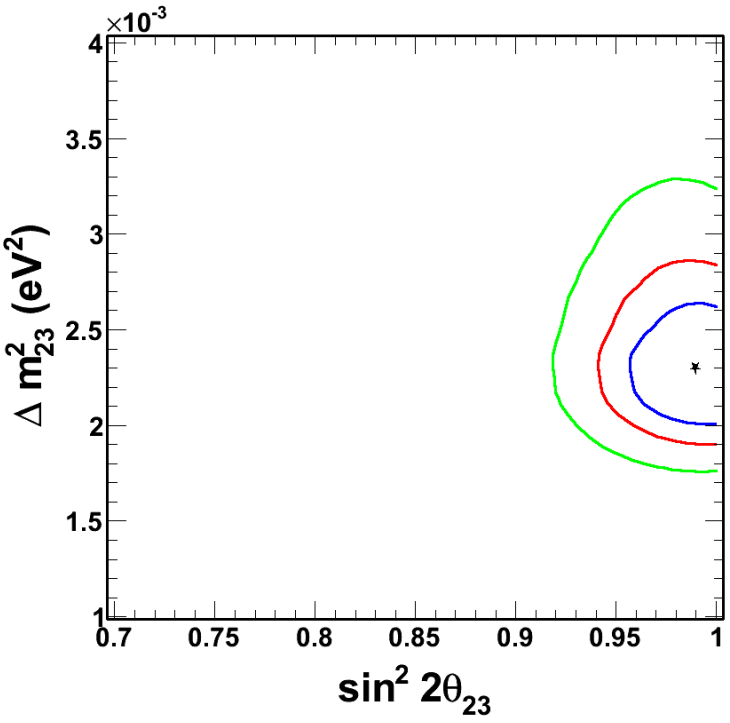

Figure 7.9: The 2-d allowed regions for Δm^2_{23} versus $\sin^2(2\theta_{23})$ at 68%, 90% and 99% C.L. for SK-I+II+III+IV data. The black star indicates the best-fit point.

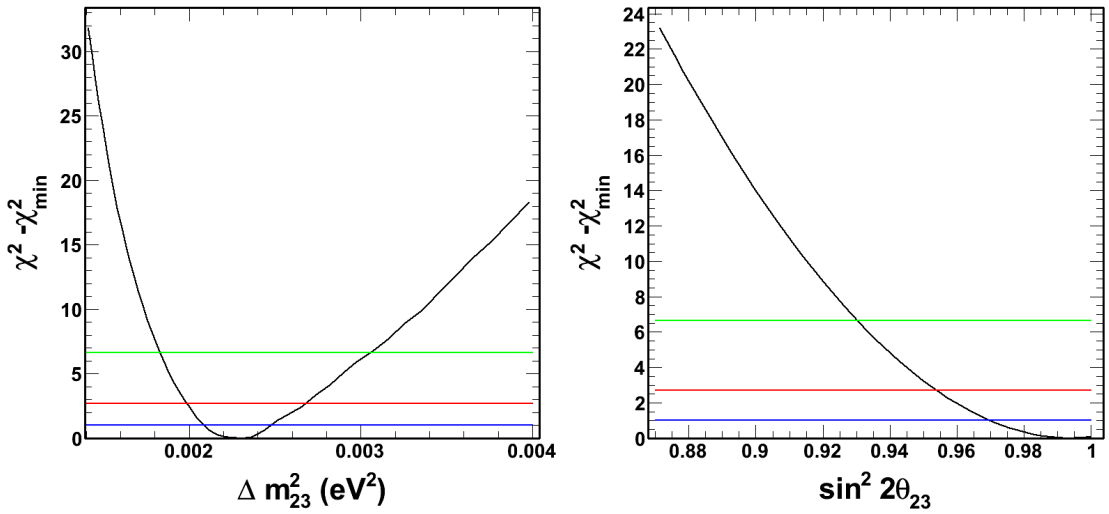

Figure 7.10: The 1-dimensional χ^2 distributions for Δm^2_{23}(left) and $\sin^2(2\theta_{23}$ (right, physical region only) fit to the SK-I+II+III+IV data.

2σ constraints on the individual parameters are determined by their 1-d χ^2 distributions, which are shown in Fig.7.10. The individual parameter constraints are found to be Δm^2_{23} $= 2.30^{+0.17}_{-0.22} \times 10^{-3}$ eV^2 (1σ) and $\sin^2(2\theta_{23}) > 0.95$ (90% C.L.).

The allowed regions for this analysis are found to be similar to, but shifted relative to the previous SK-I+II+III official result. In particular the allowed region has moved upward in the mass-squared splitting space. This effect is mostly from the addition of the SK-IV data to the dataset, which prefers higher values for Δm^2_{23}. This analysis gives excellent agreement with the most recent results from the other active analyses of the same parameters. An overlay of all 2012 results is shown in Fig. 7.11. The physical allowed regions for each individual SK dataset (SK-I,-II,-III and -IV) fit to 2-flavor mixing are shown in 7.12 and 7.13. As the MC was completely regenerated to incorporate the updated NEUT flux models, pion FSI interaction models, and reconstruction updates, the fits to the older datasets (SK-I,-II and -III) are also updated.

The zenith-angle distributions of all the data samples (with SK-I+II+III+IV binned together) are shown in Fig. 7.14. In this figure the red histogram shows the MC oscillated with the best-fit parameters from this analysis and the blue histogram represents the no

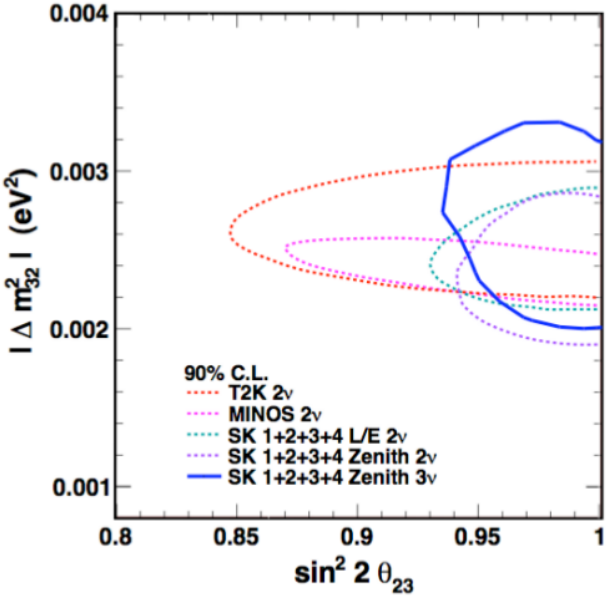

Figure 7.11: The 90% C.L. allowed regions of the most recent 2012 results for this analysis, the SK L/E analysis, the SK full three-parameter zenith-angle analysis, T2K and MINOS.

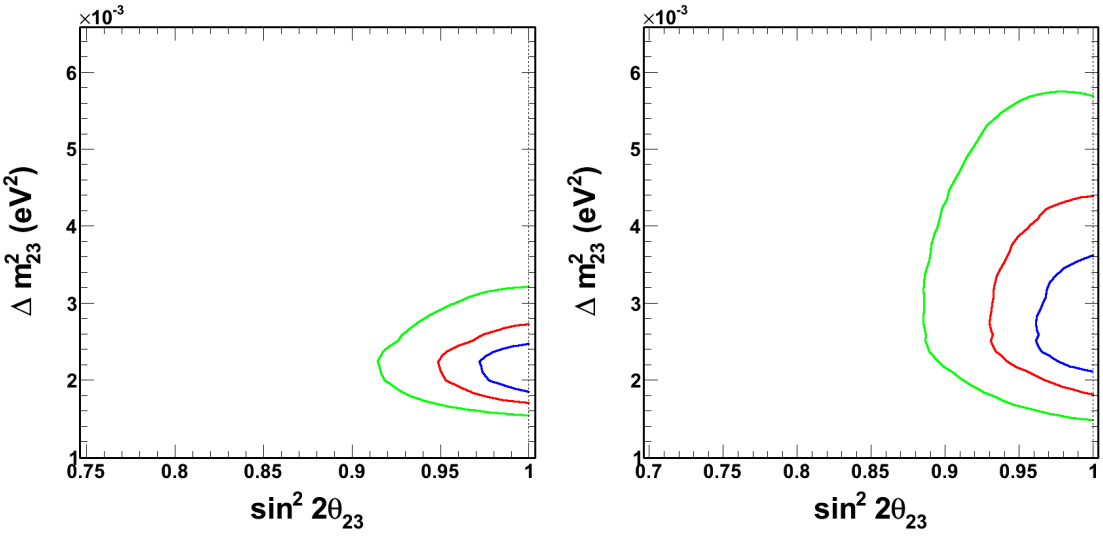

Figure 7.12: The 2-dimensional 68%(blue), 90%(red) and 99%(green) C.L. allowed regions for the SK-I data (left) and SK-II data (right) with the updated MC and reconstruction.

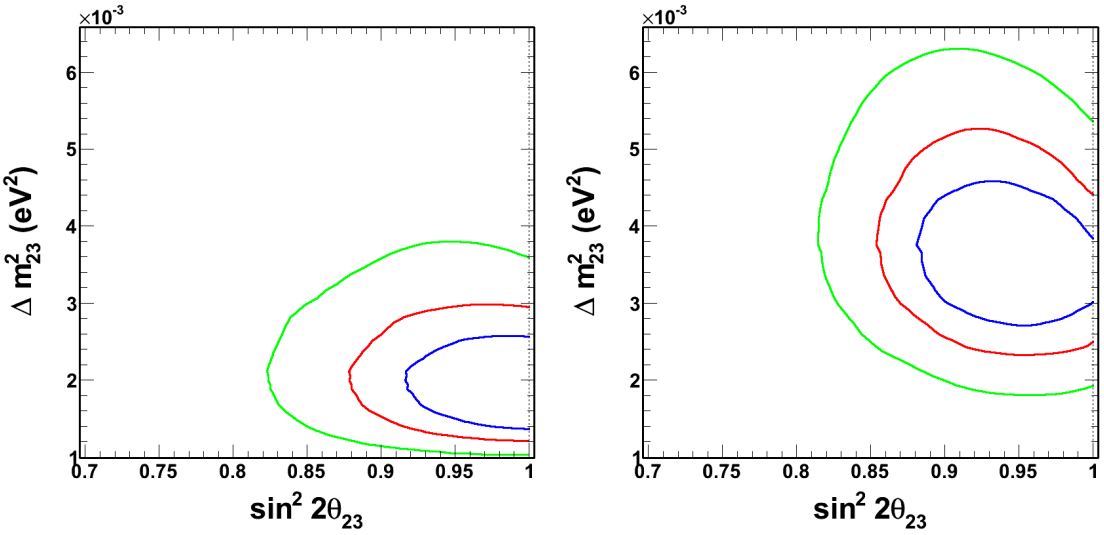

Figure 7.13: The 2-dimensional 68%(blue), 90%(red) and 99%(green) C.L. allowed regions for the SK-III data (left) and SK-IV data (right) with the updated MC and reconstruction.

oscillations prediction.

7.6.1 Systematic Error Pulls

The results of all the systematic error pulls are shown in Figs.7.15 and 7.16. In each of these figures the vertical axis represents the value of ϵ_i divided by the 1σ uncertainty for the i-th error term. The majority of pull terms are well within their 1σ estimation and the largest pull terms are found to be on the order of 1.5σ.

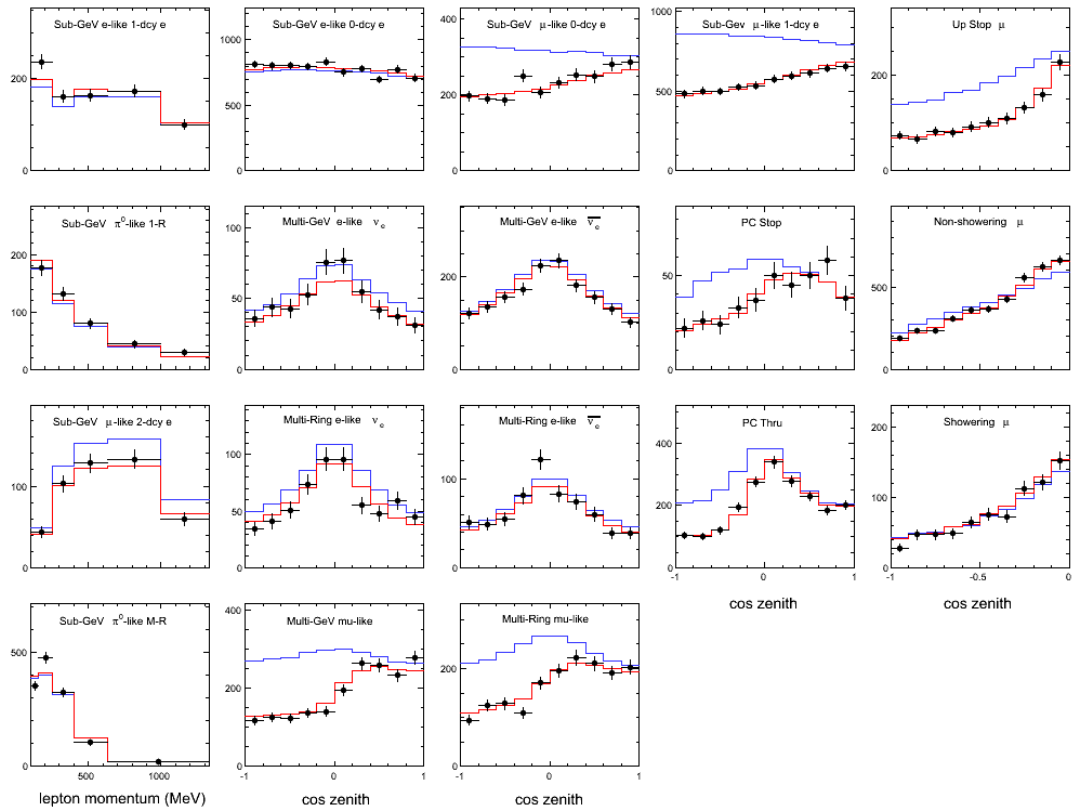

Figure 7.14: The zenith-angle distributions of the SK-I+II+III+IV data (black points), the SK-I+II+III+IV MC oscillated with the best-fit parameters from this analysis (Δm^2_{23}, $\sin^2(2\theta_{23})$) = (2.30 $\times 10^{-3}$ eV^2, 0.99) (red histogram) and the MC with no oscillations (blue histogram).

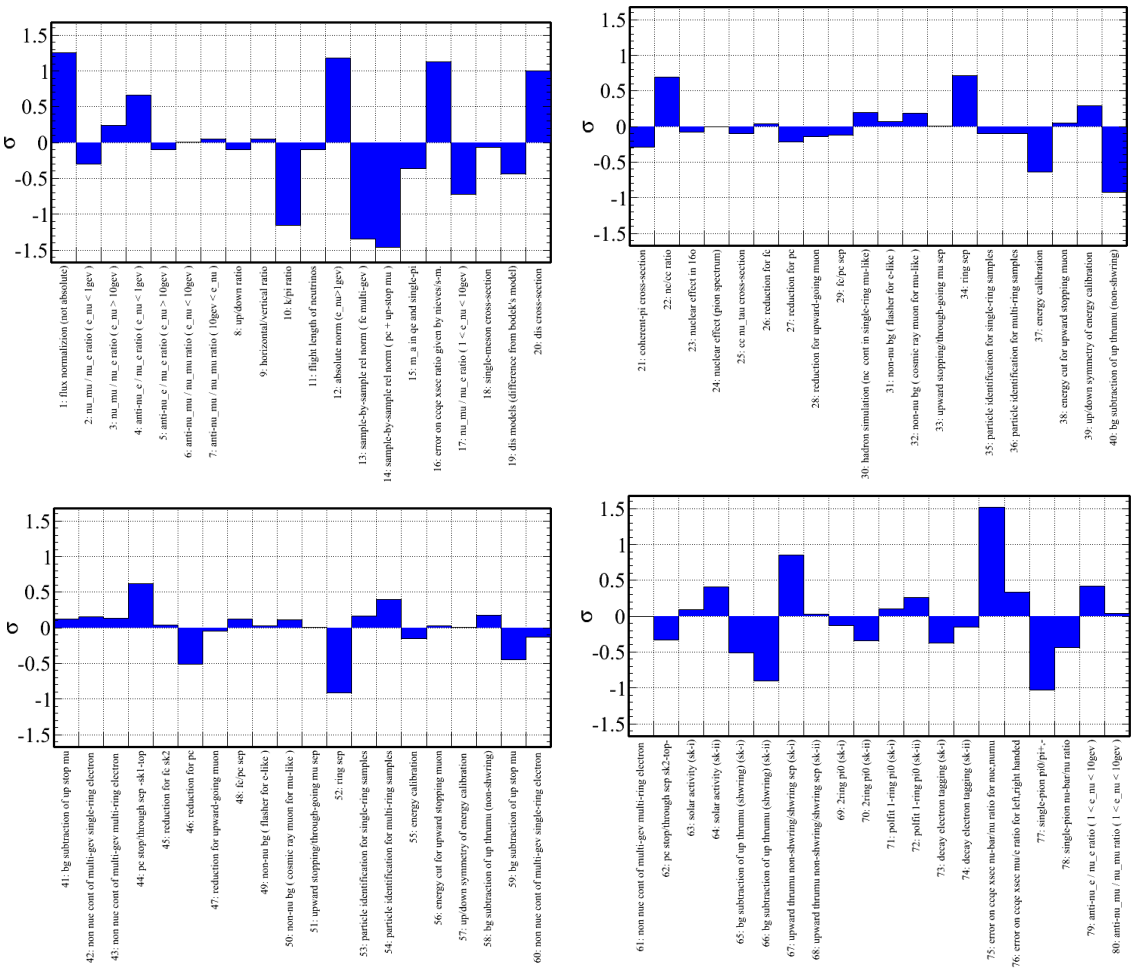

Figure 7.15: The ratios ϵ_i/σ_i for systematic error terms from the 2-flavor fit to the SK-I+II+III+IV data.

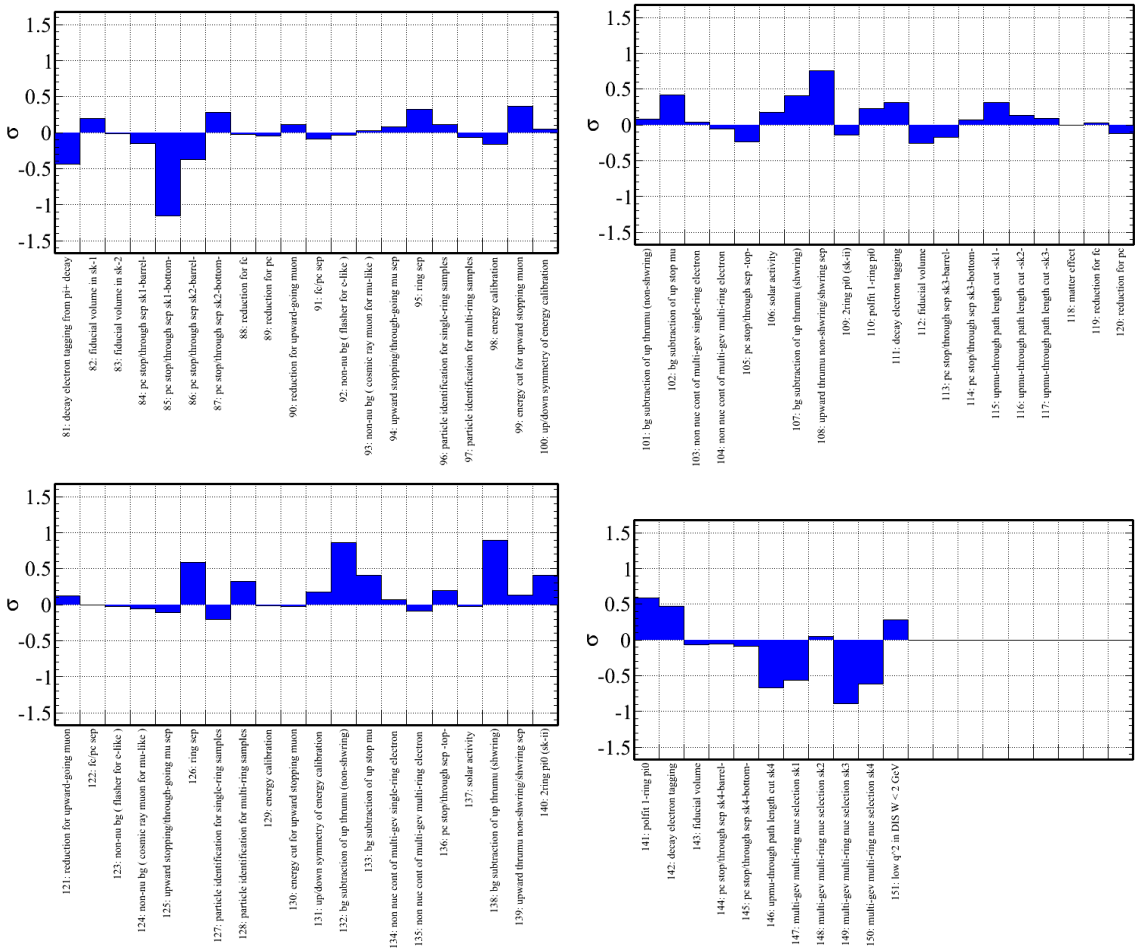

Figure 7.16: The ratios ϵ_i/σ_i for systematic error terms from the 2-flavor fit to the SK-I+II+III+IV data.

Chapter 8

APPARENT CPT VIOLATION MODEL

8.1 Introduction

The present atmospheric neutrino oscillation data from experiments worldwide are well-fit by the simplified 2-flavor oscillation model, as discussed in detail in previous chapters. This model assumes that only oscillations of the form $\nu_\mu \rightarrow \nu_\tau$ occur. However, motivated by results from the LSND[69] and, more recently, MINOS[73, 72] experiments, theorists have suggested more exotic models which reproduce the effects of standard 2-flavor atmospheric mixing as well as simultaneously incorporating additional effects these experiments claim to observe. Common features of these models include the introduction of sterile neutrinos, matter effects, and CPT-violation in neutrino mixing.

One such model, proposed at the University of Washington by Nelson, Engelhardt, and Walsh[21], attempts to explain both standard atmospheric mixing and recent anti-neutrino oscillation results by introducing a sterile neutrino and a non-standard matter interaction potential without introducing CPT-violation. The model was primarily motivated by MINOS[53], a long-baseline accelerator experiment which has constrained both neutrino and anti-neutrino oscillation parameters.

MINOS' initial anti-neutrino constraints, taken from a low-statistics sample of anti-neutrino events found in a neutrino beam, did not agree well with their corresponding neutrino parameters[73, 72]. The constraints were later updated with larger statistics from a dedicated anti-neutrino beam running period, and the discrepancy between neutrinos and anti-neutrinos has since disappeared[55]. The model which is the subject of this analysis was motivated by the earlier results from MINOS. There currently exists no compelling evidence for a difference between neutrino and anti-neutrino oscillations. Nonetheless, this model remains worthy of consideration as it predicts interesting effects in neutrino- and anti-neutrino oscillations in matter without invoking CPT-violation while claiming compatibility

with existing experimental oscillation results.

8.2 Mathematics of Model

The main features of the model are the addition of a sterile neutrino which participates in active-sterile mixing and an exotic matter interaction mediated by a newly-introduced gauge vector boson. With the addition of the sterile neutrino state, the mixing matrix now expands to a 4x4 matrix to include the new mixing angle θ_{34}. The mixing angles θ_{12} and θ_{13} are assumed to be negligible because they do not contribute significantly to mixing at the MINOS neutrino energies and baselines. These assumptions also apply to the atmospheric neutrinos detected at SK. Additionally, maximal atmospheric mixing is assumed with $\theta_{23} = \frac{\pi}{4}$. The resulting simplified 4x4 matrix which transforms between the mass and flavor bases takes the form

$$U_s = \begin{pmatrix} 1 & 0 & 0 & 0 \\ 0 & 1 & 0 & 0 \\ 0 & 0 & \cos\theta_{34} & \sin\theta_{34} \\ 0 & 0 & -\sin\theta_{34} & \cos\theta_{34} \end{pmatrix} \tag{8.1}$$

where the angle θ_{34} quantifies mixing between the heaviest active state and the sterile state.

The neutrino mass hierarchy also expands to include the sterile neutrino as the fourth mass state. The model then simplifies this expanded mass hierarchy to

$$M_m = \mathrm{diag}(0, 0, m, M) \tag{8.2}$$

by assuming that $m_1 = m_2 = 0$. This assumption is analogous to neglecting solar terms in the oscillations. This assumption is valid for long-baseline accelerator and atmospheric neutrino oscillations. The remaining two non-zero mass states correspond to the largest active neutrino mass, m, and the newly-introduced sterile neutrino of mass M.

The model also introduces a new matter interaction for neutrinos. From standard model electroweak interactions, neutrinos traveling in matter experience charged current and neutral current potentials of the forms

$$V_{\mathrm{CC}} = \pm\sqrt{2}G_F N_e \text{ and } V_{\mathrm{NC}} = \pm\frac{G_F}{\sqrt{2}}N_N, \tag{8.3}$$

respectively. Here G_F represents the Fermi constant, N_e the local electron density, and N_n the local neutron density. The model's new $B-L$ gauge interaction is mediated by a new vector boson, previously proposed by Nelson and Walsh[97] to reconcile the results of the MiniBooNE[70] and LSND[69] experiments with the standard oscillations picture. This interaction causes neutrinos to experience an additional potential in matter,

$$V_{B-L} = \pm\frac{\tilde{g}^2}{m_V^2}N_n \tag{8.4}$$

where $\tilde{g}$ represents the coupling constant for the new interaction and m_v the mass of the interaction's gauge boson. This term is positive (negative) for active (anti-)neutrinos and negative (positive) for sterile (anti-)neutrinos, and enhances the difference between neutrino and anti-neutrino oscillations in matter originally coming from the MSW effect[95, 112].

Combining these potentials, the full potential matrix in the flavor basis can be written as

$$V_f = (V_{cc} - V_{nc} - V_{B-L}, -V_{nc} - V_{B-L}, -V_{nc} - V_{B-L}, V_{B-L}). \tag{8.5}$$

The assumptions made so far in the model lead to mixing between the sterile neutrino state and a combination of ν_μ and ν_τ. For atmospheric oscillation studies at Super-Kamiokande, the main oscillation channel is assumed to be $\nu_\mu \to \nu_\tau$. This muon neutrino disappearance is expressed mathematically by the muon neutrino survival probability, as shown in Eqn. 7.1. The muon neutrino survival probability in this new model can be expressed in the interaction basis, where the overall Hamiltonian is diagonal, as

$$P(\nu_\mu \to \nu_\mu) = 1 - \cos^2(\theta_s)\sin^2\left(\frac{\tilde{m}^2 L}{4E}\right) - \sin^2(\theta_s)\sin^2\left(\frac{\tilde{M}^2 L}{4E}\right) - \cos^2(\theta_s)\sin^2(\theta_s)\sin^2\left(\frac{(\tilde{M}^2 - \tilde{m}^2)L}{4E}\right). \tag{8.6}$$

The variables $\tilde{m}^2$ and $\tilde{M}^2$ in this equation are the effective mass-squared splittings in the interaction basis. Likewise, θ_s is the effective sterile mixing angle in the interaction basis.

The reader can refer to [21] and the Appendix for more details. As seen in this equation this ν_μ survival probability allows for more exotic oscillation effects to appear than in standard 2-flavor mixing, especially in the presence of matter which affects the values of $\tilde{M}$ and $\tilde{m}$.

8.3 Fit to MINOS Data

The creators of the model constrained it with MINOS' early muon anti-neutrino data sample, which came from anti-neutrino contamination of the muon neutrino beam[73]. For this analysis the parameter $V = \frac{1}{2}V_{NC} + V_{B-L}$ was defined to quantify the matter interaction. The best-fit values were found to be

$$m = 0.0394 \text{ eV}, M = 0.157 \text{ eV, and } V = 2.01 \times 10^{-4} \text{ neV}. \tag{8.7}$$

For this analysis the local Earth density was assumed to be a constant $\rho = 2.7\frac{g}{cm^3}$, which is the matter density in the crust. The best-fit potential V is larger from the contribution expected from SM interactions alone, which is $V_{SM} = 0.25 \times 10^{-4}$ neV. The best-fit value for the active neutrino mass is smaller than the square root of the 2-flavor atmospheric mass-squared splitting ($\sqrt{\Delta m^2_{23}} \approx 0.049$eV). These two values should become equal in the limit where new exotic oscillation effects are removed from the model.

The allowed regions at 68.3% (blue), 99.5% (red), and 99.7% confidence limits for each pair of parameters are shown in Fig. 8.1. There are two main allowed regions in this analysis. The first includes the best-fit point and has a constant active neutrino mass near $sqrt\delta m^2_{23}$, a sterile neutrino mass M which is large relative to m (minimal active-sterile mixing), and values of the coupling constant near the Fermi constant. The second region extends to much smaller values of m, smaller values of M (more sterile mixing), and larger values of the new interaction's coupling constant. In this allowed region with a great contribution from the new interaction m and M are inversely related.

8.4 Effects on Atmospheric Neutrinos at SK

The atmospheric neutrino data collected at SK cover a wide range of energies and baselines, unlike the MINOS data to which this model was originally fit, which cover a relatively narrow

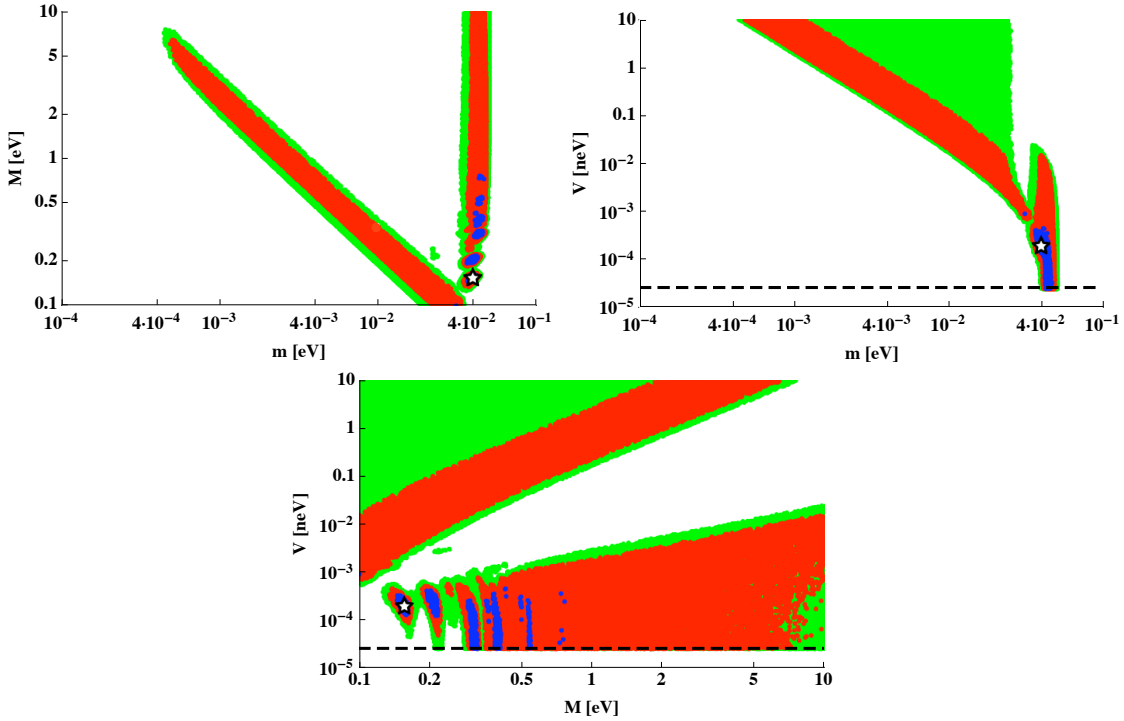

Figure 8.1: Allowed regions from original fit to MINOS anti-neutrino data within 68.3% (blue), 99.5% (red), and 99.7% confidence limits for each pair of parameters, with the best fit point indicated by the star.

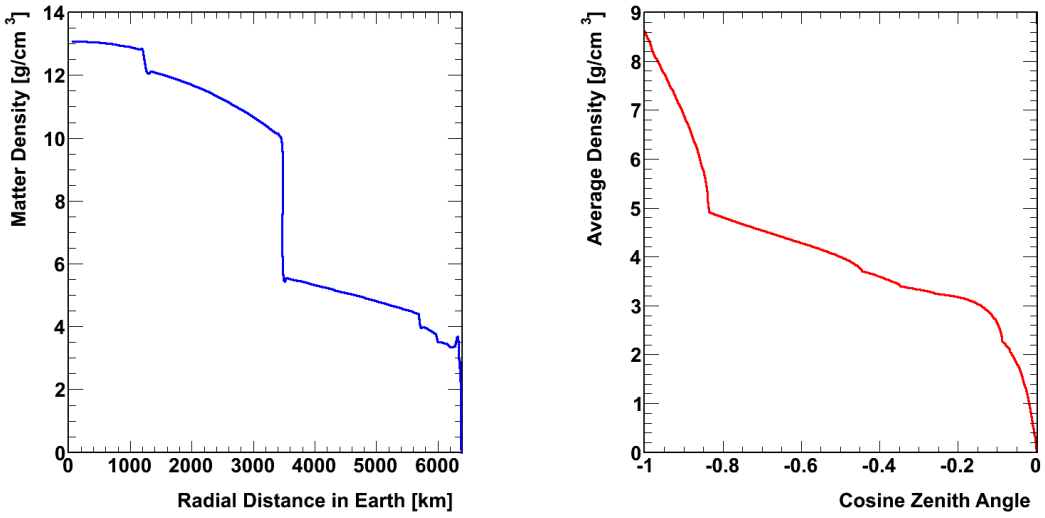

Figure 8.2: Earth density profile as a function of radius according to PREM[20] on the left, and the average line-integral density as a function of cosine zenith angle on the right.

distribution of neutrino energies at a fixed baseline of 735km[53]. The model's oscillations are sensitive to both neutrino energy and baseline (see Eqn. 8.6), so atmospheric neutrinos at SK offer a good opportunity for constraining the model. Because the density of the Earth varies with radial distance, the zenith angle of the incoming neutrino, which determines its pathlength, specifies the Earth matter density along the path. In order to calculate the average matter density traversed by each incoming neutrino, a radial density profile for the Earth given by PREM[20] was assumed. The earth density profile from this model is shown in Fig. 8.2.

Average density as a function of zenith angle was calculated by taking the line-averaged integral of the density along the path for all zenith angles. The average matter potential for each neutrino was calculated by assuming this line-averaged density to be a constant density along the path. The matter potential as a function of zenith angle is shown on the RHS in Fig. 8.2.

The model's variables $\tilde{m}^2$, $\tilde{M}^2$ and θ_s as a function of energy, assuming the parameters in Eqn. 8.7 are shown in Figs. 8.3 and 8.4, respectively. These plots assume an Earth

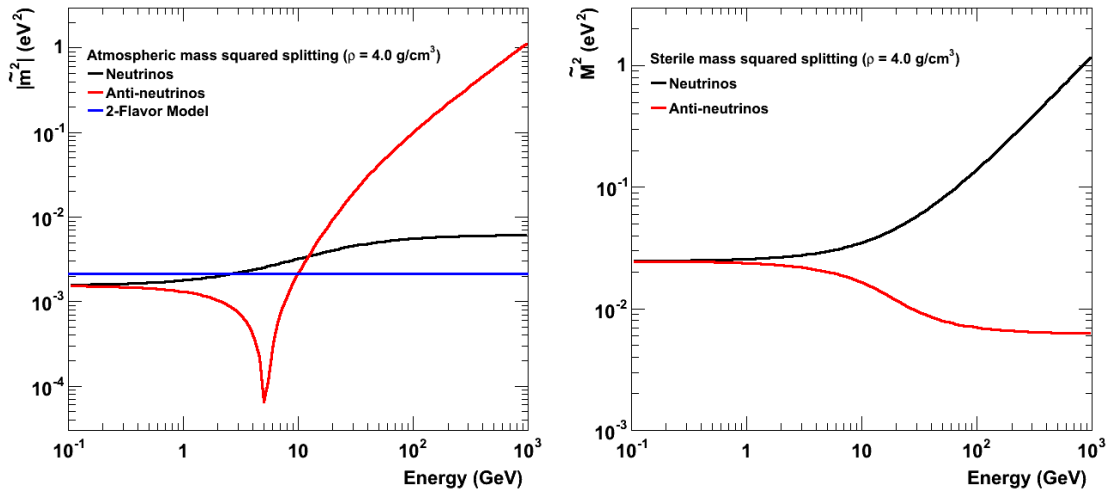

Figure 8.3: Effective mass squared splittings in matter as a function of energy in the apparent CPT-violation model. The 2-flavor atmospheric mass squared splitting is shown in the left-hand figure for comparison. A density of $\rho = 4.0\frac{g}{cm^3}$ for the Earth is assumed.

density of $\rho = 4.0\frac{g}{cm^3}$, since neutrinos detected at SK are not limited to passing through only the crust.

With the interaction potential distribution known, the oscillation survival probability can be calculated for atmospheric muon neutrinos. A 2-dimensional contour plot of the model's predicted muon neutrino and anti-neutrino survival probabilities for a wide range of energies and zenith angles, including those of the atmospheric neutrinos arriving at SK, is shown in Fig. 8.5. The model input parameters for the neutrino masses and interaction coupling are assumed to be the values from Eqn. 8.7.

In this figure it can be seen that the model predicts rapid oscillations as a function of neutrino baseline and energy, especially in the anti-neutrino case. Contours showing the difference between this model and the standard 2-flavor model (as shown in Fig. 7.3) are shown in Fig. 8.6. The regions of large difference predict noticeable disappearance effects in the SK atmospheric data.

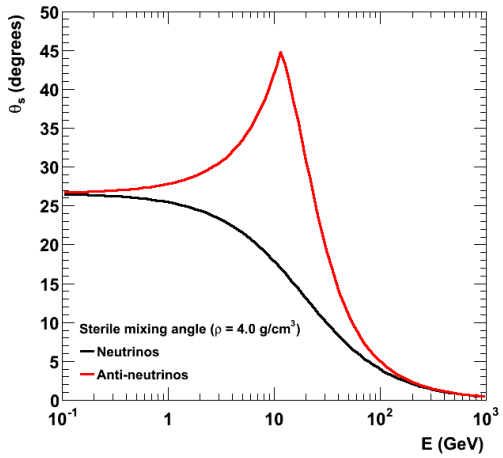

Figure 8.4: Effective mixing angle in matter as a function of energy. A density of $\rho = 4.0 \frac{g}{cm^3}$ for the Earth is assumed.

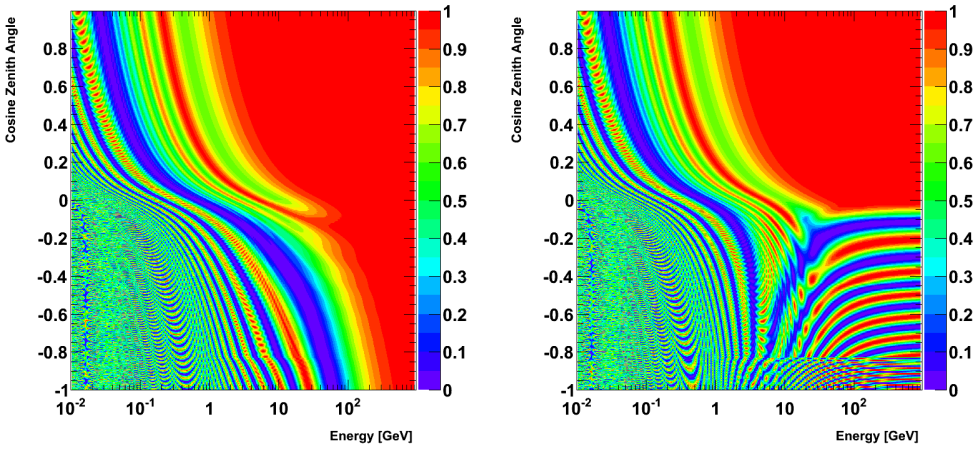

Figure 8.5: Theoretical survival probabilities for muon neutrinos and anti-neutrinos in the apparent CPT-violation model.

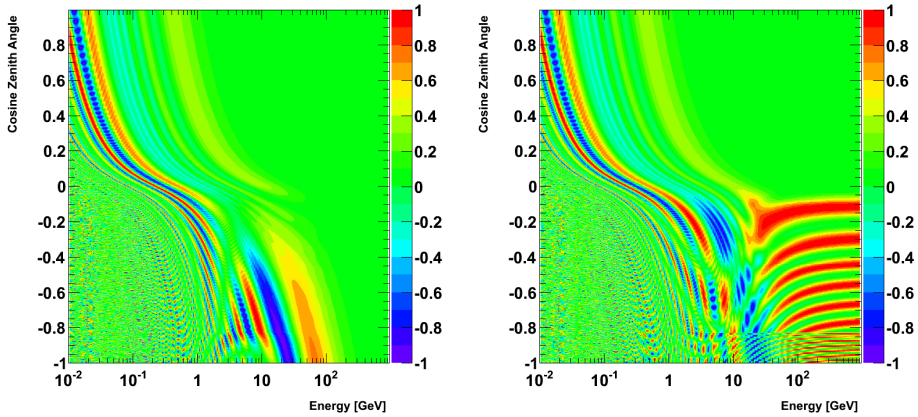

Figure 8.6: Difference of oscillation survival probabilities for muon neutrinos and anti-neutrinos between the apparent CPT-violation model and the standard 2-flavor model.

8.5 Analysis Method

The model was fit to the SK-I+II+III+IV datasets using the same pull method [75] used in the 2-flavor analysis from the previous chapter. The details of the datasets are shown in Table 7.4.1. For the official monte carlo samples, 500 simulated livetime years of FC and PC and 200 years of Upmu events were used for each generation of SK. In this analysis three parameters were varied on a grid to find the best fit to the SK data. The active neutrino mass (m) and sterile neutrino mass (M), defined just as in the original model, were the first two parameters fitted. The third and final fit parameter, g, describes the overall (weak plus exotic) interaction coupling and is equal to

$$g = G_F + 2\sqrt{2}\frac{\tilde{g}^2}{m_V^2}. \tag{8.8}$$

This coupling constant reduces to the Fermi constant in the absence of the interaction. For a given matter density g is directly proportional to the matter potential V. However, unlike the accelerator beam neutrinos at MINOS, the neutrinos detected at SK travel through a non-uniform matter density, so the potential V varies along the path even for the same neutrino. Therefore, g was used in the fitting instead of V. The ranges of each of the parameters was

$$0.0001 \text{ eV} < m < 0.1 \text{ eV} \tag{8.9}$$

$$0.1 \text{ eV} < M < 100.0 \text{ eV} \tag{8.10}$$

$$1.167 \text{ x}10^{-5} \text{ GeV}^{-2} < g < 1.0 \text{ GeV}^{-2}, \tag{8.11}$$

with a total of 96,400 points tested. These ranges completely covered the values tested in the original model's paper. At each analysis point, each MC event was assigned an oscillation weight using Eqn. 8.6 with the model parameters taken at that point. After assigning oscillation weights, both the data and oscillated MC events were placed into one of the 480 analysis bins shown in Fig. 7.1, based on their event type, energy and zenith-angle values. For each analysis point a total chi-squared was calculated by summing the individual chi-squared contributions of each bin using Eqn. 7.7. Each of the 150 systematic error pull terms was allowed to fluctuate to minimize the overall chi-squared for each analysis point just as in the 2-flavor analysis.

8.6 Analysis Results

The 2-dimensional contours showing the 68%, 90% and 99% allowed regions of the model from the fit to the SK-I+II+III+IV data are shown in Figs. 8.7, 8.8 and 8.9.

The SK dataset rules out a large portion of the original model's allowed regions. The 1-dimensional χ^2 distributions for each of the three parameters is shown in Figs. 8.10,8.11,8.12.

The minimum chi-squared was found at the combination of parameters.

$$m = 0.046 \text{ eV}, M = 10 \text{ eV}, g = 1.44 \times 10^{-5} \text{ GeV}^{-2} \tag{8.12}$$

with $\chi^2_{min} = 554/478$ d.o.f.

The best-fit value for the lightest non-zero neutrino mass in the model agrees well with the square root of the atmospheric mass-splitting value predicted by the standard 2-flavor model ($m \sim \sqrt{\Delta m^2_{23}}$) if the lighter mass states are assumed to be zero. The best-fit mass for the heavier sterile neutrino state allows only a modest amount of sterile-active mixing because of the result $M \gg m$ (this limit suppresses active-sterile mixing). This is consistent with a previous analysis at SK constraining sterile-active mixing[60].

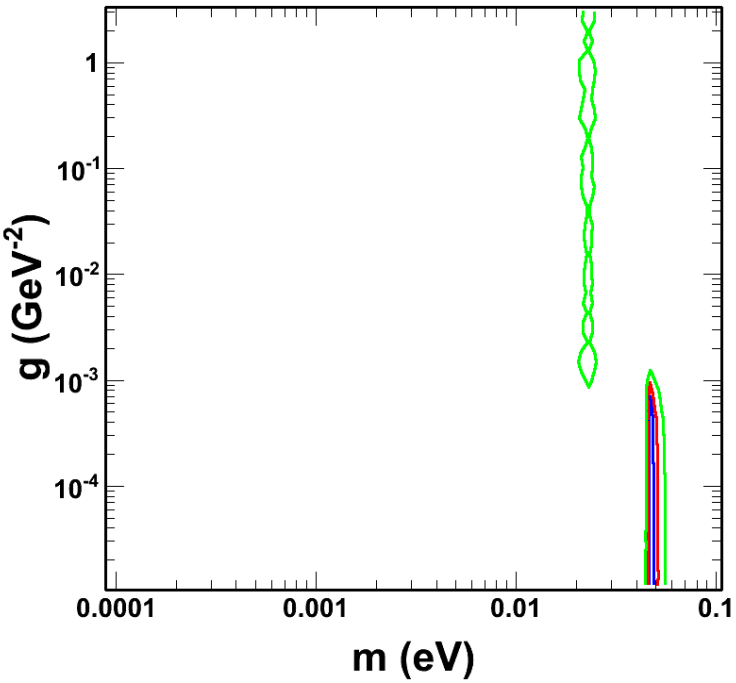

Figure 8.7: The 68% (blue), 90% (red) and 99% (green) allowed regions in the g versus m space for the fit to the SK-I+II+III+IV data, with M minimized away.

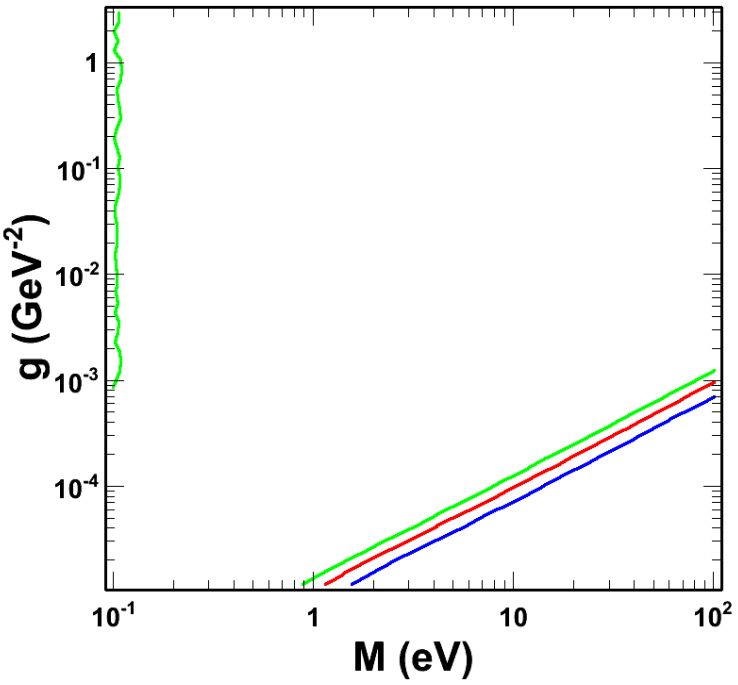

Figure 8.8: The 68% (blue), 90% (red) and 99% (green) allowed regions in the g versus M space for the fit to the SK-I+II+III+IV data, with m minimized away.

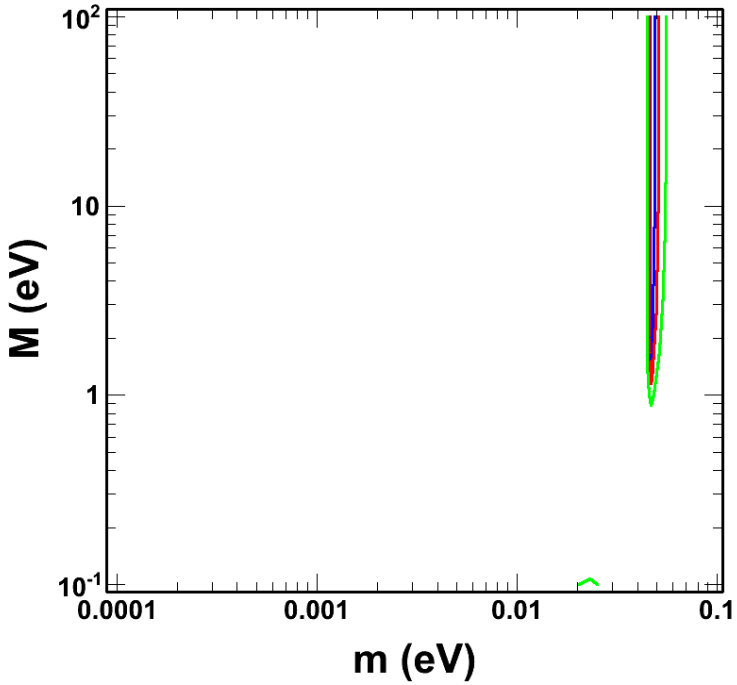

Figure 8.9: The 68% (blue), 90% (red) and 99% (green) allowed regions in the M versus m space for the fit to the SK-I+II+III+IV data, with g minimized away.

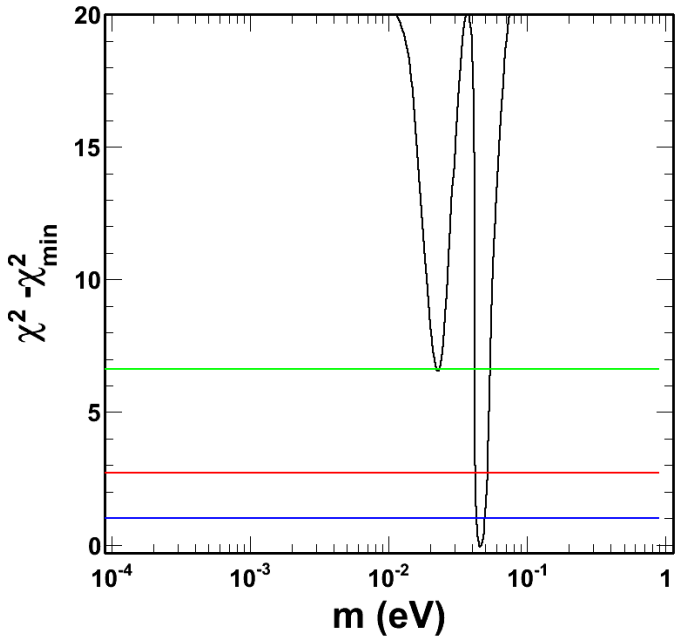

Figure 8.10: The 1-d χ^2 distribution and 68% (blue), 90% (red) and 99% (green) C.L. for the active neutrino mass m after fitting to the SK-I+II+III+IV data.

In conclusion the only allowed region at 90% C.L. corresponds to small sterile-active mixing, active neutrino disappearance consistent with 2-flavor atmospheric mixing, and a very small contribution from the new gauge boson in the interaction coupling constant. A lower bound is placed on the sterile neutrino mass in this model of $M > 1.4$ eV at 90% C.L. An upper bound is placed on the component of the new interaction in the Fermi coupling of $g < 8.0 \times 10^{-4}$ GeV^{-2} at 90% C.L.

In addition to the largest allowed region, smaller disconnected allowed regions exist. These regions correspond to a smaller amount of traditional muon disappearance combined with increased sterile-active mixing. These regions are allowed only at 99% and this is because the particular combination of parameters there almost reproduces 2-flavor disappearance for neutrinos, but diverges significantly from the 2-flavor model for anti-neutrinos, thus ruling them out at 90% C.L.

Studies were done on this region to see if the SK data were capable of ruling them out

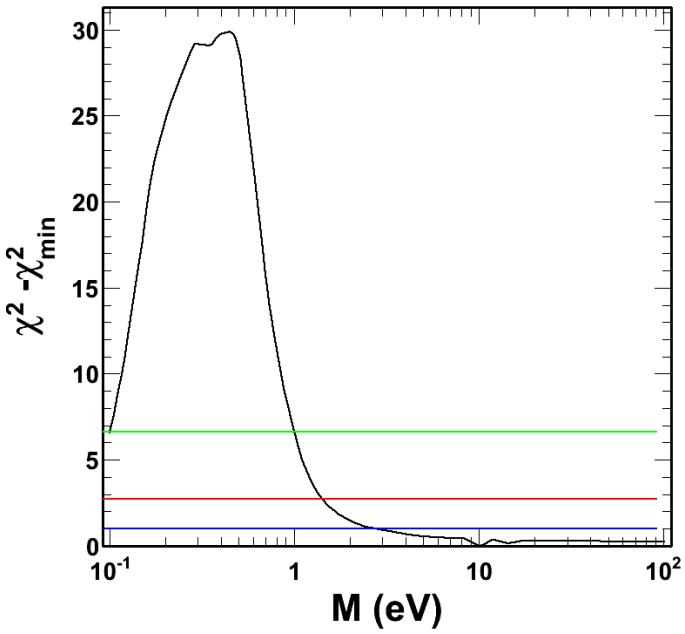

Figure 8.11: The 1-d χ^2 distribution and 68% (blue), 90% (red) and 99% (green) C.L. for the sterile neutrino mass M after fitting to the SK-I+II+III+IV data.

with increased livetime. One such study was a sensitivity study using SK-I+II+III MC simulated at livetimes of 7.9 years (the actual SK-I+II+III livetime), 15.8 years (double the livetime) and 50 years. The result of the expected sensitivity to the exotic coupling parameter g is shown in Fig. 8.13. This study shows that for large values of g, the χ^2 becomes independent of g and flattens off, even with 50 years livetime. Thus, the flattening of the distribution is an inherent limitation in SK's ability to constrain such physics. However, the degree at which these higher values of g are ruled out by SK increases correspondingly with livetime.

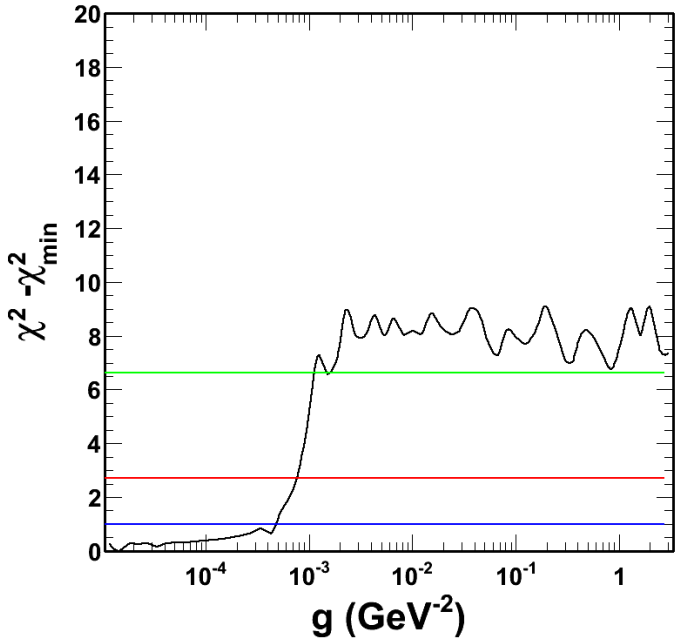

Figure 8.12: The 1-d χ^2 distribution and 68% (blue), 90% (red) and 99% (green) C.L. for the new coupling interaction g after fitting to the SK-I+II+III+IV data.

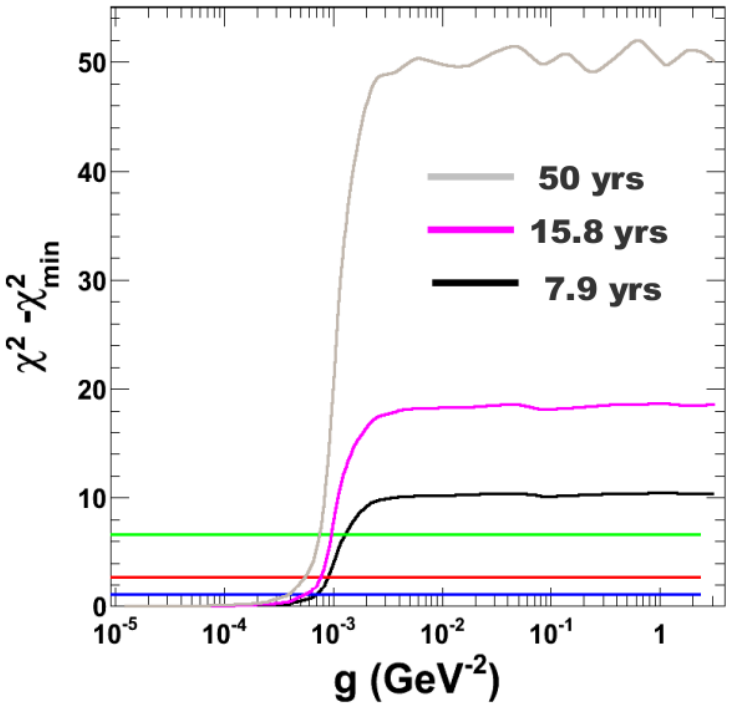

Figure 8.13: The 1-d χ^2 distribution and 68% (blue), 90% (red) and 99% (green) C.L. for the new coupling interaction g in a sensitivity study for livetimes 0f 7.9, 15.8 and 50 years with the SK-I+II+III MC.

Chapter 9

CONCLUSION

The Super-Kamiokande experiment has been taking atmospheric neutrino data since April 1, 1996 and has operated in four distinct phases. We have conducted an analysis of two neutrino oscillation models using the atmospheric neutrino data set collected in all four periods. The updates in this analysis include the addition of 1,096.66 days of additional livetime collected during the SK-IV period, improvements to the Monte Carlo simulations, including flux, nuclear interaction and detector response models, an upgraded data acquisition system with improved dynamic charge and high-rate performance, an updated event binning scheme and fully reprocessed Monte Carlo samples for fully contained, partially contained and upward-going muon reduction.

We fit the SK-I+II+III+IV data to the 2-flavor muon neutrino disappearance model using the improved MC sample and a zenith-angle binning technique. We measured values of $\Delta m^2_{23} = 2.30^{+0.17}_{-0.22} \times 10^{-3}$ eV^2 and $\sin^2 2\theta_{23} > 0.95$, 90% C.L. for the parameters in the model. We find that these results have excellent agreement with recent worldwide constraints on the same parameters.

We also fit the same dataset to a non-standard interaction model which includes both sterile neutrino mixing and a new matter interaction. We find that the SK data rule out most of the model's parameter space and limit the model to the region where standard 2-flavor mixing is recovered.

BIBLIOGRAPHY

[1] E. Kh. Akhmedov. Neutrino physics. *arXiv:hep-ph/0001264v2*, 2000.

[2] V. Barger, Danny Marfatia, and Adam Tregre. Neutrino mass limits from sdss, 2dfgrs, and wmap. *Physics Letters B*, 595:55–59, 2004.

[3] G. D. Barr, T.K. Gaisser, P.Lipari, S. Robbins, and T. Stanev. Three-dimensional calculation of atmospheric neutrinos. *Physical Review D*, 70:023006, 2004.

[4] G. Battistoni, A. Ferrari, T. Montaruli, and P.R. Sala. The fluka atmospheric neutrino flux calculation. *Astroparticle Physics*, 19:269–290, 2004.

[5] Kirk Bays. PhD thesis, University of California-Irvine, 2012.

[6] A. Bodek and U.K. Yang. Modeling neutrino and electron scattering inelastic cross sections. *arXiv:hep-ex/0308007v1*.

[7] R. Brun and F. Carminati. Geant: Detector description and simulation tool. *CERN Program Library Long Writeup*, W5013, 1993.

[8] A. Chavarria. http://www.phy.duke.edu/ schol/superk/alvaro thesis.pdf. Senior Thesis, 2007.

[9] ALEPH Collaboration. Determination of the number of light neutrino species. *Physics Letters B*, 231:519–529, 1989.

[10] Borexino Collaboration. Observation of geoneutrinos. *Physics Letters B*, 687:299–304, 2010.

[11] Super-Kamiokande Collaboration, 2002. http://www-sk.icrr.u-tokyo.ac.jp/cause-committee/index-e.html.

[12] Super-Kamiokande Collaboration. The super-kamiokande detector. *Nuclear Instruments and Methods in Physics Research*, 501A:418–462, 2003.

[13] T. Jannakos (KARMEN Collaboration). The karmen limit on $\bar{\nu}_\mu \rightarrow \bar{\nu}_e$ oscillation and its implication for the lsnd result. *Nuclear Physics B (Proceedings Supplements)*, 85:84–90, 2000.

[14] Zoa Conner. PhD thesis, University of Maryland, 1997.

[15] E. R. Davies. *Machine Vision: Theory, Algorithms, Practicalities.* Academic Press, San Diego, 1997.

[16] Raymond Davis Jr., Don Harmer S., and Kenneth Hoffman C. Search for neutrinos from the sun. *Physical Review Letters*, 20:1205–1209, 1968.

[17] Patrick de Perio. Neut pion fsi. *AIP Conference Proceedings*, 1405:223–228, 2011.

[18] Shantanu Desai. PhD thesis, Boston University, 2004.

[19] Fanny M. Dufour. PhD thesis, Boston University, 2009.

[20] Adam M. Dziewonski and Don L. Anderson. *Physics of the Earth and Planetary Interiors*, 25(297), 1981.

[21] Netta Engelhardt, Ann E. Nelson, and Jonathan R. Walsh. Apparent cpt violation in neutrino oscillation experiments. *Physical Review D*, D81(113001), 2010.

[22] A. A. Aguilar-Arevalo et al. A combined $\nu_\mu \to \nu_e$ & $\bar{\nu}_\mu \to \bar{\nu}_e$ oscillation analysis of miniboone excesses. *arXiv:hep-ex/1207.4809v1*, 2012.

[23] A. Kayis-Topaksu et al. Charged-particle multiplicities in charged-current neutrino- and anti-neutrino-nucelus interactions. *The European Physical Journal C*, 51(4):775–785, 2007.

[24] A.A. Aguilar-Arevalo et al. Measurement of muon neutrino quasi-elastic scattering on carbon. *Physical Review Letters*, 100:032301, 2008.

[25] Ch. Kraus et al. Most recent results of the mainz neutrino mass experiment. *Nuclear Physics B (Proceedings Supplements)*, 118:482, 2003.

[26] D. Rowntree et al. π^+ absorption on n and ar. *Physical Review C*, 60:054610, 1999.

[27] F.P. An et al. Observation of electron-antineutrino disappearance at daya bay. arXiv:1203.1669v2 [hep-ex].

[28] G. Ambrosini et al. Production ratios from 450 gev/c protons on beryllium. *Physics Letters B*, 420:225, 1998.

[29] G. Danby et al. Observation of high-energy neutrino reactions and the existence of two kinds of neutrinos. *Physical Review Letters*, 9:36–44, 1962.

[30] Glenn Rowe et al. Energy-dependent phase shift analysis of pion-nulceon scattering below 400 mev. *Physical Review C*, 18:584–589, 1978.

[31] H. Nishino et al. High-speed charge-to-time coverter asic for the super-kamiokande detector. *Nuclear Instruments and Methods in Physics Research*, 610A:710–717, 2009.

[32] H. Nishino et al. Search for proton decay via $p \to e^+\pi^0$ and $p \to \mu^+\pi^0$ in a large water cherenkov detector. *Physical Review Letters*, 102, 2009.

[33] H. Nishino et al. The new front-end electronics for the super-kamiokande experiment. *Nuclear Science Symposium Conference Record, NSS '07, IEEE*, pages 127–132, October 26 2007–November 3 2007.

[34] J. Beringer et al. 2012 review of particle physics. *Physical Review D*, 86:010001, 2012.

[35] J. Nieves et al. Inclusive quasielastic charged-current neutrino-nucelus interactions. *Physical Review C*, 70:055503, 2004.

[36] K. Abe et al. Indication of electron neutrino appearance from an accelerator-produced off-axis muon neutrino beam. *Physical Review Letters*, 107:041801, 2011.

[37] K. Abe et al. Search for difference in oscillation parameters for atmospheric neutrinos and anti-neutrinos at super-kamiokande. *Physical Review Letters*, 107:241801, 2011.

[38] K. Abe et al. Solar neutrino results in super-kamiokande-iii. *Physical Review D*, 83:052010, 2011.

[39] K. Abe et al. The t2k experiment. *Nuclear Instruments and Methods in Physics Research*, 659A:106–135, 2011.

[40] K. Niita et al. Phits - a particle and heavy ion transport code system. *Radiation Measurements*, 41:1080, 2006.

[41] K. S. Hirata et al. Observation in the kamiokande-ii detector of the neutrino burst from supernova sn1987a. *Physical Review D*, 38(2):448–458, 1988.

[42] K. S. Hirata et al. Observation of ^{8}b solar neutrinos in the kamiokande-ii detector. *Physical Review Letters*, 63(1):16–19, 1989.

[43] Kim Soo-Bong et al. Observation of reactor electron antineutrino disappearance in the reno experiment. arXiv:1204.0626v2 [hep-ex].

[44] Kirk Bays et al. Supernova relic neutrino search at super-kamiokande. *Physical Review D*, 85, 2012.

[45] M. Ahn et al. Measurement of neutrino oscillation by the k2k experiment. *Physical Review D*, 74:072003, 2006.

[46] M. E. C. Swanson et al. Search for diffuse astrophysical neutrino flux using ultra-high-energy upward-going muons in super-kamiokande-i. *The Astrophysical Journal*, 652(1), 2006.

[47] M. Honda et al. New calculation of the atmospheric neutrino flux in a three-dimensional scheme. *Physical Review D*, 70:043008, 2004.

[48] M. Honda et al. Calculation of atmospheric neutrino flux using the interaction model calibrated with atmospheric muon data. *Physical Review D*, 75:043006, 2007.

[49] M. Honda et al. Improvement of low energy atmospheric neutrino flux calculation using the jam nuclear interaction model. *Physical Review D*, 83:123001, 2011.

[50] M. Nakahata et al. Atmospheric neutrino background and pion nuclear effect for kamioka nucleon decay experiment. *Journal of the Physical Society of Japan*, 55:3786, 1986.

[51] M. Nakahata et al. Calibration of super-kamiokande using an electron linac. *Nuclear Instruments and Methods in Physics Research*, A421:113–129, 1999.

[52] M.H. Ahn et al. Measurement of neutrino oscillation by the k2k experiment. *Physical Review D*, 74:072003, 2006.

[53] P. Adamson et al. Measurement of neutrino oscillations with the minos detectors in the numi beam. *Phys. Rev. Lett.*, 101:131802, Sep 2008.

[54] P. Adamson et al. Measurement of the neutrino mass splitting and flavor mixing by minos. *Physical Review Letters*, 106:181801, 2011.

[55] P. Adamson et al. An improved measurement of muon antineutrino disappearance in minos. *Physical Review Letter*, 108:191801, 2012.

[56] R. Becker-Szendy et al. Imb-3: a large water cherenkov detector for nucleon decay and neutrino interactions. *Nuclear Instrumentation & Methods in Physics Research*, A324:363, 1993.

[57] R. Wendell et al. Atmospheric neutrino oscillation analysis with subleading effects in super-kamiokande i,ii and iii. *Physical Review D*, 81:092004, 2010.

[58] R.A. Arndt et al. Dispersion relation constrained partial wave analysis of πn elastic and πn $\rightarrow \eta n$ scattering data: The baryon spectrum. *Physical Review C*, 69:035213, 2004.

[59] S. Abe et al. Precision measurement of neutrino oscillation parameters. *Physical Review Letters*, 100:221803, 2008.

[60] S. Fukuda et al. Tau neutrinos favored over sterile neutrinos in atmospheric muon neutrino oscillations. *Physical Review Letters*, 85:3999–4003, 2000.

[61] S.N. Ahmed et al. Measurement of the total active ^{8}b solar neutrino flux at the sudbury neutrino observatory with enhanced neutral current sensitivity. *Physical Review Letters*, 92:181301, 2004.

[62] Tanaka T. et al. An indirect search for weakly interacting massive particles in the sun using 3109.6 days of upward-going muons in super-kamiokande. *The Astrophysical Journal*, 742, 2011.

[63] V.M. Lobashev et al. Direct search for neutrino mass and anomaly in the tritium beta-spectrum: Status of "troitsk neutrino mass" experiment. *Nuclear Physics B (Proceedings Supplements)*, 91:280–286, 2001.

[64] Y. Ashie et al. Evidence for an oscillatory signature in atmospheric neutrino oscillations. *Physical Review Letters*, 93:101801, 2004.

[65] Y. Ashie et al. A measurement of atmospheric neutrino oscillation parameters by super-kamiokande i. *Physical Review D*, 71:112005, 2005.

[66] Y. Fukuda et al. Evidence for oscillation of atmospheric neutrinos. *Physical Review Letters*, 81:1562–1567, 1998.

[67] Y. Fukuda et al. Measurement of a small atmoshperic ν_μ/ν_e ratio. *Physical Letters B*, 433:9–18, 1998.

[68] B. Ambruster et al. (KARMEN Collaboration). Upper limits for neutrino oscillations muon-antineutrino to electron-antineutrino from muon decay at rest. *Physical Review D*, 65:112001, 2002.

[69] A. Aguilar et al. (LSND). Evidence for neutrino oscillations from the observation of $\bar{\nu}_e$ appearance in a $\bar{\nu}_\mu$ beam. *Physical Review D*, D64(112007), 2001.

[70] A. A. Aguilar-Arevalo et al. (MiniBooNE). *Physical Review Letters*, 98(231801), 2007.

[71] A. A. Aguilar-Arevalo et al. (MiniBooNE). A combined ν_μ to ν_e and $\bar{\nu}_\mu$ to $\bar{\nu}_e$ oscillation analyses of the mineboone excesses. *arXiv:1207.4809v1 [hep-ex]*, 2012.

[72] P. Adamson et al. (MINOS Collaboration). First direct observation of muon antineutrino disappearance. *Physical Review Letters*, 107:021801, 2011.

[73] J. J. Evans. PhD thesis, fERMILAB-THESIS-2009-14, 2009.

[74] Enrico Fermi. *Zeitschrift fur Physik*, 88:161, 1934.

[75] G. L. Fogli, E. Lisi, A. Marrone, D. Montanino, and A. Palazzo. Getting the most from the statistical analysis of solar neutrino oscillations. *Physical Review D*, D66(053010), 2002.

[76] G.L. Fogli, E. Lisi, A. Marrone, A. Palazzo, and A.M. Rotunno. Evidence of theta(13)>0 from global neutrino data analysis. 2011. arXiv:1106.6028v2[hep-ph].

[77] Thomas Patzak for the DONUT Collaboration. First direct observation of the tau neutrino. *Europhysics news*, 32(2):56–57, 2001.

[78] M. Gluck, E. Reya, and A. Vogt. Dynamical parton distributions revisited. *The European Physical Journal C*, 5(3):461–470, 1998.

[79] S.N. Gninenko. Lsnd/miniboone excess events and heavy neutrino from μ and k decays. *Physical Review D*, 83:093010, 2011.

[80] Maurice Goldhaber, L. Grodzins, and A.W. Sunyar. Helicity of neutrinos. *Physical Review*, 109:1015–1017, 1958.

[81] Jan Hamann, Steen Hannestad, Georg G. Raffelt, Irene Tamborra, and Yvone Y.Y. Wong. Cosmology favoring extra radiation and sub-ev mass sterile neutrinos as an option. *Physical Review Letters*, 105:181301, 2010.

[82] Y. Hayato. Neut. *Nuclear Physics B (Proceedings Supplements)*, 112:171–176, 2002.

[83] Y. Hayato. A neutrino interaction simulation library neut. *Acta Physica Polona B*, 40:2477, 2009.

[84] A. E. Hedin. Msise model (1990). *Planetary and Space Science*, 40:556, 1992.

[85] E. Hernandez, J. Nieves, and M. Valverde. Weak pion production off the nucleon. *Physical Review D*, 76:033005, 2007.

[86] Kazuhide Ichikawa, Masataka Fukugita, and Masahiro Kawasaki. Constraining neutrino masses by cmb experiments alone. *Physical Review D*, 71:043001, 2005.

[87] Chizue Ishihara. PhD thesis, University of Tokyo, 2010.

[88] Masaki Ishitsuka. PhD thesis, University of Tokyo, 2004.

[89] J.D. Jackson. *Classical Electrodynamics*. John Wiley & Sons, Inc., 3rd edition, 1998.

[90] C.L. Cowan Jr., F. Reines, F.B. Harrison, H.W. Kruse, and A. D. McGuire. Detection of the free neutrino: A confirmation. *Science*, 124(3212):103–104, 1956.

[91] S. I. Klimushin, E. V. Bugaev, and Igor A. Sokalski. Precise parameterizations of muon energy losses in water. 2001. arXiv:hep-ph/0106010v1.

[92] Maggie Ka-Pik Lee. PhD thesis, University of Tokyo, 2012.

[93] Ziro Maki, Masami Nakagawa, and Shoichi Sakata. Remarks on the unified model of elementary particles. *Progress of Theoretical Physics*, 28(5):870–880, 1962.

[94] Thomas McLachlan. PhD thesis, University of Tokyo, 2012.

[95] S. P. Mikheyev and A. Y. Smirnov. Resonant enhancement of oscillations in matter. *Soviet Journal Nuclear Physics*, 42:913–917, 1985.

[96] Ann E. Nelson. Effects of cp violation from neutral heavy fermions on neutrino oscillations, and the lsnd/miniboone anomalies. *arXiv:1010.3970v1*, 2010.

[97] Ann E. Nelson and Jonathan R. Walsh. *Physical Review D*, D77(033001), 2008.

[98] NOAA, NASA, and US Air Force. *U.S. Standard Atmosphere*. U.S. Government Printing Office, Washington D.C., 1976.

[99] Wolfgang Pauli. Open letter to radioactive ladies and gentlemen (1930). *Physics Today*, 31:27, 1978.

[100] Bruno Pontecorvo. Neutrino experiments and the problem of conservation of leptonic charge. *Soviet Physics JETP*, 26:984, 1968.

[101] Dieter Rein and Lalit M. Sehgal. Neutrino-excitation of baryon resonances and single pion production. *Annals of Physics*, 133:79–151, 1979.

[102] B.G. Ritchie. Parameterization of total and differential cross sections for $\pi d \rightarrow pp$ below 1 gev. *Physical Review C*, 44:533–536, 1991.

[103] S. Roesler, R. Engel, and J. Ranft. The monte carlo event generator dpmjet-iii. *arXiv:hep-ph/0012252*.

[104] L.L. Salcedo and E. Oset et al. Computer simulation of inclusive pion nuclear reactions. *Nuclear Physics A*, 484:557–592, 1988.

[105] T. Sjoestrand. High-energy-physics event generation with pythia 5.7 and jetset 7.4. *Computer Physics Communications*, 82:74–89, 1994.

[106] C.H. Llewellyn Smith. Neutrino reactions at accelerator energies. *Physics Reports*, 3:261–379, 1972.

[107] R. A. Smith and E. J. Moniz. Neutrino reactions on nuclear targets. *Nuclear Physics B*, 43:605–622, 1972.

[108] Yumiko Takenaga. PhD thesis, University of Tokyo, 2008.

[109] Takayuki Tanaka. PhD thesis, University of Nagoya, 2011.

[110] Eric Thrane. PhD thesis, University of Washington, 2008.

[111] Roger A. Wendell. PhD thesis, University of North Carolina, 2008.

[112] L. Wolfenstein. Neutrino oscillations in matter. *Physical Review D*, 17:2369–2374, 1978.

[113] C. Zeitnitz and T.A. Gabriel. The geant-calor interface and benchmark test calculations of zeus calorimeters. *Nuclear Instruments and Methods in Physics Research A*, 349:106–111, 1994.

VITA

Michael Dziomba was born in Buffalo, NY in 1984. He earned a BS in Physics, graduating Summa Cum Laude, from the State University of New York at Buffalo in 2006. He earned his MS (2007) and PhD (2012) in Physics from the University of Washington. His thesis focus was atmospheric neutrino oscillation studies with the Super-Kamiokande detector, with advisor R.J. Wilkes.

.